Synopsis

Depth sensing indentations are indentation experiments in which the load and the displacement of a hard indenter are measured continuously. The complete deformation history of the material indented is recorded as the load-displacement characteristics. The projected area of the indent is obtained from the depth of penetration, known as the geometry of the indenter. Thus hardness of the material is obtained without imaging the resulting impression. This makes the depth sensing indentation ideal for determining the property of small volumes of material, as in nano-indentation. Apart from the hardness, there is a wide range of other material properties that can be obtained from the load-displacement characteristics. The common thread running through this thesis is depth sensing indentation. Chapter 2 deals with a mechanical model of elasto-plastic indentation. A parameter - strength of the Blister field, that characterises the stress field in an elastic-plastic indentation is obtained *ab initio*. Chapter 3 describes the design of a depth sensing indenter capable of measuring material properties by indenting to a depth of nanometers. Chapters 4, 5 and 6 address the problems encountered in indentation when penetration depth is comparable to the surface roughness.

Blister field model [111] gives the stresses in an elastic-plastic indentation as a sum of two elastic fields, one due to a point load and another due to a strain nucleus - blister. Among the existing models, the blister field model predicts the surface strains closest to the values measured using strain gauges [37]. However, the value of the strength of the blister is not known *ab initio*. Chapter 2 derives a method for finding this value using energy conservation principles. The input energy is obtained from the load-displacement characteristics of the indentation. This energy is equated to the energy stored in the highly deformed core and the strain energy of the surrounding elastic medium. Solving the resulting equation, the strength of the blister field is obtained as a function of the material properties and the geometry of the indenter. The theory is verified by continuous surface strain measurements in a depth sensing experiment.

A displacement controlled, depth sensing indentation instrument is designed, fabricated and tested. The main innovation in this design is the use of flexure hinges to measure forces. A system of four flexure hinges, has been used to optimise the conflicting requirements of the sensitivity and the stiffness of the force sensor. A capacitor sensor with a resolution of 0.67 nm is used to measure the deflection of the sensor giving a force resolution of 3 μN. The stiffness is 62 $\mu N/nm$. The instrument uses a piezo-electric translator in a closed loop with a capacitance sensor to achieve a displacement resolution of 0.9 nm with a range of 15 μm. The instrument is used to indent copper with a spherically tipped conical indenter.

The surfaces are rough down to atomic scale. When the penetration depth is less than the asperity size, then an error is introduced in the hardness measured in depth sensing indentations. Depending upon the local geometry, there is a scatter in the measured hardness values. The nature of this error and the scatter is studied using experimental and numerical techniques.

The rough surface can be thought of as made up of hemi-spherical asperities carrying smaller hemi-spherical asperities which in turn carry still smaller asperities. The asperities with of radius comparable to the penetration depth will affect the hardness measurements while the other asperities are either too small or too large. This effect of single spherical asperity on the hardness measurement in a depth sensing indentation is studied using a macroscopic experiment. In this, a hemispherical specimen of copper is indented using a hardened steel ball. The measured hardness is found to be an explict function of the indentation geometry and bulk hardness.

To study the scatter introduced, numerical studies were carried out simulating the indentation of a rough surface. The rough surface is simulated using the Weierstrass-Mandelbrot fractal function. The load coming onto the rigid conical indenter with spherical tip is obtained using the spherical cavity model. The scatter is found to decrease with increasing penetration depth and, the variation in the material properties with deformation volume or penetration depth has very little effect on the scatter.

A phenomenological model is proposed in chapter 6 to characterise the error introduced in hardness measurements on a rough surface. Using this model, it is possible to correct the nano-indentation data for the surface roughness effect.

Acknowledgements

I thank,

Prof. S.K. Biswas	for	guidance, support, encouragement, freedom, technical inputs, intuitive inputs, forcing me to my limits, discussions, introducing the fascinating world of Contact Mechanics and Nanoindentation teaching the intricacies in research and a lot.
Prof. V.H. Arakeri, **Prof. S. Seshan**, **Prof. M.L. Munjal**	for	facilities and support.
Dr. S.V. Kailas	for	technical and non-technical inputs, time and energy.
labmates		
Dr. Arul Selvan	for	teaching me exploiting intuitions, numerous ideas and techniques, companionship and support during hard times.
Dr. Rajendra Kumar	for	setting an example for hard working and giving company during late night working.
Venkatesh	for	helping me out with experiments.
Shyamasundar	for	goodwill and Administrative support.
Pushpa	for	secretarial support.
Srinivas	for	hardware support.
Bhaskar	for	software support.
present and past **labmates**	for	letting me 'feel' at home

Professionals		
Govindaraju	for	introducing practicability into my design, and practical ideas.
Mr. Dube	for	manufacturing support
Technicians of Ducom, CMTI, HAL and IISc	for	helping to realise my crazy ideas.
friends		
Karthik	for	helping me out with *physics*.
Dani	for	introducing MATLAB, MATHEMATICA, TEX other software and computer support.
other loonie gang members	for	letting the IISc. life tickle with magnificent arguments.
Pradeep	for	teaching me fourier transforms.
Kanti	for	helping me out with electronics.
family members		
BO and AMBO	for	Understanding, Patience, financial and emotional support.
Kishore	for	waiting ...
Madan	for	inspiration, algo, and ideas
Deepa	for	typing and proof reading this thesis, patience and waiting...
Anger Ambo	for	encouragement.

and a lot of others who helped me directly and indirectly

Contents

Chapter 1

Introduction

Indentation experiments, with the aim of determining the properties of materials are being carried out for the last 100 years. From simple comparisons of relative hardness of different materials, these experiments have evolved today to act as a mechanical microprobe and attempts to determine mechanical properties at the level of single molecules. From testing of metals, the relative ease and speed with which the indentation tests can be carried out made it possible to extend the technique to test the properties of a variety of materials like soil, rock, organic monolayers, etc. The scale at which these indentations are carried out varies from few meters to few nanometers. Such a wide range in physical scale and the materials, makes it impossible to have a single theory that can explain all the mechanisms that underlie the responses obtained in indentation.

Clever usage of the indentation technique has resulted in measurement of properties other than hardness from the indentations. The fracture toughness of a brittle material can be obtained by measuring the length of the crack produced at the sharp edges of a Vicker's imprint. The microindentation techniques are used to find the case hardening depth, properties of the inclusions in an alloy etc. The list of properties that can be deconvoluted from the depth sensing indentation is increasing day by day.

Depth sensing indentation/continuous indentation mark a quantum leap in the development of indentation testing, from the classical apply load and measure the resulting impression types. Depth sensing experiments, record the complete deformation history of the indentation, through the load-displacement characteristics. By suitable interpretation of these curves various properties ranging from Young's modulus to the strain rate behaviour can be obtained.

The elimination of the limitation of the resolution of the optical microscope in measuring the imprint, in the depth sensing indentation paved the way to study the deformation characteristics of very small volume of materials. In early 70's Gane [36] had demonstrated that the yield strength of metals like gold depends on the volume of the deformation, the

strength increasing with the decreasing volume of material deformed. It has also been observed that the hardness increases with the decreasing indent size. The indentation size effect observed in the microindentation has remained inconclusive due to the inaccuracies in the measurement. Pethica *et al.* [82] were the first to show that the hardness of the materials do increase at the lower deformation volume, using depth sensing indentation.

Many possible reasons have been put-forth for the observed variation in hardness from presence of oxide layers, to the reduced dislocation source size to purely statistical artifacts, apart from the actual increase in strength. Few experimental evidence [1] do suggest that the yield strength of nanometer sized asperities approach the theoretical strength. However, the exact nature of strength variation with the deformation remains inconclusive. Apart from the instrumentation problem, the main reason for this seems to be the lack of proper modelling to interpret the data obtained from the experiments especially the indentation experiments, at the submicron level.

Macroscopic material behaviour is well modelled using continuum mechanics, while molecular dynamics simulations [51, 83] have started to throw light on the atomic scale behaviour. There exist no definite method to model the mesoscopic behaviour of the material, where the continuum assumptions breakdown and the present day computing power, limit the molecular dynamic simulations. Though an hybrid of these two approaches have been attempted [49], the best bet seems to be stretching the continuum mechanics with suitable assumptions and modifications [33]. For these attempts to succeed the main requirement is reliable and reproducible experimental data on different systems. Depth sensing indentation is evolving as a fast and reliable method of obtaining the mesoscopic material behaviour.

The deformation behaviour of very small volume materials needs to be understood clearly to realize the dream of micro-machines. Though rudimentary prototypes have been demonstrated, it is yet to be put to practical use widely. In order to cope up with the phenomenal growth rate in computational power, the access speed of the media storage devices has to be improved. The severe contact problems encountered brings about a need for understanding the mechanical behaviour at nanometric level. Depth sensing indentations seems to be the only way through which the properties of material of deformation volume in the range of few hundreds of nanometers can be determined.

Mechanical characterisation of thin films is another area where depth sensing indentations are being applied extensively. In order to measure the properties of the film without any substrate effect, the depth of indent made should be approximately $1/10^{th}$ the thickness of the film. Since the thickness of the thin films is few microns, the depth to which the

indent has to be made is less than 100 nm.

In order to use the depth sensing indentation more effectively in the range of 10 nm - 1000 nm, it is important to understand the mechanics of the indentation process. It is also important to know the sources of errors involved in the depth sensing indentation and either eliminate them or account for them by suitably processing the data obtained. The main aim of this thesis is to study the depth sensing indentation process and some of the inevitable errors involved and use the information obtained. to design an instrument capable of measuring deformation properties of the material by indenting to a depth of 10 nm - 1000 nm.

1.1 Brief History of Indentation

1.1.1 Early Experiments

Indentation of soft materials by a hard indenter is carried out to compare the properties of different materials since the beginning of this century. Brinell [20, 103] was first to carry out indentation tests using hard spherical indenter. The indenter is pressed under a fixed normal load onto the smooth surface and left for 15 to 30 seconds to reach equilibrium. The diameter of the resulting permanent deformation is measured to express the Brinell hardness number (BHN) as the ratio of the load P to the curved area of indenter as,

$$BHN = \frac{2\,P}{\pi\,D^2\ \left(\,1-\sqrt{1-(d/D)^2}\,\right)}$$

where D is the diameter of the spherical indenter and d is the diameter of the impression, P is in Kg_f and $D,\ d$ are in mm to get BHN in Kg_f/mm^2. BHN is not constant for a given material but depends on the load P and size of the indenter D.

The spherical indenters were later replaced by indenters of different geometry such as cone [59] (Rockwell), square pyramid [91] (Vicker's), pyramid with a parallelogram base [48] (Knoop's), triangular pyramid (Berkovich) etc. The advantage with these indenters is that *hardness number* is independent of the applied load as the indents at different load are geometrically similar [97]. Instead of measuring the impression, the depth of penetration of a conical indenter is measured in Rockwell tests.

The property of the material that is measured by these static indentation tests is termed as hardness and is defined as the resistance of the material to permanent deformation [97]. Physically, it is the mean pressure between the surface of the indenter and the indentation.

This mean pressure which is equal to the ratio of load to the projected area is termed as Meyer's hardness [66]. The (Meyer's) hardness has been related to several other properties and attributes such as the yield stress, the Young's modulus, the fracture toughness, the melting point, the resistivity, the magnetic properties, the wear resistance and the position in the periodic table [78].

The other two methods by which the hardness can be determined are scratch hardness and dynamic hardness [97]. In scratch hardness, the hardness is obtained from the width/depth of the scratch resulting from pulling a hard stylus under a normal load. In dynamic hardness measurements, an indenter is dropped onto the surface and the hardness is expressed in terms of the energy of impact and the size of the remaining indentation.

Tabor [97] was the first to give some physical reasoning to the indentation measurements. Empirically it was established that the indentation hardness (that is the pressure p_m over a fully plastic indentation) for a fully work-hardened metals is approximately three times its yield stress (Y_0).

$$p_m \;=\; H \;\simeq\; 3\; Y_0$$

For materials which are not fully work-hardened, the hardness is equal to three times the yield stress (Y_r) at some representative strain

$$H \;\simeq\; 3\; Y_r$$

The representative strain ϵ_r depends on the geometry of the indenter [27, 97].

$$\begin{array}{rcll} \epsilon_r & \simeq & 0.2\; d/D & \textit{for spherical indenters} \\ & \simeq & \tan\,\beta & \textit{for conical indenters} \end{array}$$

where β is the iclination of the face of the cone to the surface.

1.1.2 Modelling Indentations

The analytical treatment of indentation of a material is a difficult problem. Many models have been developed involving different degrees of idealisation and simplification. The two dimensional plane strain indentation of a rigid plastic material can be analysed using slip line method [26]. Axisymmetric perfectly-plastic indentations has been analysed for sphere [46] and for cone [64], by slip line method.

The elasticity of the materials plays an important role in plastic indentation process. When the yield point is first exceeded, the plastic strains are of the same order of magnitude as the surrounding elastic strains, as the plastic zone is contained by material which remains

elastic. On increasing the severity of indentation, the plastic zone expands and eventually breaks out to the free surface. The material is then free to escape by plastic flow to the sides of the indenter and the indentation can be analysed by the rigid-plastic approximation.

An exact analytical solution for the indentation of elastic-plastic material is very difficult to obtain, though in principle, it should be possible to calculate the contact stresses [46]. The simplest model developed by Marsh [64] and Johnson [45], assumes that the stress and displacements in an indentation is same as in an infinite elastic-perfectly plastic body containing a spherical cavity of size equal to the projected contact radius, of the indenter. For an incompressible material a simple expression for the mean pressure is obtained for a conical indenter as [46]

$$p_m \;=\; \frac{2}{3}\, Y_0 \left\{ 2 \;+\; \ln\left(\frac{E\ \tan\beta}{3\ Y} \right) \right\} \tag{1.1}$$

with Y_o as the yield stress, E as the Young's modulus of the material and β the inclination of the cone face to the surface. For a spherical indenter [46], the imposed strain is d/D instead of $\tan\theta$. Attempts [28] have been made either to improve upon this model, at the cost of simplicity or to propose altogether different models [14, 111] with other approximations.

Numerically, finite element methods have been employed to analyse the elastic-plastic indentation by a cylinder [31], sphere [41, 53], cone [9], rectangular pyramid [34] and triangular pyramid [71]. More complicated material models such as strain hardening materials [9, 38], strain rate sensitive materials [16], thin films on substrates [10] have been analysed. The expression for the average pressure during indentation for an elasto-plastic, linear strain hardening material can be written as [115],

$$p_m \;=\; k_1\ Y_0 \ \left(\ 1 \ + \frac{Y_{0.3}}{Y_0} \ \right) \left\{ 1 \ + \ \ln\left(\frac{E\ \tan\beta}{3\ Y} \right) \right\} \tag{1.2}$$

The constants k_1 and the imposed strain term $\tan\beta$ depends on the geometry of the indenter. $Y_{0.3}$ is the yield stress at the plastic strain of 0.3 and Y_0 is the yield stress at zero plastic strain. The values of k_1 and β are 0.297 and 22^o for Vicker's indenters and 0.245 and 24.7^o for Berkovich indenters [115].

1.1.3 Micro and Nano Indentations

In a conventional indentation experiment carried out, to measure the hardness of the materials, the applied loads are of several kilogram force. In micro indentation [22, 69], the applied load is 1000 times smaller and the resulting impression size is of the order of microns. This technique has been used to study the deformation properties of grain boundaries, of alloy

constituents, of particulate inclusions. The interesting observation is that the hardness measured in micro indentations is found to be dependent on the load applied and increases at lower loads. Various explanations have been provided ranging from pure statistical artifact due to error in measurements [114] to the limited number of dislocations in the small volumes being deformed [22]. Different physicochemical mechanisms that could produce this indentation size effects has been reviewed by Sargent [87].

If the load applied to the indenter is decreased below the load used in micro indentation, the size of the indent becomes smaller than that can be resolved using optical microscopes. Such indentation experiments are called nano indentation and the hardness measured as nano hardness. Many techniques have been used to get the projected area of indent which can be broadly classified into two categories.

1. Imaging method and

2. Depth sensing method

In imaging method, the indent is "viewed" using techniques other than optical such as scanning electron microscope [6] or atomic force microscopes [11] which has atomic resolution. In depth sensing method, the penetration depth of the indenter into the material is measured and the projected area is deduced from the known geometry of the indenter [82]. The continuous recording of the penetration depth as the function of the applied load in this method can be used to determine material properties other than hardness.

From the simple application to compare the relative 'hardness' of the materials, the indentation experiments have now evolved to determine a plethora of mechanical properties of the material by suitably interpreting the measured load-displacement curve. The appearance of this characteristic curve can serve as a mechanical "finger print" of the material response [79].

1.2 Depth Sensing Indentations

1.2.1 Load *vs* Displacement

Depth sensing indentations involve continuous measurement of load supported by the material and the displacement of the indenter as the indenter penetrates the material. A typical load *vs* displacement curve resulting from such an experiment may be seen in figure 1.1. The indenter establishes the contact with the material at A and the load increases along AB, the

loading curve, as the indenter penetrates the material. BC is the unloading curve. If the material is perfectly elastic and has no hysterisis, then AB and BC will be identical. AC gives a measure of permanent deformation, if the material is not elastic.

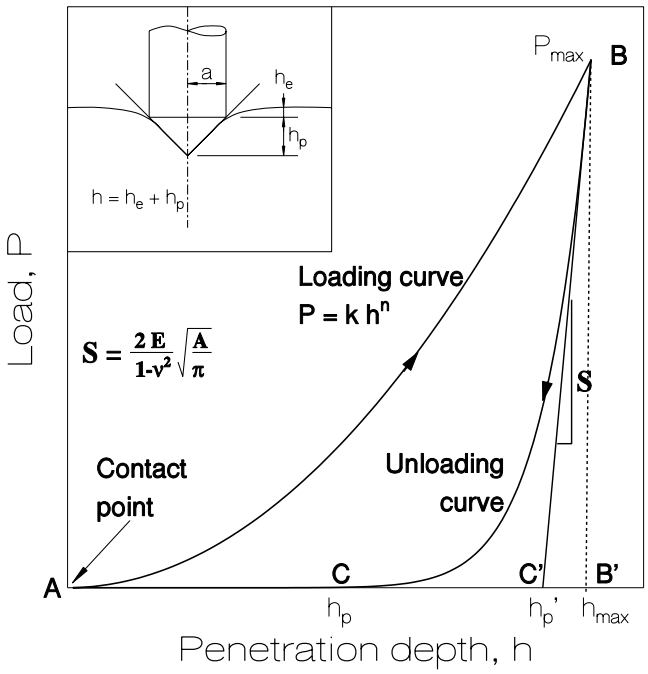

Figure 1.1: Typical Load - Displacement curve

The area ABB' gives the total work done on the material, the area CBB' represents the amount of energy that has been recovered elastically and the area ABC gives the energy that has been used to create the permanent impression. For a perfectly plastic material, there is very little elastic recovery hence area $BB'C \rightarrow 0$, while for a perfectly elastic material area $ABC \rightarrow 0$.

The theoretical determination of the relation between P and h for elasto–plastic materials is a difficult problem. Finite elements methods have been used to solve this problem [9, 10, 38, 71]. These results show that the loading curve is quadratic, i.e

$$P = k_{ep}\, h^2 \tag{1.3}$$

for indenters which give rise to geometrically similar indents like cone, Vicker's and Berkovich. For a spherical indenter the relation is linear. More generally, the relation between P and h

can be written in power law form [90] as

$$P \;=\; k\; h^n \tag{1.4}$$

A simple relation between k_{ep} of equation 1.3 and the material properties, Young's modulus (E), Poisson ratio (ν) and Yield strength (Y) can be obtained by assuming that the elastic and plastic behaviour of the material can be dissociated [56], i.e.

$$P \;=\; k_e\; h_e^2 \;=\; k_p\; h_p^2 \tag{1.5}$$

where k_p is a function of yield strength Y or hardness H, k_e is a function of E, ν and the indenter angle (θ). The equations 1.5 can be thought of as that of two springs one elastic and the other plastic. The total penetration is sum of elastic (h_e) and plastic (h_p) contributions, (i.e. the springs are in series)

$$h \;=\; h_e \;+\; h_p$$

substituting from equation 1.5

$$\left[\frac{P}{k_{ep}}\right]^{\frac{1}{2}} \;=\; \left[\frac{P}{k_e}\right]^{\frac{1}{2}} \;+\; \left[\frac{P}{k_p}\right]^{\frac{1}{2}}$$

$$i.e. \qquad k_{ep} \;=\; \left[{k_e}^{-\frac{1}{2}} \;+\; {k_p}^{-\frac{1}{2}}\right]^{-2} \tag{1.6}$$

k_p can be obtained from the hardness definition. For Vicker's hardness,

$$H \;=\; \frac{\cos^2\theta}{4\;\sin\theta}\;\frac{P}{h^2}$$

$$k_p \;=\; \frac{4\;\sin\theta}{\cos^2\theta}\;H \;=\; 26.4\;H \tag{1.7}$$

k_e can be obtained from the relation between P and h_e in the case of a nonadhesive rigid, cylindrical flat punch normally loaded on the plane surface of a smooth elastic body [93].

$$P \;=\; \frac{2\;E}{1-\nu^2}\;a\;h_e \tag{1.8}$$

where a is the radius of contact area (inset of figure 1.1) and is the same as the one given by plastic penetration. For Vicker's indentation

$$\pi\;a^2 \;=\; \frac{D^2}{2} \tag{1.9}$$

where D is the diagonal of the impression and can be obtained from the definition of hardness as

$$D = \left(1.854 \frac{P}{H}\right)^{\frac{1}{2}} \tag{1.10}$$

from equations 1.8, 1.9 and 1.10,

$$P = \left(\frac{E}{1-\nu^2}\right)^2 \frac{1.18}{H} h_e^2$$

hence,

$$k_e = \left(\frac{E}{1-\nu^2}\right) \frac{1.18}{H} \tag{1.11}$$

substituting equations 1.7 and 1.11 in equation 1.6, k_{ep} can be obtained as a function of material properties.

During unloading, if the material is rigid plastic, then the penetration remains the same as that at maximum load. The unloading path will be AB' in figure 1.1. However, if the material is elasto-plastic then the part of the displacement is recovered elastically (AC). There are two components in this elastic recovery. One corresponds to the recovery of the elastic deformation of the half-space and the other is due to the recovery within the indent. During initial stages of unloading, the recovery of the half-space is much more than the recovery of the impression. Hence during initial unloading stages the load-displacement characteristics can be approximated to that of an elastic flat punch which has a base area equal to the projected area of the indentation. The relation is linear and is given by

$$P = \frac{2\,E}{1-\nu^2}\, a\, (h - h'_p) \tag{1.12}$$

for Vicker's indentation, this equation can be used to determine the Young's modulus as

$$\frac{2\,E}{1-\nu^2} = \frac{P_{max}\,\sqrt{2\,\pi}}{2\,D\,(h_{max} - h'_f)} \tag{1.13}$$

1.2.2 Hardness from Depth Sensing Indentations

Hardness is calculated as the load divided by the projected area of the permanent indent. In depth sensing indentation experiments, the projected area is obtained from the penetration depth of the indenter, known the geometry of the indenter. There are three different depths that can be used to obtain the projected area for a given load. They are

1. the maximum penetration h_{max} (figure 1.1)

2. the plastic depth h_p and

3. the depth $h_p^{'}$ obtained as the intersection of the tangent (BC') to the unloading curve at P_{max} and the X-axis.

For a material that exhibits only a small amount of elastic recovery and thus approximates the rigid-plastic model, the depth for estimating the projected area can be taken as the depth at the highest load point (h_{max}). However many materials show considerable amount of elastic recovery and h_{max} would underestimate the hardness. It has been shown using finite element calculations [9] that using the depth $h_p^{'}$ gives a better estimation of the hardness. Since the equation of line BC' depends only on the elastic properties E, ν of the material and is independent of the geometry of the indenter, the area of the indent at any point along the loading curve can be obtained using equation 1.12 and the area function of the indenter. Thus from a single indentation experiment, it is possible to obtain the hardness of the material as the function of the indentation size.

The area function of the indenter, which gives the cross sectional area of the indenter from the penetration depth can also be obtained from the unloading curves. This is important because the indenters are invariably blunt to a radius of 100 to 1000 nm. Equation 1.12 can be rewritten for an indenter of general geometry as

$$E = \frac{1 - \nu^2}{2} \sqrt{\frac{\pi}{A}} \frac{dP}{dh} \tag{1.14}$$

with A as projected contact area and dp/dh as the slope of the initial unloading portion. Since the Young's modulus of the material is independent of the deformation, this expression can be used to obtain A as function of h_{max}, if $\frac{dp}{dh} |_{h_{max}}$ is measured experimentally for different penetrations (h_{max}).

Careful experiments [82], show that the hardness of a variety of materials is dependent on the size of the indent made when the penetration depth is less than 1000 nm. Various reasons ranging from purely statistical error [114] to the decrease in the defect concentration in the deformed material [82] has been proposed. It is also observed that the scatter in the measured hardness value increases with the decreasing penetration depth. Some possible mechanisms for these effects are studied as a part of this thesis work.

1.3 Errors in Depth Sensing Indentations

1.3.1 Contact Point

The penetration depth, that is used to calculate the projected area in depth sensing indentations in order to arrive at hardness is to be measured from the surface of the specimen. As the indenter is moved towards the surface of the specimen, the load remains zero and the displacement which is usually measured with respect to some machine reference increases. In load controlled instruments, the initial portion of the $P - h$ curve will be linear with the slope corresponding to the stiffness of the indenter holding mechanisms. Once the indenter comes in contact, the load starts to increase with penetration. The exact contact point is lost in the scatter of the measured values due to instrument noise [102]. Even if the noise is ideally not present, the error introduced will be of the order of the force and displacement resolution of the instrument.

If h_i is the error in determining the contact point, then the measured hardness is

$$H_m \;=\; \frac{P}{A(h)} \;\propto\; H\;\frac{A(h \;\pm\; h_i)}{A(h)}$$

where H is the actual hardness of the material and $A(h)$ is the area function that gives the projected area from the penetration depth h. Approximating the blunt indenter to be spherical tipped,

$$H_m \;\propto\; 1 \;\pm\; \frac{h_i}{h}$$

This is very similar to the genuine trends in hardness variation with penetration [82].

The error in the determination of contact point can be minimised by fitting a suitable regression curve to the initial data points of the $P - h$ curve and extrapolating to zero load [65]. A method based on statistical testing has been developed in this thesis for a displacement controlled machine (section 3.3.3).

Increasing the resolution of the instrument is not going to solve the problem of contact point, as the surface forces such as Vander Walls, capillary, electrostatic, adhesive etc., will produce a sudden jump to contact when the separation between the sample and the indenter is few nanometers [24]. Complicated instrumentation would be needed to overcome this difficulty [43].

1.3.2 Indenter Tip Shape

The tip of any real indenter is blunt on a nanometric scale, with the effective radius of order of tens of nanometers or more. This results in an error in the area function $A(h)$ as obtained from the ideal geometry of the indenter. There are several ways in which the actual area function for a given indenter could be obtained. One technique is to make a series of known properties, calculate the contact areas from the size of indents measured by direct imaging and determine the effective depth of penetration as the depth corresponding to an ideally sharp indenter with the same projected contact area [30, 82]. Another method uses equation 1.14 to determine the contact area from the measured compliance dp/dh of a specimen with known Young's modulus (E) and fits a suitable polynomial $A(h)$ to the values A obtained from various depths h [77]. A third approach utilises the fact that for an ideally sharp indenter, the load is proportional to the square of the depth of the penetration. A regression line is fitted to the data obtained by testing a standard material and the correction values are calculated for small depths of penetration as the difference between the observed and ideal values [7]. Another alternative is to directly image the indenter using scanning electron microscope or otherwise and determine the geometry of the indenter (section 3.4.2).

1.3.3 Surface Roughness

Except for the carefully cleared surfaces of the single crystals, no surface is ideally smooth. Even the best polished specimens have surface undulations with height from several nanometers to several tens of nanometers and with distances between the individual peaks at tens of nanometers or more. As a result of this, the indenter, at the initial stages of loading, touches only at a few points, and the effective contact area for a given penetration depth is less than the area as given by the area function. The effect of surface roughness could be taken into account by introducing a correction to the measured penetration depths [102, 104]. The influence of surface roughness on hardness measurements is studied in some detail in this thesis (Chapters 4, 5 and 6). By suitable post processing of the data, it is possible to eliminate the error introduced due to surface roughness alone [15, 18].

1.3.4 Pile Up

In the case of soft ductile materials and in soft films on a hard, stiff substrate, the material surrounding the impression caused by the penetrated indenter could pile up along the contact perimeter [27, 96]. This results in a larger contact area than the area obtained from the

measured penetration depth. Further if the material is strain rate sensitive, then the pile up would depend on the rate of loading. The only way the pile up could be determined is by imaging the impression suitably using atomic force microscopy or profilometer. It is further complicated by the fact that some of the piling up could be occurring during the unloading stage.

1.3.5 Rate of Penetration

Most of the indentation experiments are carried out either at constant loading rate or at constant rate of penetration. The average strain rate during indentation can be written as [84]

$$\dot{\epsilon} \propto \frac{1}{h}\frac{dh}{dt}$$

Thus the strain rate vary during an indentation experiment and is very high at smaller penetration depths. If the yield stress of the material depends on the strain rate then this will introduce an error/variation in the hardness measured at very small penetrations. Further due to finite stiffness of the measuring system, there is bound to be a sudden impact when the indenter comes in contact with the specimen due to various surface forces. This would introduce an error in the hardness measured at the small penetrations. The effect of rate of penetration on a strain rate sensitive material is studied using finite element methods by Bobji and Biswas [16].

1.3.6 Thermal Drift

Any change in temperature will produce a change in length of the structure supporting the indenter and the specimen of the order of $10^{-5}\ m/m^oK$. The magnitude of this displacement could be comparable to the penetration of the indenter. For example, if the distance between the reference point and the point where displacement is measured is about 10 mm, then the thermal drift will be about 100 $nm/^oK$. The errors due to thermal drift can be greatly minimised by allowing sufficient time for the instrument to come in thermal equilibrium with the surroundings and carrying out the whole experiment as fast as possible such that the change in temperature during that period is very very small. It is also possible to measure the thermal drift just before the experiment and/or just after the experiment and introduce proper correction in the data. The other alternative is to enclose the whole instrument in a temperature controlled chamber.

1.3.7 Noise

The thermal fluctuations, mechanical vibrations and the electrical interference may cause a random fluctuations in the measured output. It is next to impossible to completely eliminate these random fluctuations, but is very easy to minimise most of them by proper design of the instrument and locating the instrument away from the sources of these disturbances.

Since these errors are random in nature, the best way to account for them is by repeating the experiments a number of times and taking the average. Simple statistical procedures can be used to determine the confidence interval for the measured quantities and to determine the number of tests required for a given degree of accuracy.

1.3.8 Compliance of the Measuring System

The measuring system, including the indenter, specimen holder, supporting structure etc., have a finite stiffness and acts as a spring in series with the specimen. It is possible to measure the compliance directly and correct for it after acquiring the data. It is also possible to obtain the compliance of the system by plotting dp/dh of the unloading curve for different max. penetration depths h_{max} against the reciprocal of the depth $(1/h_{max})$. The Y-intercept of the straight line fitted to this curve will give the compliance of the system [30].

1.4 Scope of the Present Work

1.4.1 Indentation Modelling

Spherical cavity model [45, 64] is the simplest and yet the most effective model for indentation of an elastic–plastic half space by a hard indenter. The mean pressure(p_m) under the indenter, obtained through this model (equation 1.1) in terms of material properties like E, ν, & Y matches well with experimentally observed values [46], when the values of mean pressure is less than approximately three times yield stress. For the higher values of mean pressure the indentation is fully plastic and the dependence of p_m on Young's modulus can be ignored. The main disadvantage of this model is that the stresses on the free surface do not reduce to zero.

Blister field model [111], describes the stress field in the elastic hinterland of the indentation. In this model, the stresses due to the elastic-plastic indentation is equated to the sum of the stresses due to a point load and a strain nucleus – blister. *Ab initio* determination of the strength of the blister field is however not been available so far, only qualitative

description using arbitrary factors have been suggested. It is shown in chapter 2 that an estimate of the strength of the blister can be obtained *ab initio* from the energy conservation arguments. The input energy, obtained from the load-displacement graph ABC (figure 1.1) is equated to the elastic strain energy and the energy of the core that generates the blister field. Macroscopic depth sensing experiments with the continuous recordings of surface strains were carried out on copper and alumina. The theoretical estimates of the strength of the blister field is compared with those obtained from the radial strain measurements.

1.4.2 Design and Fabrication of a Nano Indenter

A displacement controlled instrument capable of measuring the mechanical properties of materials by indenting to a depth of few tens of nanometer to few hundreds of nanometers has been designed and fabricated. The design lays emphasis mainly on characterising the various errors and correct the data after the experiment has been completed. It uses a piezo electric translator for generating the displacements and uses capacitance sensors for measuring them. The main innovation in this design is the use of flexible hinges as a force sensor. This overcomes the disadvantages of using a cantilever (as in atomic force microscopes) - the inability to separate the geometry, the sensitivity and the stiffness of the sensor. This force sensor uses a system of levers to magnify the displacement thus increasing the sensitivity without sacrificing the stiffness.

The flexible hinges were fabricated out of the aluminium alloy AU4G1 (table 3.2) using wire cut electro-discharge machining. The feed back from the fabrication has been used to improve the design. The final design is a product of three such main interactions. In chapter 3, the instrument design and the working principle are explained in detail. The capability of the instrument has been demonstrated by indenting a copper specimen with a conical diamond indenter.

1.4.3 Rough Surface Indentation

It is a well known fact that surface roughness affects hardness measurements, if the surface undulations are much smaller than the indentation size [97]. For hardness measurements carried out with a penetration depth which is comparable to the size of surface undulations, the local geometry of the rough surface will have appreciable effect on the measured hardness. It is possible to reduce roughness of the surfaces by polishing but only to an extent determined by the processing parameters. From a practical point of view, since hardness measurement

is a fast and reliable method of determining the mechanical properties of a material, it is not desirable that the specimen preparation should take up a lot of time and should need high sophistication.

While characterising the thin films, the penetration depths to which an indentation is to be carried out, is limited by the thickness of the film. Depending upon the hardness of the film and the substrate, the penetration at which the substrate starts to influence the measurement of the thin film hardness varies from 0.06 to 0.4 times the film thickness [32]. The roughness of the film is approximately the same as that of the substrate. The R_a value for mirror finish is of the order of 0.1 micron. Thus, in most of the indentations carried out to measure the thin film properties on films with thickness less than 1 micron, the roughness of the surface is comparable to the penetration depth.

The effect of surface roughness on the hardness measured is studied experimentally as well as numerically. Rough surface can be thought of as made up of hemispherical asperities of gradually decreasing radii riding on the back of the previous larger asperity [3]. Any real indenter is blunt and tip can be approximated to be spherical. When such an indenter comes in contact with a rough surface, the indentation can be modelled as a contact between two spherical bodies, for smaller penetration depths. Such single asperity contact is studied in chapter 4, experimentally. To isolate the effect of surface geometry from other surface effects observed at micro and nanometric levels, the problem is zoomed up and the experiments are carried out with a spherical indenter with a diameter of 25 mm. The hardness values as estimated in a depth sensing indentation is found to depend strongly on the curvature of the asperities relative to the indenter and weakly on the location of the contact on the spherical surface.

As the indenter penetration increases, the asperity in contact deforms plastically and the neighbouring asperities come into contact and a multiple asperity contact is established. The hardness measured depends on the local distribution of the asperities near the point of first contact. This results in a scatter due to the measurements being made at different points on a rough surface. Chapter 5 reports the detail of the numerical simulation carried out to quantify this scatter. The rough surface is simulated using Weierstrass-Mandelbrot function, and the indentation is simulated using spherical cavity model. The scatter is found to increase with the decreasing tip radius of the indenter and decrease with the cone angle for a given penetration. It has been found that the scatter follows a power law relation with the nominal contact area.

Based on the above studies, a model is proposed in chapter 6 to characterise the

variation of hardness with penetration of the rough surface. The hardness measured at a particular penetration depth on a rough surface can be approximated to the hardness measured on a spherical asperity whose radius of curvature depends on the surface roughness and the penetration depth. This radius varies from a very small value at the point of contact to infinity (i.e. flat surface) for penetration much greater than the surface undulations. The exact nature of this variation will depend on the nature of the surface roughness and the indenter geometry. The first order model developed on these premises has been verified using numerical simulation for a Weierstrass-Mandelbrot fractal surface and a conical indenter with a spherical tip.

Chapter 2

Strength of the Blister Field

2.1 Introduction

Unlike the conventional indentation tests, which gives information only about the final residual state of the material, the depth sensing indentation records the response throughout the indentation process. Since the permanent deformation resulting from the indentation is path dependent, the depth sensing indentation can be effectively used in modelling the indentation behaviour of the materials. This fact is used in this chapter to determine the strength of the blister field which decides the nature of the stresses in the elastic hinterland of the indent.

The configuration of an indent may be idealised as one consisting of a core which envelopes the indent and a hinterland of half space outside the core. The core consists of highly deformed or compacted material. The hinterland is bounded by the boundary of the core and a surface free of shear stresses and normal stress perpendicular to that surface. During the loading cycle of indentation, as the size of indent increases, the boundary of the core expands and the hinterland is strained. On unloading the hinterland does not fully recover as it is restricted by the permanently displaced core boundary. This gives rise to residual stresses and the elastic energy is stored in the hinterland. This residual strain energy increases as the core expands due to an increase in indentation load.

The most well known model of elastic plastic indentation, the spherical cavity model [45, 46, 64] is an adaptation of Hill's [42] spherical cavity solution. Shape of the core in this case is always hemispherical. An application of hydrostatic pressure, equal to the indentation pressure, in the core, strains the hinterland. As the core expands, due to increasing indentation load, the stresses increase in proportion to $ln(r)$ and as $1/r^3$ in the elastic hinterland, with r as the radius of a point in the hinterland. In modelling indentation, Hill's spherical cavity is diametrically sliced to generate planes bounding two half spaces. This leaves hoop

stresses on the free surface of both the half spaces. According to this model the core on unloading is constrained to shrink elastically as a hemisphere. An attempt had been made by Chiang, Marshall and Evans [28] to eliminate the normal surface stresses of the spherical cavity model by superposing the stresses due to Mindlin's [67] point force solution on Hill's stress field.

Ghosal and Biswas [37] have compared the surface radial strains predicted by the original and the amended versions of the spherical cavity solution with those measured experimentally during indentation of copper by a conical indenter. The spherical cavity models were found to over estimate the strains during loading and to predict incorrectly the nature of change in the strain during the unloading part of the cycle. The experimental results showed that a point on the free surface displaces away from the indenter axis, on unloading. Stillwell and Tabor [95] have also shown that for metals the recovery on unloading occurs principally in depth. The FEM work of Yokouchi, Chou and Greenfield [112, 113] have shown that the displacement vector of a free surface element swings away from the indentation axis on unloading.

An alternative approach would be to relax the constraint of spherical symmetry imposed on displacement such that the corresponding normal stress on the free surface is zero. The displacement field corresponding to the loading of a surface by two outward double forces in the surface plane and an inward double force of equal magnitude normal to it, satisfies this requirement. The field is not spherically symmetric but axisymmetric, as a hemisphere on loading expands near the surface while it contracts in depth. The corresponding stress field is proportional to $1/r^3$. In Love's [57] terminology this stress field is generated by a nucleus of strain situated on the free surface. Yoffe [111] described it as a stress field generated by a similarly situated blister or an inclusion. If a strength B is now attributed to the strain nucleus or blister the stresses are proportional to B/r^3. As these stresses are however highly local in nature, Yoffe suggested superposing the stresses due to Boussinesq point-load solution ($\propto\ P/r^2$) on these to take care of the far field support of the load in the indentation problem.

In the cylindrical coordinate system $r,\ \theta,\ \phi$ (figure 2.12), the stresses in the elastic half-space, for the blister field superposed on the Boussinesq solution are,

$$\sigma_{rr} = \frac{P\ (1-2\,v-2\ (2-v)\cos\theta)}{2\,\pi\,r^2} + \frac{4\,B\ (-2+v+(5-v)\cos^2\theta)}{r^3}$$

$$\sigma_{\theta\theta} = \frac{P\ (1-2\,v)\cos^2\theta}{2\,\pi\,r^2\ (1+\cos\theta)} + \frac{-2\,B\ (1-2\,v)\cos^2\theta}{r^3}$$

$$\begin{aligned} \sigma_{\phi\phi} &= \frac{P\,(1-2\,v)\,(\cos\theta - 1/(1+\cos\theta))}{2\,\pi\,r^2} + \frac{2\,B\,(1-2\,v)\,(2-3\cos^2\theta)}{r^3} \\ \sigma_{r\theta} &= \frac{P\,(1-2\,v)\cos\theta\,\sin\theta}{2\,\pi\,r^2\,(1+\cos\theta)} + \frac{4\,B\,(1+v)\cos\theta\,\sin\theta}{r^3} \end{aligned} \tag{2.1}$$

The corresponding displacements are,

$$\begin{aligned} u_r &= \frac{P\,(-1+2\,v+4\,(1-v)\cos\theta)}{4\,G\,\pi\,r} + \frac{B\,(2\,(1-v)-(5-4\,v)\cos^2\theta)}{G\,r^2} \\ u_\theta &= \frac{2\,B\,(1-2\,v)\cos\theta\,\sin\theta}{G\,r^2} + \frac{P\left(-((3-4\,v)\sin\theta) + \frac{(1-2\,v)\,\sin\theta}{1+\cos\theta}\right)}{4\,G\,\pi\,r} \end{aligned} \tag{2.2}$$

and the radial strain is

$$\epsilon_{rr} = \frac{-\left(P\,(-1+2\,v+4\,(1-v)\cos\theta)\right)}{4\,G\,\pi\,r^2} - \frac{2\,B\,(2\,(1-v)-(5-4\,v)\cos^2\theta)}{G\,r^3} \tag{2.3}$$

Yoffe [111] has used this approach to correctly predict the types of crack initiated in the indentation of soda lime glass. Mukhopadhyaya and Biswas [70] and Ghosal and Biswas [37] have demonstrated that using this approach it is possible to correctly predict the nature and variation of free surface radial strains generated during the indentation of alumina–clay composite and copper respectively.

Predicting the correct surface strains, is very important in understanding and modelling the indentation size effect observed in the nano-indentation. Developments in nanofabrication techniques, has made it possible to measure surface strains at nanometric scale. An array of markers, either mounds of atoms made by electrical nanofabrication or indentations made by mechanical nanofabrication, can be made on the surface, with a pitch of about 50 nm. The surface residual strains could be measured, by measuring the relative displacements of these markers using scanning probe microscopes [68]. This would provide an independent means of confirming and characterising the high strength exhibited by the materials when deformation volume is very small.

Cook and Pharr [29] and Tabor [98] have commented on the effectiveness of the Yoffe's approach, especially in modelling indentation of brittle solids. The approach clearly has a great potential for modelling the indentation process. Any extensive use of the method is however restricted, as has been pointed out by Tabor [98] by the fact that the value of the strength of the blister field B is not known *ab initio.*

The strength of the blister field may be estimated by considering the extra volume (displaced by indentation) maintained within the core [29, 111]. This provides a sensitivity of the strength of the blister field to material porosity and the applied strain. For quantification

Cook and Pharr [29] multiplies the extra volume by a compactability factor. Yoffe [111] and Cook and Pharr [29] discuss the fracture mechanics of glasses and ceramics by quantifying B by this method or by observing the continuity of the radial and shear stresses across the core boundary. The volumetric method suffers from the uncertainty of assigning the compactability factor. Yoffe has discussed the difficulty of arriving at a single value of the strength of the blister field by the stress continuity method.

According to the spherical cavity model the stresses in the hinterland are caused by pressures which are in equilibrium with applied load while they act on the core boundary. These stresses are thus a function of the applied load and the mechanical properties of the material. If the stresses due to the nucleus of strain or blister are now considered as a legitimate component of the total stresses in the hinterland they may also be associated analogously with the magnitude of the applied load and the mechanical properties of the deforming body. Given this, the proportionality term B which has been called the strength of the blister, may also be considered as a function of the applied load and the mechanical properties of the material.

An attempt has been made here to derive an estimate of B by applying the principle of energy conservation. The energy input into the system is considered to be made up by two parts. The first part is dissipated in the core in giving rise to large scale permanent deformation by compaction or flow. The second part is dissipated in straining the elastic hinterland and thus giving rise to stresses which are proportional to B/r^3 and P/r^2 . The strength of the blister field, B is estimated as a function of known mechanical properties such as hardness, Young's modulus and Poisson's ratio as well as the normal load. The estimates are compared with those calculated from measured radial strains on the free surface. The study is done for pure copper and alumina using 150^o and 90^o diamond cones by depth sensing indentations.

2.2 Theory

2.2.1 Loading

In the loading part of the indentation cycle, a stress field is created in a core adjacent to the indenter tip. Yoffe [111] proposes a pressure field in the core which is in equilibrium with the mean pressure applied by the indenter. Outside the core the half space is elastic where the stresses are as given in the equations 2.1. It is proposed here to estimate the strength of the blister from an equation which equates the energy input E_i to the system by the indenter to

the sum of the elastic energies of the core E_c and the elastic hinterland E_H.

$$E_i = E_c + E_H \tag{2.4}$$

2.2.1.1 Input Energy

The load-displacement characteristics in indentation is quadratic in nature [52, 95]. The work done by the indenter is the area under this characteristics.

$$Work \;\; done = \int_{h_o}^{h_{max}} P dh \tag{2.5}$$

where h_o and h_{max} is the initial and maximum depths of indentation respectively and P is the load on the indenter for the penetration depth of h.

The stiffness of the material k against indentation is given as [56]

$$k = \frac{P}{h^2}$$

If the material is now considered as made up of two springs in series representing elastic and plastic behaviour,

$$P = k_e h_e^2 + k_p h_p^2$$

where

$$h = h_e + h_p$$

The equivalent stiffness is, (equation 1.6

$$k \;\; = \;\; \left(\frac{1}{k_e^{0.5}} \;\; + \;\; \frac{1}{k_p^{0.5}} \right)^{-2}$$

Loubet *et al.* [56] model the indentation cavity as made up of a recoverable elastic indentation depth h_e created by a flat punch of radius a and an irrecoverable conical plastic indentation depth h_p. If it is now noted that the hardness of the material $H \;\; = \;\; P/\pi a^2$ and the contact radius of the impression $a \;\; = \;\; h_p \;\; \tan\alpha$, then

$$k_p \;\; = \;\; \pi H \tan^2 \alpha$$

Using Sneddon's [93] relation for flat-punch elastic indentation,

$$k_e \;\; = \;\; \frac{P}{h_e^2} \;\; = \;\; P \; \frac{16G^2a^2}{P^2(1-\nu)^2} \;\; = \;\; \frac{16G^2}{\pi H(1-\nu)^2}$$

Substituting in equation 2.5 gives

$$E_i = \frac{k h_{max}}{3} = \frac{P^{1.5}}{3k^{0.5}} = \frac{a^3}{3} \;\; \left(\frac{\pi^2 H^2 (1-\nu)}{4G} \;\; + \;\; \frac{\pi H}{\tan\alpha} \right) \tag{2.6}$$

2.2.1.2 Core Energy

This is approximated to the strain energy of the blister. Yoffe [111] describes the stress field in the blister in terms of an uniform pressure $p_m = P/\pi a^2$ and a containing pressure q normal to p_m. Noting the relationship $q = \nu p_m/(1-\nu)$, required to give minimum elastic strain energy density, the elastic strain energy per unit volume is given by

$$\frac{(1-\nu-2\nu^2)}{(1-\nu^2)}\ \frac{p_m^2}{4G}$$

Since the core volume under the indenter (being the hemispherical volume less the volume of the indent in the half-space [111]) is $\pi a^3(2-\cot\alpha)/3$. Therefore the core energy is

$$E_c = f_1(2-\cot\alpha)\frac{p_m^2 a^3}{G} \quad \text{where} \quad f_1 = \frac{\pi}{12}\,\frac{(1-2\nu)}{(1-\nu)}$$

Noting $p_m = H$,

$$E_c = f_1(2-\cot\alpha)\,\frac{H^2 a^3}{G} \tag{2.7}$$

2.2.1.3 Strain Energy Outside the Core

The strain energy in the region outside the core is given by,

$$E_H = \frac{1}{2}\int_s (U_r\sigma_{rr} \ + \ U_\theta\sigma_{r\theta})\,ds$$

where s is the hemispherical surface area of radius a.

Yoffe [111] gives the stress and displacement fields by superposing the contributions from the Boussinesq and blister fields. Substitution of equations 2.1 and 2.2 and integration gives

$$E_H = f_2\frac{H\,a^3}{G} \ - \ f_3\frac{H\,B}{G} \ - \ f_4\frac{B^2}{G\,a^3} \tag{2.8}$$

where f_2, f_3 and f_4 are functions of ν as given in table 2.1.

	f_2	f_3	f_4
$\nu = 0.33$	0.84744	2.80481	17.8426
$\nu = 0.25$	0.88877	3.14159	19.4779

Table 2.1: Values of f2, f3, and f4 as a function of ν

2.2.1.4 Blister-field Strength

Substituting from equations 2.6, 2.7 and 2.8 into equation 2.4 gives

$$\frac{f_2 H^2 a^3}{G} - \frac{f_3 HB}{G} + \frac{f_4 B^2}{Ga^3} + f_1(2-\cot\alpha)\frac{H^2a^3}{G} = \frac{\pi^2 H^2 a^3}{3}\left(\frac{1-\nu}{4G} + \frac{1}{\pi H \tan\alpha}\right)$$

rearranging this we get,

$$f_4\left(\frac{B}{Ha^3}\right)^2 - f_3\frac{B}{Ha^3} + f_2 + f_1(2-\cot\alpha) - \frac{\pi^2}{3}\left(\frac{1-\nu}{4} + \frac{\cot\alpha}{\pi}\frac{G}{H}\right) = 0 \qquad (2.9)$$

This is a quadratic equation in B/Ha^3 which can be solved to give B/Ha^3 as a function of α, which is a function of applied strain ($\approx 0.2\cot\alpha$) [4] and the material properties G, H and ν. Thus for a given material, B is directly proportional to $p^{1.5}$, since $a^3 = (P/\pi H)^{1.5}$

For copper, the solution of equation 2.9 gives for a range of α ($30^o < \alpha < 85^o$).

$$B = P^{1.5}\left(2.8\times10^{-4} + 1.3\times10^{-2}(\cot\alpha)^{0.5}\right)$$

2.2.2 Unloading

In the unloading part of the indentation cycle, the input energy is recovered by the punch withdrawal. As the load is reduced, elastic strain energies corresponding to the core as well as the Boussinesq component of the stress field outside the core are reduced. To maintain the validity of equation 2.4 in this new situation, the blister field adjusts itself by reducing its strength. Validity of an *ab initio* estimation of the input as well as the core energies and therefore the residual stresses during unloading is clearly dependent on the recovery path chosen for the indent. If the indent recovers by the flat punch route [56] the input energy at any unloading load, P is

$$\begin{aligned} E_i(P) &= E_i(P_{max}) - \Delta E_i \\ &= E_i(P_{max}) - \frac{P_{max}^2 - P^2}{S} \end{aligned}$$

Where (from equation 1.14)

$$S = \left(\frac{16}{\pi}\frac{G^2}{H(1-\nu)^2}P_{max}\right)^{\frac{1}{2}}$$

The corresponding core energy

$$E_c(P) = \frac{(1-2\nu)}{\pi^2}\frac{(2-\cot\alpha)P^2}{aG}$$

where a is the flat punch radius and equal to the indentation radius at P_{max} .

Substituting in equation 2.4

$$E_c(P) + E_H(P) = E_i(P_{max}) - \frac{P_{max}^2 - P^2}{S} \tag{2.10}$$

Solution of the equation gives the current strength of the blister field.

2.2.3 Elastic - Plastic Boundary

The stress field at the free surface ($\theta = \pi/2$) as proposed by Yoffe [111] may be written as

$$\sigma_{ij} = \frac{s_{ij}\, P}{r^2} + \frac{t_{ij}\, B}{r^3}$$

where s_{ij} and t_{ij} are functions of Poisson's ratio.

Now

$$P = \pi H a^2 = C_1 a^2$$

From equation 2.9

$$B = C_2 P^{1.5} = C_2 \left(\pi H a^2\right)^{1.5} = C_3 a^3$$

where C_1, C_2 and C_3 are material constants. Substituting the stress becomes

$$\sigma_{ij} = \frac{s_{ij}\, C_1 a^2}{r^2} + \frac{t_{ij}\, C_3 a^3}{r^3}$$

At the elastic plastic boundary r = c.

$$\sigma_{ij} = s_{ij}\, C_1 \frac{1}{(c/a)^2} + t_{ij}\, C_3 \frac{1}{(c/a)^3} \tag{2.11}$$

and

$$\sigma_0^2 = J_2' \tag{2.12}$$

c/a may be estimated by substitutions of equation 2.11 into equation 2.12.

As s_{ij}, t_{ij}, C_1 and C_4 are material constants the estimated c/a is independent of the normal load. A superposed, combination of the Boussinesq and blister field, thus gives rise to a self similar process. It must be noted that this stress field implies that c/a will vary with θ. However, the stress field also implies that c/a at a given θ does not change with load.

2.3 Experimental Details

5 cm diameter and 2.2 cm length extruded copper (99.9% pure) blocks and sintered alumina flats of $2.54 \times 2.54 \times 0.63$ cm were indented with 150^o and 90^o (indenter angle) diamond tip cones. The cone was ground to a tip radius of 70 μm. The surface which was indented was ground and polished (1000 grit alumina powder).

The block was placed on a (5 KN maximum) load cell (figure 2.1). The movement of the indenter was recorded using a Linear Variable Displacement Transducer (LVDT). The whole assembly was placed inside and the indenter rigidly attached to the top plate of a precision subpress which was driven hydraulically in a universal testing machine.

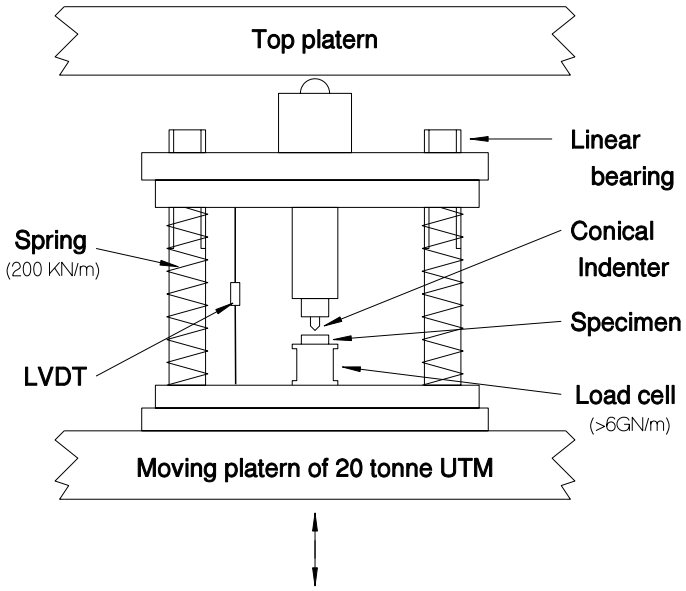

Figure 2.1: Experimental Setup

1 mm strain gauges were pasted on to the indented surface at fixed intervals from the indenter axis to record the radial strains. A single indentation experiment consisted of taking the load up to a certain value and unloading to zero load. Repeated loading and unloading cycles were implemented on the same indent, with the maximum load in any cycle being higher than that in the previous cycle and lower than that in the subsequent cycle. The output from the load cell, LVDT and the strain gauges were recorded to give the

displacement h and the surface strain $(\epsilon^e_{rr})_s$, at the load P during the loading and unloading cycle. Each experiment was repeated three times. The standard deviation of experimental results was found to be within 5 % of the average.

2.4 Results and Discussion

Figures 2.2 and 2.3 show the displacement-load graphs obtained by indenting the copper and alumina blocks respectively. It is of interest to note the uneven nature of the displacement-load graph for alumina when the indenter angle is 90^o. At point A (figure 2.3) the specimen develops a crack which facilitates large displacements at that point. Similar features are noted in the unloading part (point B) of the graph. Figure 2.4 shows large shallow craters and radial cracks in alumina specimen indented by a 90^o indenter. It is to be noted that similar features of the displacement-load graph were not observed when the indenter angle was 150^o . Figures 2.5 and 2.6 show the variation of the surface radial strain $(\epsilon^e_{rr})_s$ at r=4 mm as a function of cyclic loading (and unloading). The surface strains at very low loads ($< \ 200\ N$) or at points very close to the indent were found to be low ($< \ 2 \sim 3 \times 10^{-6}$) and tensile. At higher loads and further away from the indent the surface radial strains are compressive on loading and become more compressive on unloading.

The hardness of the test materials was estimated by measuring the projected area A, of the residual impression as $H = P_{max}/A$. The estimated hardness (1 GPa) of copper agrees with the BHN hardness of the test block ($0.8 \sim 0.9\ GPa$). The estimated hardness of alumina is 6.5 GPa. (Vicker's hardness testing at loads more than 2 kg was not possible as indentation produced cracks). The Young's modulus of both the test materials were estimated by measuring the initial slope of the unloading part of the displacement-load graph and substituting it into the equation [56],

$$G = \frac{P(1-\nu)}{4ah_e}$$

The estimated values are $G_{copper} = 45.1\ GPa$ and $G_{alumina} = 100\ GPa$. The poisson's ratio values were taken from literature [60, 28]

Given the experimentally measured $(\epsilon^e_{rr})_s$ the experimental strength of the blister field was estimated using equation 2.3. Figures 2.7 and 2.8 show this experimental B (B_{exp}) for copper and alumina respectively. Substitution of material constants in equations 2.9 and 2.10 gives the estimate of B, B_{th}. This estimates are plotted as continuous lines in the figures 2.7 and 2.8.

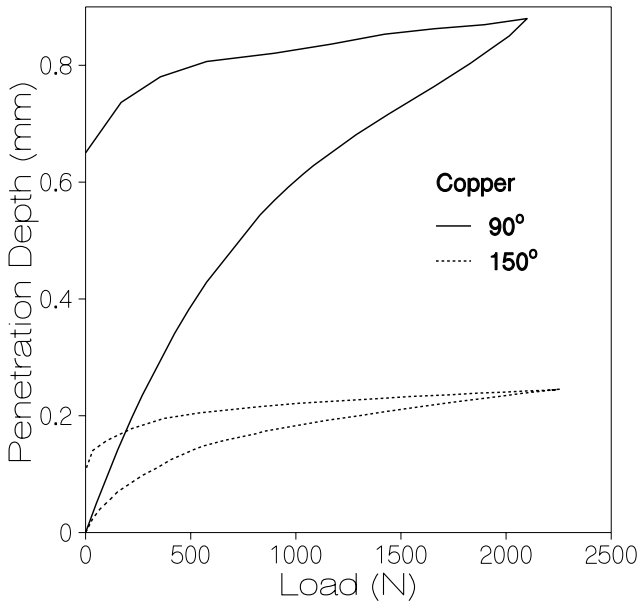

Figure 2.2: Displacement - Load Characteristics of Copper

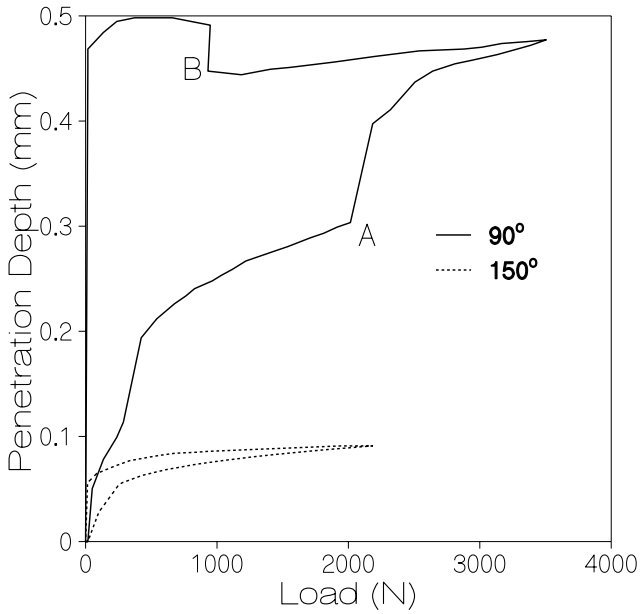

Figure 2.3: Displacement - Load Characteristics of Alumina

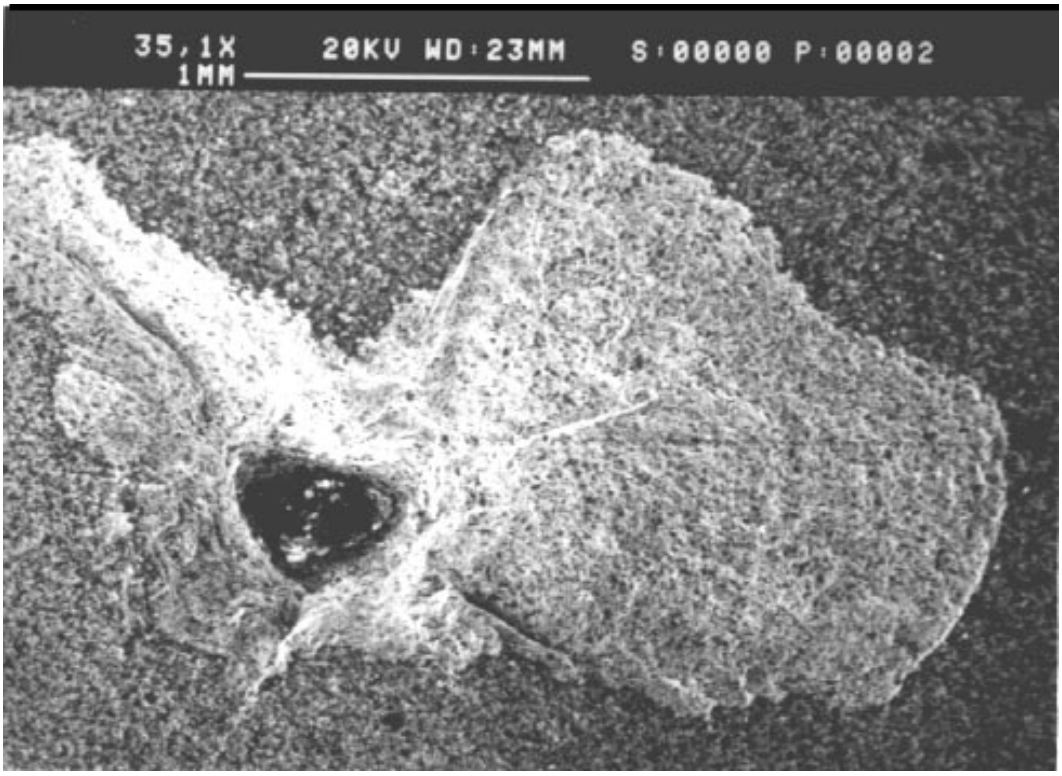

Figure 2.4: Scanning electron micrograph of an indent made on alumina by a 90^o cone

The departure of the estimate from experimental observation during unloading is probably related to the strength of the "recovery path" assumption. For example if the actual value of input energy at $P = 0$ is estimated by taking into account the actual non-linear experimental path during unloading and substituted in equation 2.10, then the B value is close to the experimental value (shown as a filled circle in Figure 2.7).

Figure 2.9 shows a radial surface profile of a pile up generated by 150^o indentation of copper. The profile is seen to deviate from the flat surface of the block at $t/a = 2.5$. The slip line field solutions of wedge indentation [26] limits plastic deformation in the deformation plane to a circle, the radius of which is equal to the distance of the pile up edge from the indentation axis. If the edge of a pile up is similarly said to be the limiting radius of plastic deformation in conical indentation, figure 2.9 which shows the pile up to be limited to $t/a = 2.5$, provides an experimental estimate of c/a. Table 2.2 shows that the present estimates of c/a are reasonable ones.

Figure 2.10 gives a comparative summary of the estimates of strength of the blister field during loading. As the alumina block started to fracture at low loads when indented by

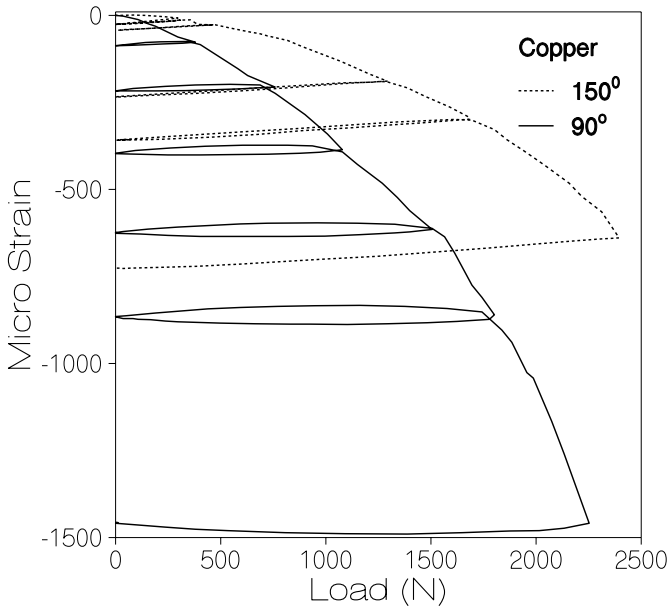

Figure 2.5: Surface radial strain at r=4mm from the indent axis for copper

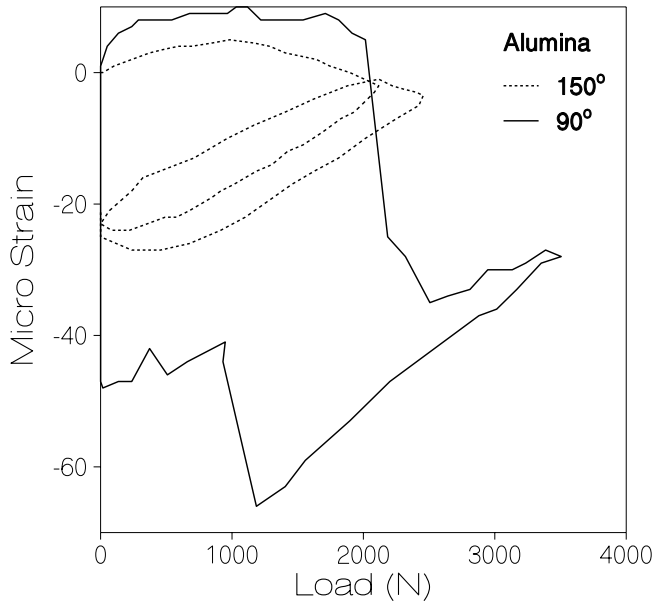

Figure 2.6: Surface radial strain at r=4mm from the indent axis for alumina

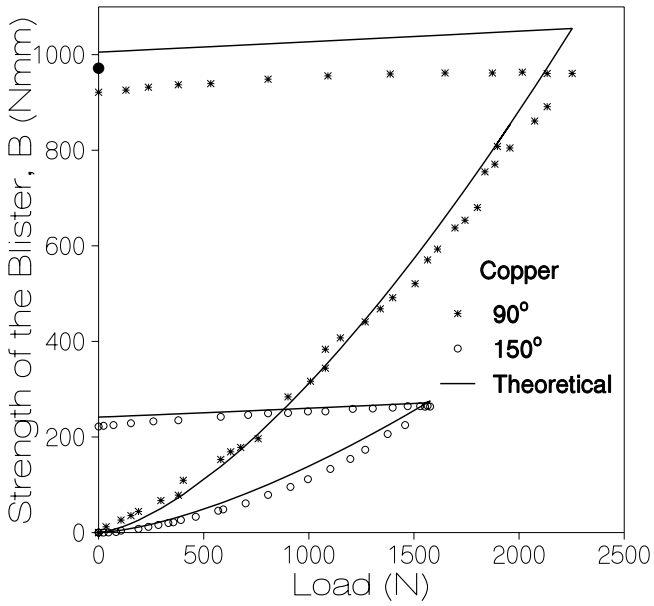

Figure 2.7: Variation of Blister field strength of copper with load

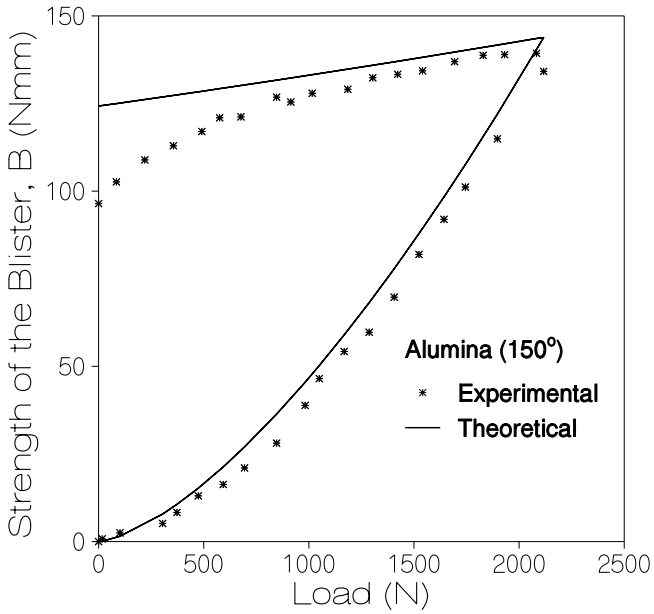

Figure 2.8: Variation of Blister field strength of alumina with load

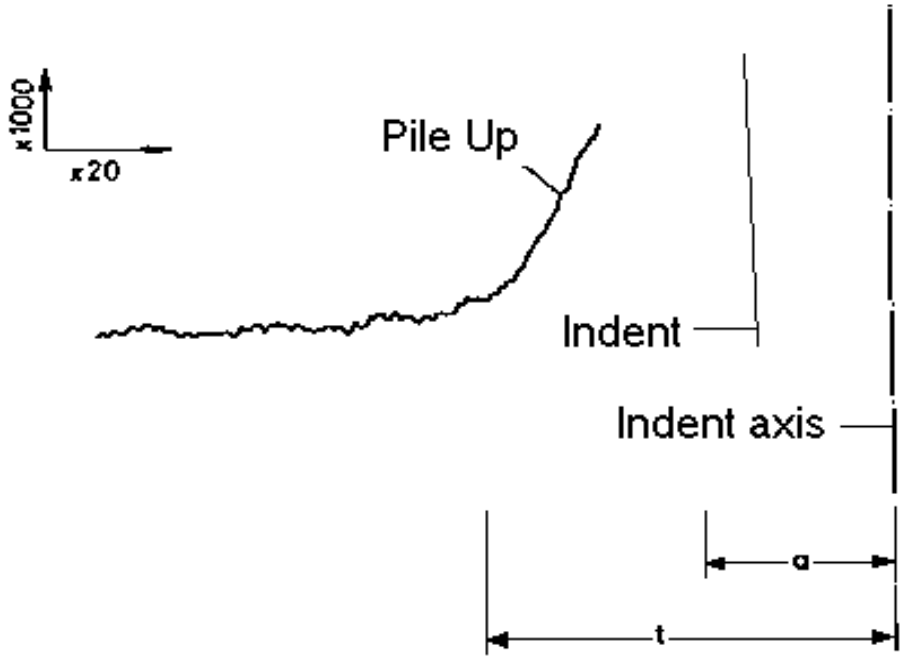

Figure 2.9: Radial surface profile of a pile up generated by 150^o indentation of copper

a 90^o cone, the corresponding estimates of the strength of the blister field from experimental surface strain measurements are considered to be unreliable and are therefore not shown in figure 2.10.

It is interesting to note that although the strength of the blister field of alumina indented by a 150^o cone is lower than when it is indented by a 90^o cone, the latter promotes fracture while the former does not. This trend is well predicted by the proposed stress field. Figure 2.11 shows the estimates of stresses generated by indentation of alumina (see equation 2.1) during loading. $\sigma_{\phi\phi}$ at $\theta = \pi/2$ increases due to a decrease in cone angle from 150^o to 90^o. This would encourage radial cracks on the free surface. Below the indenter ($\theta = 0$) the tensile σ_{rr} being much higher for the 90^o indentation than for the 150^o indentation the former is likely to give rise to lateral cracks. Figure 2.11 also suggests that no ring and median cracks are produced during loading.

The possibility of shallow lateral cracks (figure 2.4) can be demonstrated by transforming the polar stresses to cartesian stresses. Figure 2.12 shows that at a (x, z) coordinate of (a,a) the tensile σ_z is higher for the 90^o indentation of alumina than for the 150^o indentation.

Yoffe [111] has noted the possibility of lateral cracking below the indenter and radial

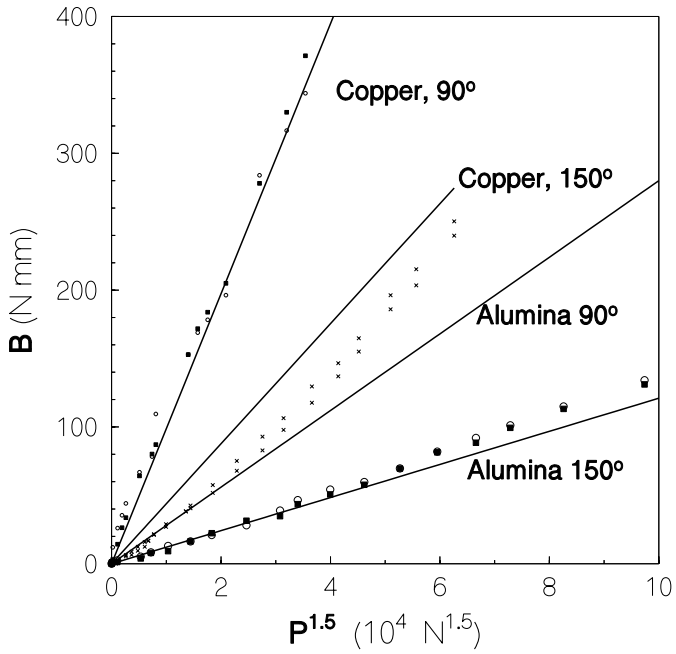

Figure 2.10: Comparative summary of the blister-field strength generated by conical indentation of copper and alumina

c/a	Copper, 150^o	Copper, 90^o	Alumina, 150^o	Alumina, 90^o
Johnson's [46] estimate	2.93	4.53	1.66	2.42
Present estimate	2.79	3.65	1.62	2.08
Experimental (from pileup)	2.5	3.4		

Table 2.2: Estimates of c/a

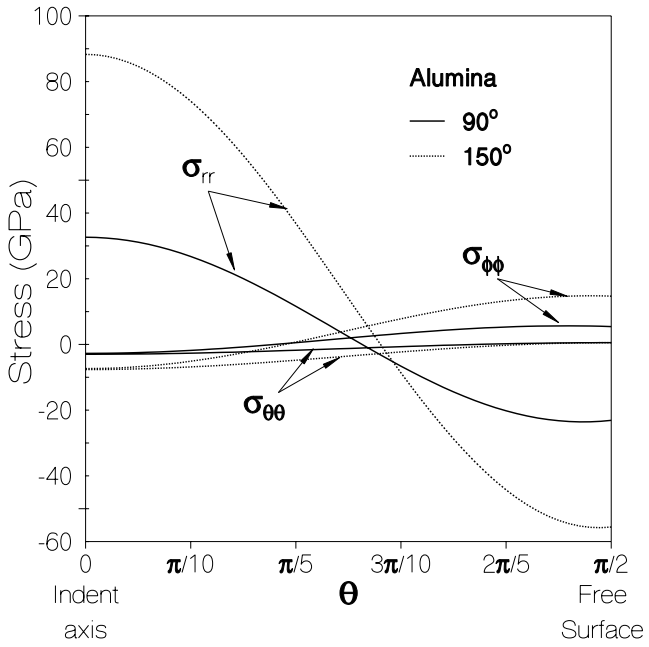

Figure 2.11: Estimates of stresses generated by indentation of alumina

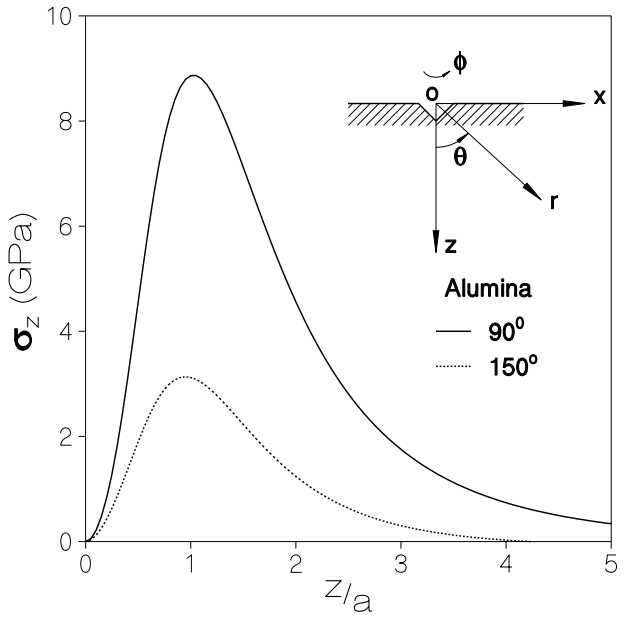

Figure 2.12: Estimate of σ_z generated by indentation of alumina at $x = a$

cracks on the surface propagating during the unloading part of the indentation cycle. Present calculations show that for alumina indented by a 90^o cone (the completely unloaded) residual tensile $\sigma_{\phi\phi}$ at $\theta = \pi/2$ as well as σ_{rr} at $\theta = 0$ are more than three times the value of these stresses at peak load. Thus the radial cracks seen in figure 2.4 may indeed have formed during unloading. The possibility of ring cracks being generated at the surface during unloading is however low as σ_{rr} at $\theta = \pi/2$ becomes zero on complete unloading.

A discussion of the comparative fracture proneness of copper and alumina cannot however be made using the present argument as copper has very high fracture toughness compared to alumina. The point however can be made that if it does fracture at very high load this may happen underneath the indenter in the lateral crack mode.

2.5 Conclusions

1. An identity which equates the input energy to the sum of the strain energy in the blister and that in the elastic hinterland can be used to predict strength of the blister field.

2. The strength of the blister field is a function of hardness, Young's modulus and poisson's ratio and is proportional to $(load)^{1.5}$ and the square root of the applied average strain $(0.2 \cot \alpha)$.

3. The strength of the blister field reduces owing to the reduction of strain energy in the core, during unloading.

Chapter 3

Displacement Controlled Nanoindenter

Nano-indentation is a technique to determine the local mechanical properties of the materials by indenting with a probe harder than the material. Though some instruments capable of measuring nanohardness [74] existed,the first instrument that recorded the load and displacement continuously was constructed by Pethica [81]. Since then a plethora of instruments has been designed. Table 3.1 gives a comparison of these designs. Most of these are depth sensing though some of them can do both depth sensing as well as imaging in same setup [58]. Some of these designs are now available commercially.

The nanoindenter can be either force controlled [73, 82, 108, 110] or displacement controlled [58, 96, 101]. In the force controlled instrument, a known amount of force is applied gradually and the resulting penetration is measured, whereas, in the latter type, the indenter is displaced gradually and the load required to do so is measured.

The main advantage of the displacement controlled instrument is that, it can be used to study the discontinuities (for example, see figure 2.3) in the load-displacement characteristics. In the case of ceramics, these discontinuities can arise out of propagation of cracks while in the case of metals, these discontinuities are found when the material response changes from elastic to plastic. In a load controlled instrument a small increment in load would produce a jump in displacement. Thus, the information on what happens inbetween is lost. It may be possible to record the exact variation in load across these discontinuities in a displacement controlled instrument.

The presence of so many designs brings out the fact that the instrument still remains to be perfected. The main problem is that it is very difficult to isolate the genuine material response from the errors introduced in measurement [65]. Numerical simulations [17, 114] have shown that purely statistical uncertainties in the measurement and the geometry of indenter and surface could give rise to the response similar to the actual response of the

Refer.	**Actuation**	**Displ. Sensor**	**Force Sensor**	**Guiding mechsm.**	**Coarse position.**	**Control, Config.**
Nishibori *et al.* 1978 [74]	d'Arsonval meter $10\mu N$	capacit. $\pm 10nm$		axle, jewelled bearing	hydraulic	load, vertical
Pethica 1982 [81]	electro-magnetic $2.5\mu N$	capacit. $2.5nm$		leaf springs	stepper motor	load, vertical
Newey *et al.* 1982 [73]	electro-static	capacit. $5nm$		jewelled bearing	piezo-electric	load, horz.
Wierenga *et al.* 1984 [108]	electro-magnetic $10\mu N$	inductive $5nm$		linear drv. air bear.	stepper motor $0.1\mu m$	load horz.
Bangert *et al.* 1986 [5]	electro-magnetic	SEM	cantilever, ϵ gauge $10\mu N$	cantilever		imaging vertical
Tsukamota *et al.* 1987 [101]	piezo-electric	fibre optic trans. $4nm$	electro-balance $0.1\mu N$		micro-meter	displ. vertical
Stone *et al.* 1988 [96]	piezo-electric	capacit. $2.5nm$ $100\mu N$	cantilever, capacit.		micro - meter	displ. vertical
Williams *et al.* 1988 [109]	linear translator	polarising interfero. $1.2nm$	parallel springs interfero.	parallel springs	stepper motor	displ. vertical
Jarvis *et al.* 1993 [44]	electro-magnetic	laser heterodyne interfero.	cantilever	cantilever	inertial slider, piezo.	load vertical
Lu *et al.* 1994 [58]	piezo-electric	optical $0.3nm$	cantilever		micro-meter	displ.
Woirgard *et al.* 1995 [110]	electro-static	capacit. $0.01nm$		silica springs	piezo. , meter	load vertical
Present Design	piezo-electric $11.5\mu m$	capacit. $0.67nm$	hinge capacit. $3\mu N$	flexure hinge	stepper motor $1\mu m$	displ. vertical

Table 3.1: Comparison of the existing Nanoindenter Designs

material.

A displacement controlled depth sensing indenter capable of indenting the materials with bulk hardness ranging from about 1 GPa to 10 GPa to a depth of 10 nm to 10,000 nm has been designed, fabricated and tested as a part of this work. A schematic of the complete system is shown in figure 3.1. It consists of a flexure capable of generating displacements upto 10 μm and a force sensor of resolution better than 3 μN. The flexure is mounted on a support structure that holds the specimen and the coarse positioning systems. The instrument is enclosed in a thermal chamber whose temperature could be controlled within $\pm 0.05^{o}C$ with the help of a laminar flow of argon gas. The vibration isolation table prevents the ground vibrations from affecting the measurement.

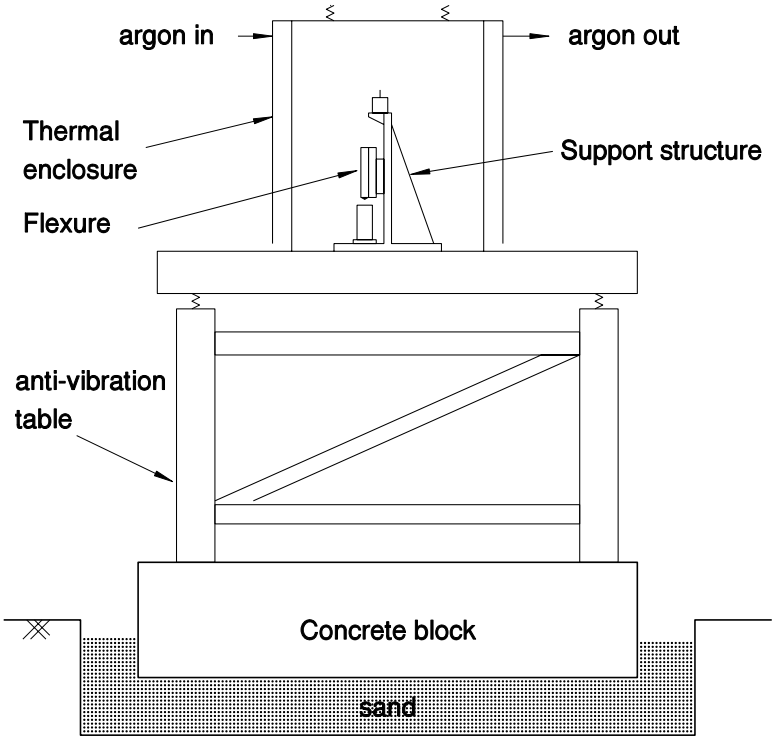

Figure 3.1: Schematic of the nanoindenter

Instead of trying to minimise the non-random measurement errors, the emphasis is given in characterising these errors and correcting them through the post-indent data analysis. The main innovation in this design is the force sensor which uses flexible hinges as the elastic element. The sensitivity of this sensor can be varied by suitably positioning the indenter and thus the performance can be optimised for a given test material. Present design

provides with two different sensitivity, one for metals and the other for hard materials like ceramics.

Design is a continuous and seemingly never ending process with a lot of nested feed back loops. In this chapter, it is not attempted to present the design process which involved a lot of feed backs from the studies on depth sensing indentation problems presented in this thesis and a lot of finer practical details from the experienced experts in different fields. Instead, what the final instrument is and how it works is presented.

3.1 Flexure Hinge as Force Sensor

Force is generally measured as the deflection of an elastic element in the range encountered in nano-indentation. Typically used elastic element is a cantilever beam for a range up to 100 N [86]. The deflection is measured as the strain. However the resolution of strain gauges are low and therefore not suitable for use in nano-indentation.

Instead of measuring strains, the deflection of the cantilever can be measured directly using tunneling current [13]. The resolution of such a sensor is very high (10^{-4} nN) and is being used in force microscopes [23]. The range of such sensors is however low and hence difficult to use in nano-indentation. The cantilever - a beam with a fixed end, can be replaced with a hinged beam with a spring. The main advantage of such a beam over cantilever is that the dimensions of the beam can be adjusted for resolution, lateral stability and natural frequency, independent of the stiffness of the spring. A flexure hinge can serve the purpose of the hinge and the spring simultaneously. The deflection of such hinged beam can be amplified using flexure-hinged levers [75]. If such a system can be used as a force sensor then its sensitivity can be increased without impairing the rigidity.

3.1.1 Design

Flexure hinge is basically a mechanical member which is compliant in bending about one axis but rigid about the cross axes. They are made from a blank having either a rectangular or circular cross section. The most common type incorporates a circular cutout on either side of the blank to form a necked down section. A closed form analysis of the stress distribution within such an hinge is rather complicated [55]. However a simplified expression for compliance can be obtained [12, 80].

A Finite Element analysis of such web is given by Smith *et. al.* [92]. This analysis

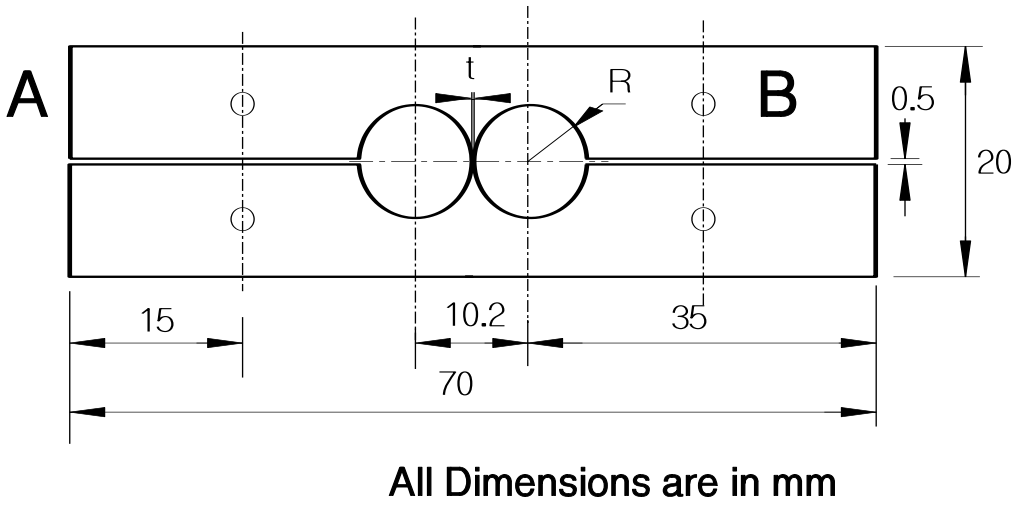

Figure 3.2: Flexure Hinge

gives the angle (θ) rotated by a particular hinge due to an applied bending moment (M) as

$$\theta = \frac{2KR}{EI_{zz}}M \tag{3.1}$$

where $I_{zz} = ht^3/12$, t is the thickness of the web, h is the depth of the web, R is the radius of the holes for the web and E is the modulus of elasticity. The value of K is obtained from the approximate formula

$$K = 0.565\frac{t}{R} + 0.166 \tag{3.2}$$

The maximum stress, which occurs at the outside edge of the thinnest part of the web can be determined from

$$\sigma_{max} = \frac{6MK_t}{t^2h} \tag{3.3}$$

The stress concentration factor K_t can be determined graphically [92] or from the approximation

$$K_t = \frac{2.7t + 5.4R}{8R + t} + 0.325 \tag{3.4}$$

The typical force resolution in nano-indentation is 3 μN and the range is 2 mN. The stiffness of the sensor should be high enough as not to cause any appreciable error in the measurement of the indenter displacement. These criteria along with equations 3.1 to 3.4 are used to find an optimum design solution. The web thickness t turned out to be very small (0.2 mm), for the material AU4G1. The properties of this material is given in table 3.2.

Si	0.5 % max
Fe	0.5 % max
Cu	3.8 $\sim$ 4.9 %
Mn	0.3 $\sim$ 0.9 %
Mg	1.2 $\sim$ 1.8 %
Cr	0.1 % max
Zn	0.25 % max
Ti + Zr	0.25 % max
others	$\leq$ 0.05 %

Young's modulus	72 GPa
Tensile strength	450 $\sim$ 480 MPa
0.2 % Proof Stress	290 $\sim$ 340 MPa
Elongation	9 $\sim$ 11%
Heat Treatment	T4 condition

Table 3.2: Chemical composition and mechanical properties of alloy AU4G1

The validity of the equations 3.1, 3.2, 3.3 and 3.4 for this thickness is established by actual measurement of a simple flexure.

3.1.2 Flexure Hinge Calibration

The flexure hinge was made out of a rectangular block of aluminium alloy AU4G1 (2024), heat treated to T4 condition. This material was selected because of its light weight and for its damping and hysterisis [25]. The flexure was cut out of the block by wire cut Electro-Discharge Machining.

Figure 3.2 shows a schematic outline of the sensor. A front polished mirror was attached on the side of the top block(A), with the help of a double side sticking tape. The deflection is measured by measuring the deviation of a reference laser beam reflected from the mirror in an autocollimator. The resolution of the autocollimator used was 1^o arc second. The force was applied through calibrated dead weights. The weights were added to a pan attached to the hole B. The calibration was carried out in a clean room isolated from vibrations.

The flexure calibration data, the angular deflection against the applied load is shown in figure 3.3. The stars are the measured data points. Different combination of the dead weights giving the same load gave slightly different deflections. The solid line is the linear least square fit with the slope of -3.49 deg/N. The dotted line is from the equation 3.1 which gives a slope of -2.44 deg/N. The deviation may be due to two main reasons. The thickness of the web t proved difficult to measure in profile projector as well as in coordinate measuring machine. Any error in the t value used in the equation 3.1 is compounded by being raised to the third power. The other source of the error may be in the value of Young's modulus. The hand book value for Aluminium - 675 GPa was used. The value of E for thin cross section

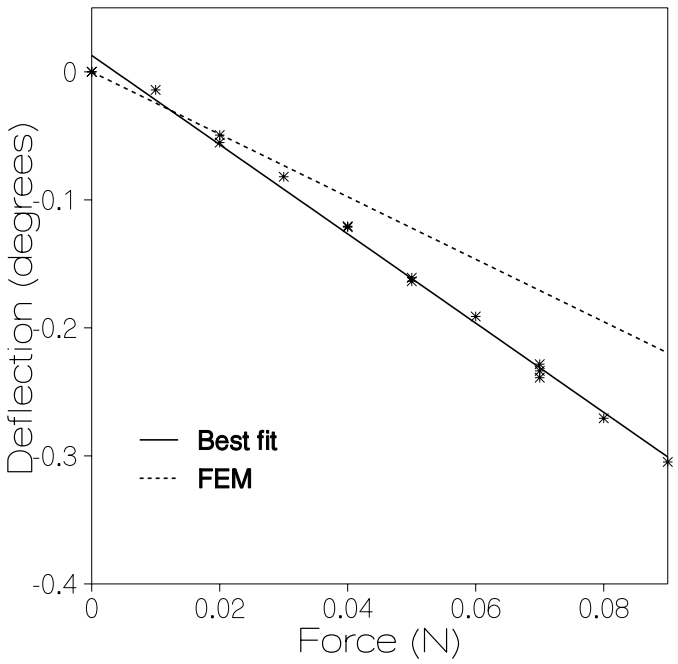

Figure 3.3: Calibration of the Flexure Hinge

might be different from the bulk value (see for example [89]).

3.2 Description

Figure 3.4 shows the mechanical details of the indentation instrument built. It uses a piezoelectric translator which has a range of 15 μm to generate the motion required by the indenter to penetrate the material surface. The actual displacement is measured with the help of capacitor sensor. The force is estimated as the deflection of a spring which is measured using capacitance sensors. The spring element used is the flexure hinges thinned out of the same block of material.

3.2.1 Translator

The piezoelectric translator (figure 3.5) is made out of stacks of piezoelectric elements that expand when voltage is applied across them. The elements are glued end to end such that the expansion of every element is added up to get a higher range of translation, without

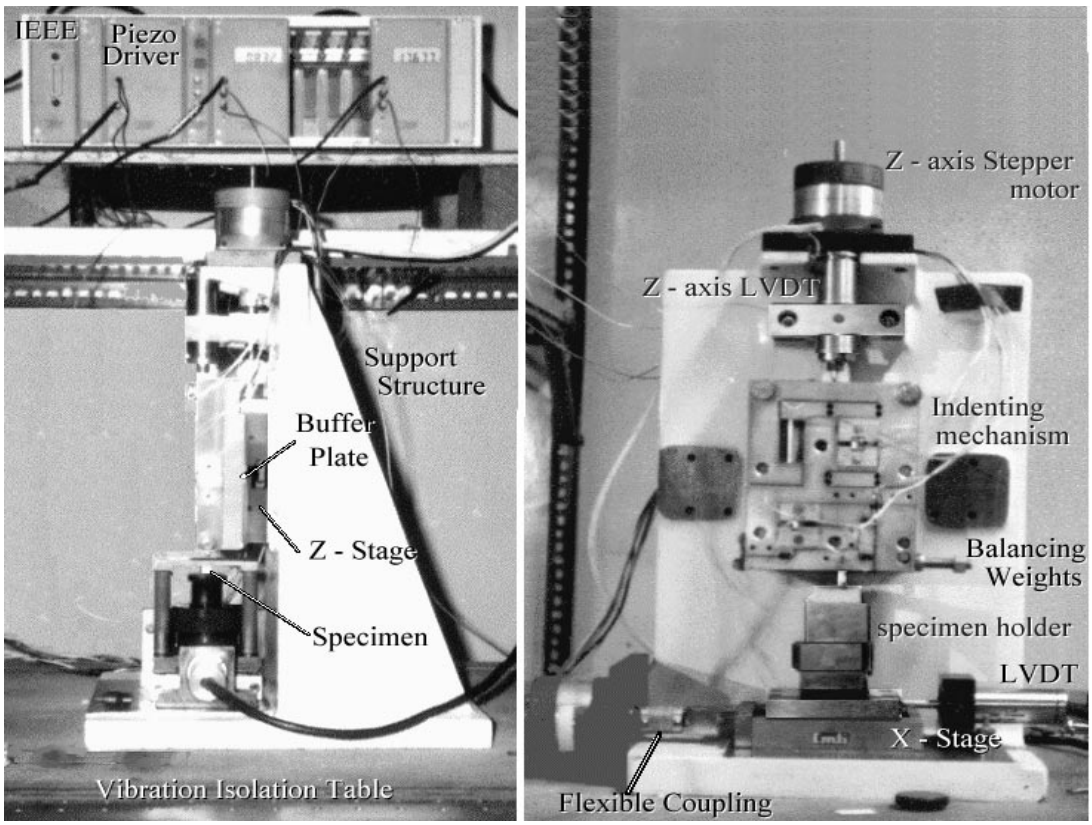

Figure 3.4: Instrument Details

going in for very high voltages. The voltage required to produce 15 μm of translation is 175 volts.

As the piezoelectric elements are made of brittle ceramic, it can take up compressive load, but very little tensile load. One end of the translator is fixed while the other end just rests against the support (figure 3.12) to ensure that the translator is never subjected to any tensile load.

The range of the piezo gets altered by the presence of an external compressive load. If the external load is going to vary with the expansion, then the linearity between the applied voltage and the translator motion is affected. To overcome this, the translator is made to move against an external spring whose stiffness is selected such that the load from

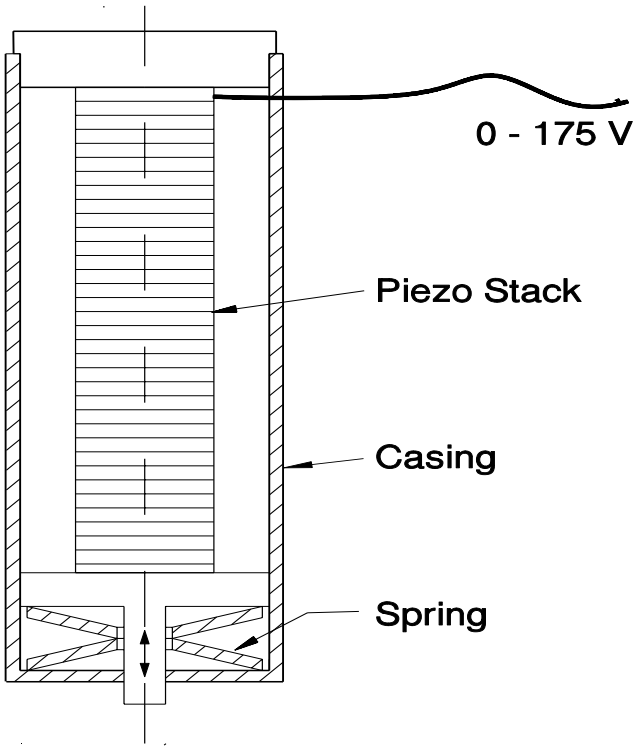

Figure 3.5: Schematic of the Piezo Translator

the indenter is a very small fraction of the total load on the translator. The presence of the external spring reduces the range of the translator. The effective range for the given setup is found to be equal to 11.5 μm.

There are two ways by which the piezo can be controlled. One is applying an external analogue voltage in the range of ± 5 V and the other is by sending digital signal from a computer, with the hexadecimal number 3FFF corresponding to the full range (i.e. the total number of steps is 16382) The advantage with the analogue input is that it is continuous unlike the stepped digital input, while the digital has an advantage that any arbitrary wave form could be generated using a simple software.

The response of the translator without any external load is shown in figure 3.6 whereas the response with the external spring load is given in figure 3.7. The hysteresis and other nonlinearity in motion can be eliminated by controlling the translator in a closed loop with a displacement transducer. An open loop control can however achieve a high speed.

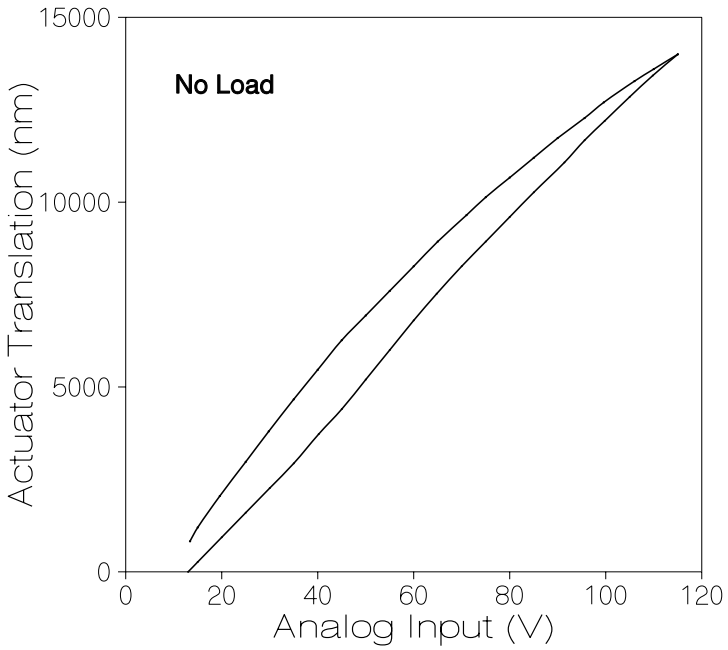

Figure 3.6: Response of the piezo translator

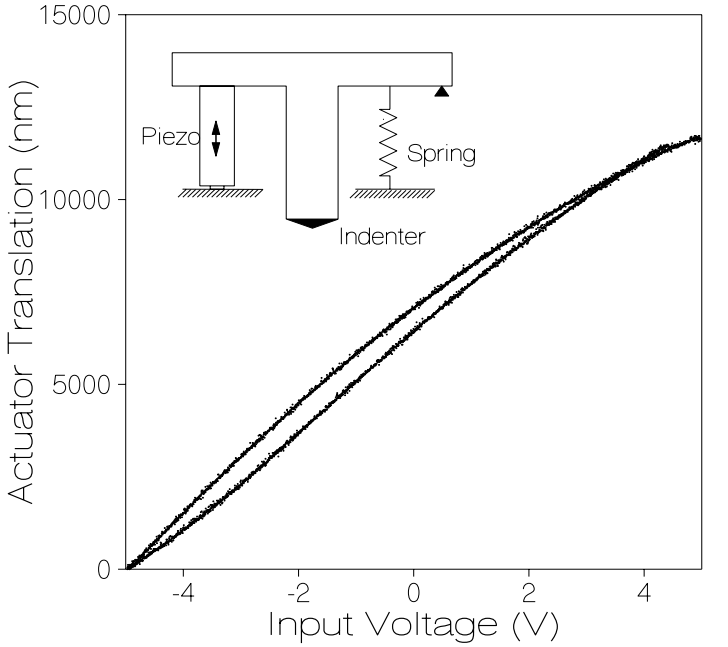

Figure 3.7: Response of the piezo translator in operating condition

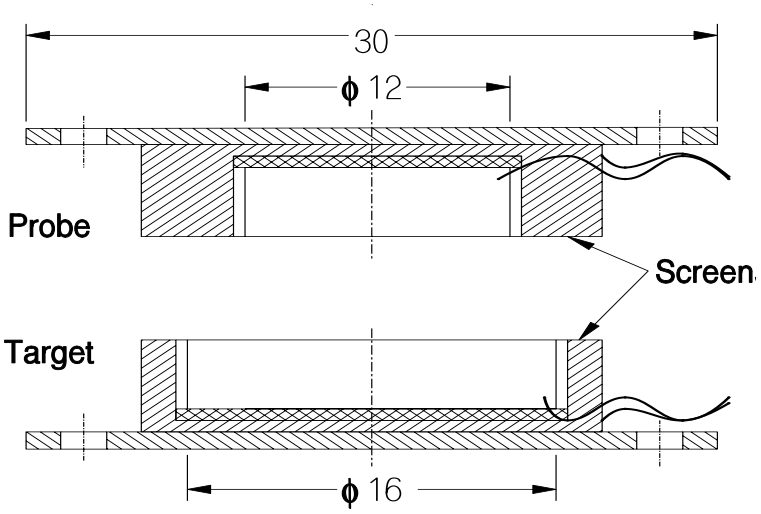

Figure 3.8: Schematic of Displacement Sensors

3.2.2 Displacement Sensors

Two capacitance type displacement sensors with a range of $\pm 20\ \mu m$ are used, one to measure the penetration of the indenter and the other to measure the force (figures 3.11 and 3.12). The capacitance sensors operate on the basic principle that the capacitance between two parallel plates is inversely proportional to the displacement. An electronic invertor is used to make the output voltage proportional to the displacement.

The sensor consists of two plates - one target and another probe held parallel to the target (figure 3.8). To take care of the end capacitance, grounded shields are used surrounding the plates. The capacitance is measured using a bridge circuit and the output of the bridge is passed through an invertor. The diameter of the probe is made smaller to the target diameter, to eliminate the error arising out of the lateral alignment. The parallelism between the plates is ensured by the four bar mechanism of the flexure which is machined to high precision in a single setting.

3.2.3 Force Sensor

A four bar mechanism with flexure hinges (section 3.1) is used for measuring the force. The flexure hinges acts as the torsional springs that deflect in proportion with the force. The magnified deflection is measured using a capacitance sensor.

The two conflicting requirements of the force sensors are the sensitivity and the stiffness. For a higher sensitivity, the deflection for a given force should be maximum, which

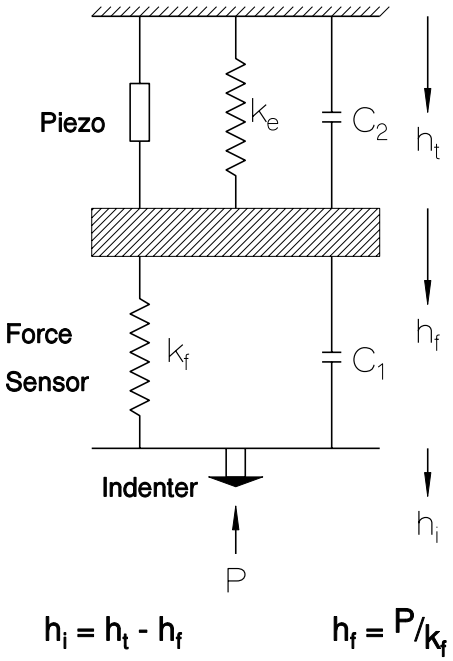

Figure 3.9: Schematic of Force Sensor in relation to the Translator and the Indenter

means that the stiffness should be very small. Lower stiffness means that the displacement (h_t) to be generated by the translator for a given penetration (h_i) is very high and the error in penetration measurement would be directly proportional to twice the deflection of the force sensor.

Figure 3.9 represents a schematic of the force sensor in relation to the translator and the indenter. If the force sensor of stiffness k_f deflects by h_f to measure a force P required to penetrate the indenter by h_i then the displacement of the translator is

$$h_t \;=\; h_i \;+\; h_f$$

If the percentage error in measurement of h_t is e then the maximum percentage error in measurement of h_i is

$$\begin{aligned}
\frac{\triangle h_i}{h_i} &= \frac{\frac{h_t}{100} e \;+ \frac{h_f}{100}\, e}{h_i} \;\times\; 100 \\
&= (1 \;+\; 2\; h_f)\; e \\
&= \left(1 \;+\; \frac{2\; P}{k_f}\right)\; e
\end{aligned}$$

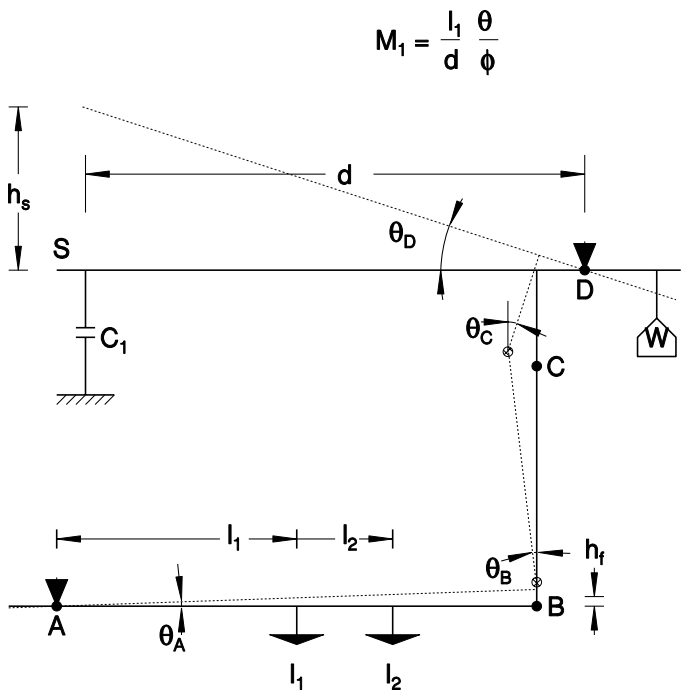

Figure 3.10: Schematic of the Force Sensor

Thus an higher deflection of the force sensor (h_f) of high sensitivity would introduce a large measurement error in the penetration.

The usage of the flexure hinges lets the deflection of the force sensor magnified, thus increasing the sensitivity without compromising on the stiffness. A system of two simple (figure 3.10) levers comprising the four bar mechanism (AB,BC,CD and the fixed frame DA) has been used. The four flexure hinges A,B,C and D are of same torsional stiffness, k_t. If the force on the indenter is P, causing a deflection h_f of the force sensor at the indenter tip I_1, then by equating the energy,

$$\frac{1}{2}\, k_f\, h_f^2 \;=\; \frac{1}{2}\, k_t\, (\theta_A^2 + \theta_B^2 + \theta_C^2 + \theta_D^2)$$

The effective stiffness of the force sensor is then

$$k_f \;=\; k_t \left(\frac{\theta_A + \theta_B + \theta_C + \theta_D}{h_f^2} \right)$$

The torsional stiffness, $k_t = \frac{M}{\theta}$ is determined by the geometry of the hinge, (equation 3.1) while the ratio in the bracketed term in equation is determined by the geometry of the four

bar mechanism. The deflection at I is magnified at S by

$$M_1 = \frac{h_s}{h_f} = \frac{DS}{DC}\,\frac{AB}{AI}$$

Thus, the required stiffness and the sensitivity could be obtained by suitably designing the geometry of the force sensor.

There is a slight lateral movement of the indenter due to rotational movements of the lever AB. However, the magnitude of this motion is small compared to the penetration of the indenter. For example, while indenting a material with a hardness of 1 GPa, for 10 nm, the lateral deflection is calculated to be less than 3 nm.

3.2.4 Flexure

This is the basic frame which integrates the translator, sensors and the guiding mechanism. Figure 3.11 shows the photograph of the flexure while a schematic of the same is shown in figure 3.12. To minimise friction and power losses and the associated heat generation, all the joints are made out of flexible hinges. The monoblock construction helps to eliminate the residual stress resulting from the temperature change in the surroundings if the flexure was made out of assembled of different materials. This also reduces the thermal drift.

The flexure is fabricated out of aluminium alloy AU4G1, the complete specification of which is given in table 3.2. This material has a highly linear stress-strain curve in the elastic region. The added advantage of this material over the other force transducer material like Cu-Be alloy is the density. The light weight of AU4G1 alloy allows greater freedom in designing the geometry of the critical flexible hinges in the force sensor.

The material in rod form was cold forged and then heat treated to T4 condition. The initial machining - milling and grinding produces surfaces that are parallel within 0.01mm. The reference holes were drilled in jig boring machine with a positional accuracy of $\pm 5\ \mu m$. The holes for the indenter I_1 and I_2 were machined by spark erosion to maintain the parallelism of the indenter axis with the guiding mechanism.

All the flexible hinges were machined in a single setting using wire cut electro discharge machining. The relative positional accuracies were maintained to an accuracy better than $\pm 5\ \mu m$. The optimum machining parameters like the current, feed rate and wire thickness were obtained after detailed experimentation. The problem of residual and clamping stresses distorting the geometry after the machining was overcome with the help of a fixture. Restraining braces were used at the points where slots opened out while machining. The

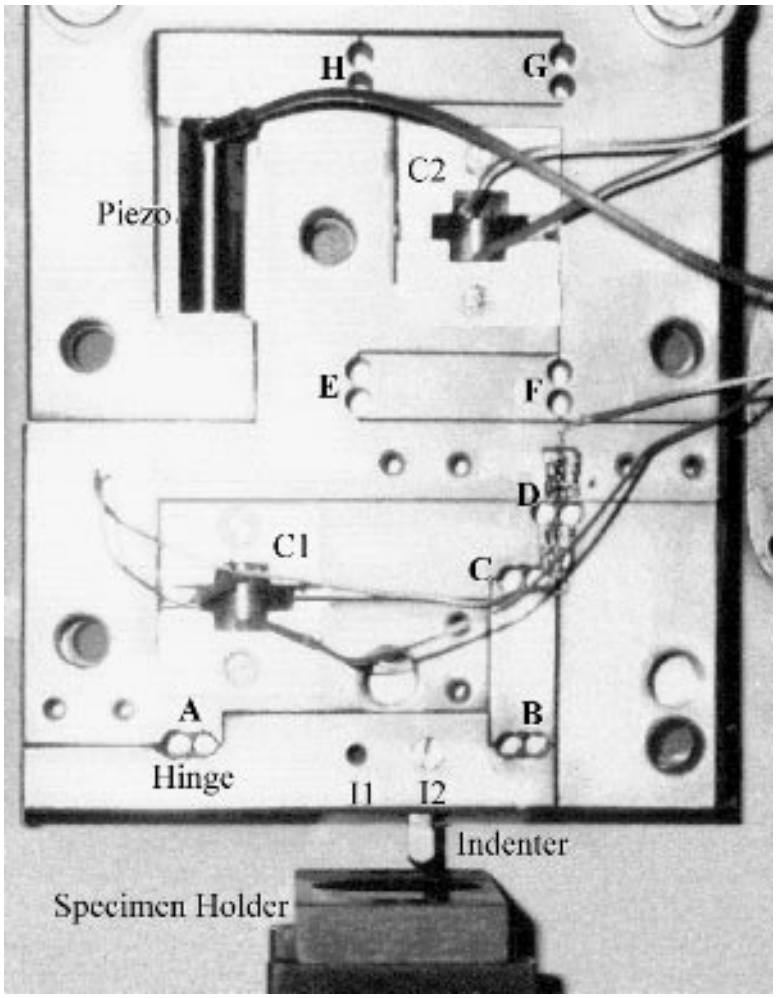

Figure 3.11: Flexure

thickness of the hinges A, B, C and D that form the force sensor is thinned out to 3mm using spark erosion.

The flexure is made out of 8 flexible hinges ($A - H$ in figure 3.12) that form two four bar links. The links AB, BC ,CD and DA is the force sensor (section 3.2.3) and the links EF, FG, GH and HE form the guiding mechanism. The guiding mechanism generates the straight line motion for the indenter.

The piezo electric translator is attached to the link GH and moves against the fixed link FG. This arrangement produces a linear motion of link HE to which the force sensor is attached and ensures that the load on the translator is always compressive. The actual motion of the link HE is measured with the help of the capacitance sensor C_2 attached to links FG and EH.

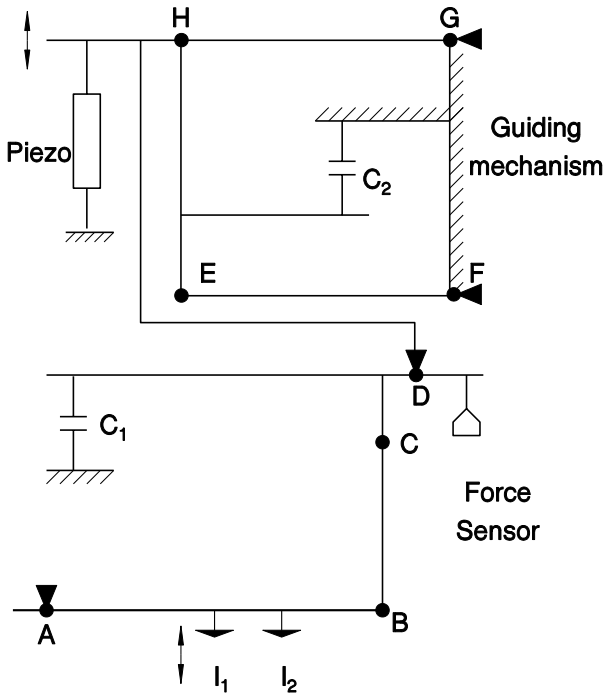

Figure 3.12: Schematic of the Flexure

The capacitance sensor C_1 attached to the links CD and DA, it measures the magnified deflection of the force sensor. There are two positions on link AB at which the indenter can be fixed, I_1 and I_2. I_1 gives higher stiffness and relatively lower resolution to I_2 and can be used to indent hard materials like ceramics.

3.2.5 Buffer Plate

This is a plate (figure 3.13) made out of same material as the flexure and is used to attach it to the Z stage of the coarse positioning system. Since the Z stage and the flexure is made of materials that have different thermal expansion co-efficient, buffer plate is used to take up the stresses induced due to any small variation in the temperature. The buffer plate has a sculptured relief that allows free motion of the force sensor.

3.2.6 Coarse Positioning

The range of the indenter motion is about 10 microns. To move the specimen surface within the range of the indenter, two coarse positioning stages X and Z are used. These stages

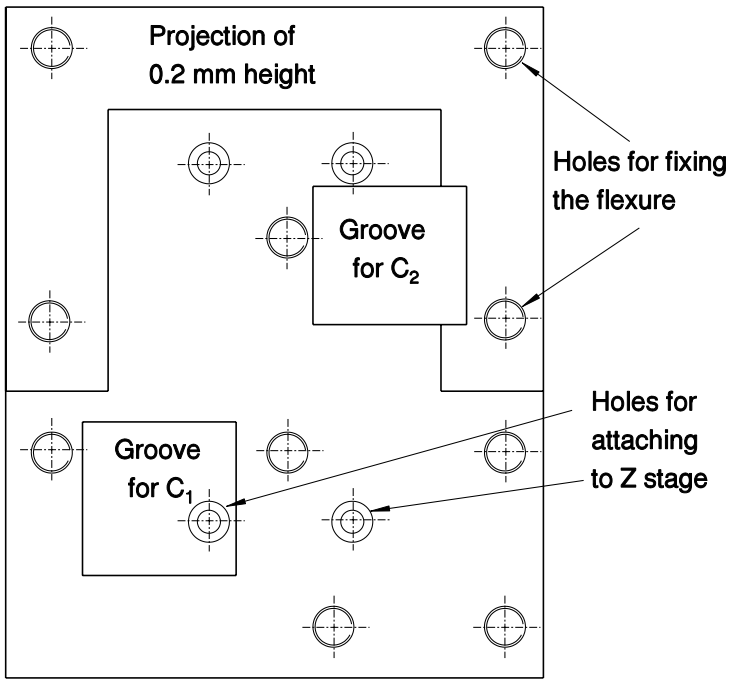

Figure 3.13: Buffer Plate

has a range of 15 mm and has a positional accuracy of better than 1 micron. The stage consists of a rectangular platform moving on a linear ball bearing and a 0.5 mm pitch lead screw. Stepper motors with 500 steps per revolution are used to drive the stages. Linear Variable Differential Transformers measure the actual linear motion of the stage and a closed loop control of the stepper motors eliminates the backlash problem associated with the lead screw. The closed loop control is implemented digitally with the help of a specially developed algorithm.

3.2.7 Specimen Holder

The surface of the specimen on which the indentation is to be carried out must be perpendicular to the axis of the indenter. This is ensured by the specimen holder (figure 3.14) that is mounted on the X stage. The specimen is held against a reference surface and the irregularities of the specimen is accommodated by clamping it with the swivelling plate. This arrangement helps to locate roughly the point at which the indenter will first come in contact with the surface.

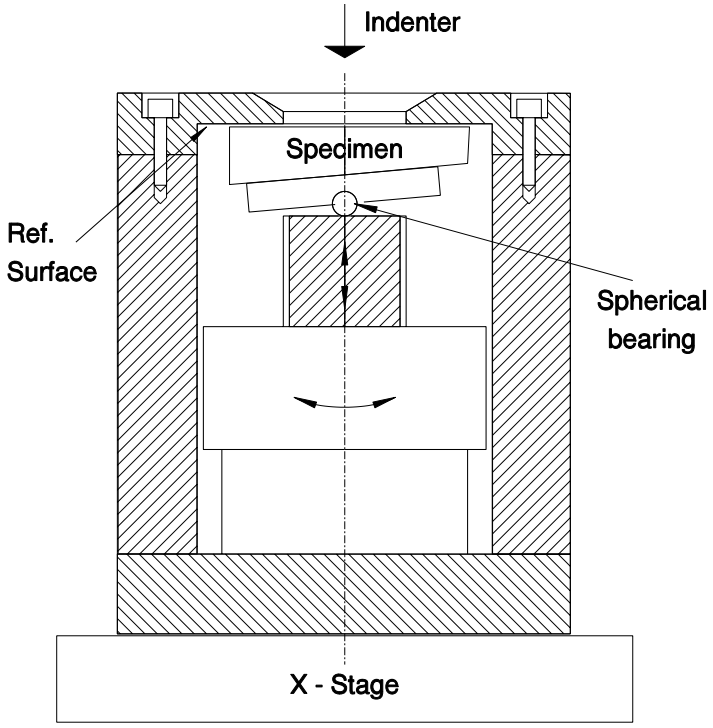

Figure 3.14: Specimen Holder

3.2.8 Support Structure

The inverted "T" shaped cast iron support structure holds the stages and the specimen holder such that the indenter is perpendicular to the surface of the specimen on which the indentation is to be carried out. This study structure with reinforcing webs, completes the force circuit between the indenter and the specimen. It is designed such that the deflection in the force circuit is less than 0.1% for the maximum load encountered while indenting a specimen with a hardness of 10 GPa. The surfaces holding the stages were hand scrapped to maintain the perpendicularity of the stages to less than 1micron.

3.2.9 Vibration Isolation

The instrument is protected from the mechanical vibrations transmitted through the ground with the help of a pneumatic controlled vibration isolation table. The table itself is placed on an isolated foundation. The foundation consists of $5' \times 5' \times 1.5'$ reinforced concrete block. The concrete block is isolated from the surrounding floor by a 6" trench filled with sand.

The vibration isolation table rests on 4 pistons that rests on a flexible rolling di-

aphragm. While operating, the piston floats under the pressure of the air contained in the cylinders. The natural frequency of the whole system is less than 2.5 Hz in both horizontal and vertical directions.

The vibrations due to the pressure waves transmitted through air and draft is minimised by enclosing the instrument in a persplex chamber. The chamber is supported on the ground such that the chamber is not in contact with the vibration isolation table top. This is to pass the vibrations picked up by the chamber to the ground and not to the low compliance table top.

3.2.10 Temperature Control

The instrument is enclosed in a chamber whose temperature could be maintained with an accuracy better than $\pm 0.05^oC$, by a controlled laminar flow of argon gas through the chamber. The chamber is designed such that the vibrations induced on the force sensor is minimal. Except for the experiments that are carried out over a large period time like indentation creep experiments, most of the indentations could be carried out over a period of time during which the change in the temperature from the equilibrium value is negligible. Thus the flow is switched off once the thermal equilibrium is reached. The temperature at different parts of the instrument could be measured with thermocouples and the data could be lodged into the computer.

3.2.11 Electronics and Computing

The complete experiment cycle is automated and the process is controlled through a pentium 100 MHz computer. A schematic of the electronics involved is shown in figure 3.15. A software that includes post-experiment data analysis is developed in Visual Basic. Most of the algorithms are very specific and has been developed from the scratch. The main emphasis is given to the flexibility in designing the experiment cycle to the user rather than fixing the variables to rigid preset values. At the same time some of the standard experiments, such as repeated indentations, creep, are provided as a package.

The piezo electric drive and the capacitance sensor output is communicated through an IEEE 488 interface. In case a higher data transfer rate is required, than that is provided with this interface, an option is provided to communicate through a data acquisition card but with a lower resolution. It is also possible to drive piezo continuously through an external signal generator. For example, it is possible to carry out constant strain rate experiment in

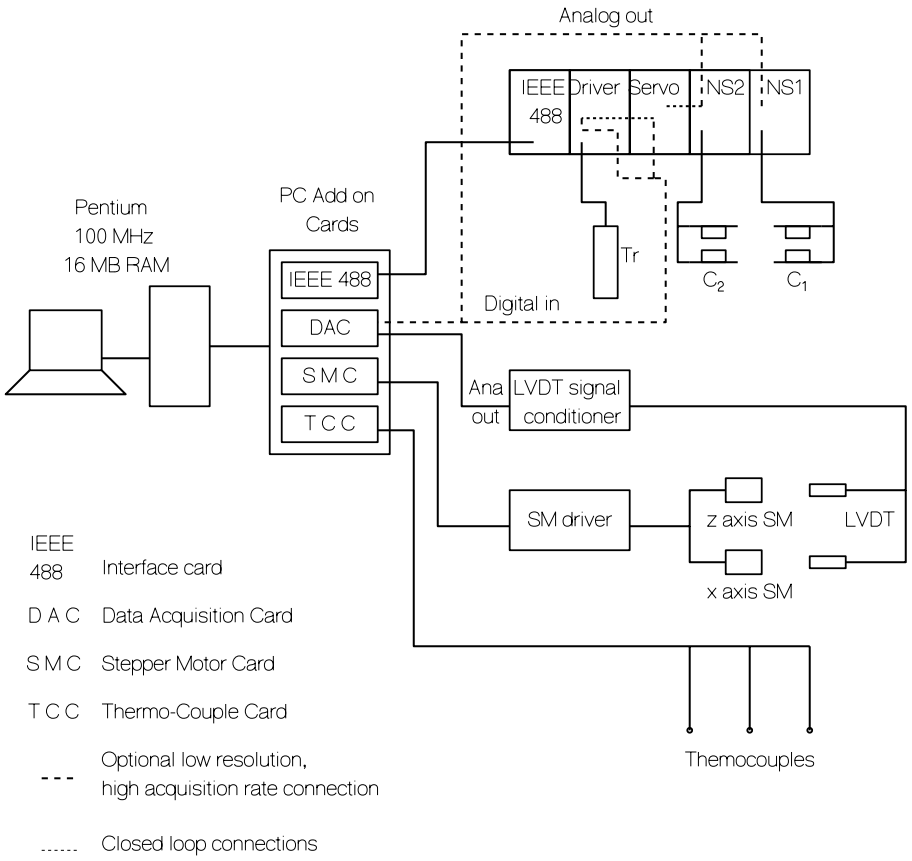

Figure 3.15: Schematic of the Electronics

which the stepped digital output would mean a momentary high strain rate.

The piezo electric translator can be driven in open loop or in a closed loop with the feed back from the capacitance sensor measuring the displacement. The open loop has an advantage of achieving a higher displacement rate of the indenter while the closed loop ensures a constant displacement rate, overcoming the inherent nonlinear responses of the piezo drive. The closed loop control is effected through an electronic hardware controller. By connecting the force sensor (C_1) output, to this controller instead of the displacement sensor (C_2) constant loading rate experiments could be carried out.

The stepper motor is driven through an add-on card. The resulting linear motion of the stages are measured using two linear variable differential transformers, through a signal conditioner and an Analog to Digital convertor card. The closed loop control is effected

through software algorithm.

3.3 Working Principle

3.3.1 Sequence of Operation

With the Z stage moved to the top limit, the specimen is butt against the reference surface of the holder. After ensuring the thermal equilibrium, the Z stage is moved such that the indenter tip is within 2 microns of the reference surface. The temperature at different points of the instrument are checked for the thermal equilibrium. The piezo-electric actuator is moved to establish the contact point ($V^{'}$) as explained in the section 3.3.3. The indentation is carried out by the controlled penetration of the indenter and the readings of the capacitance sensors C_1 and C_2 are acquired as the penetration and the force values. Once the indentation is completed, the Z stage is moved up by 20 microns. The X stage is then moved by the required distance such that the indentation could be carried out at different point on the specimen and the cycle repeats.

3.3.2 Data Processing

The acquired data will be in terms of the output voltage V_1 and V_2 from the two sensors C_1 and C_2 at different instances of time. The exact penetration is given by

$$h \;=\; \frac{V_2 \;-\; V_2'}{K_v} \;-\; \frac{V_1 \;-\; V_1'}{K_v\; M}$$

K_v is a constant that converts the voltage reading of V_1 and V_2 to the respective displacement values and is equal to 4000 nm/V. M is the magnification value for the force sensor which is 14 for indenter fixed at I_1 and 7 for indenter at I_2. The force P is

$$h \;=\; \frac{V_1 \;-\; V_1'}{K_v\; K_f}$$

V_1' is the reading of the force sensor at the contact point and K_f is the stiffness of the force sensor. The hardness and Young's modulus are determined from the resulting P *vs* h graph as explained in section 1.2.1, and 1.2.2.

3.3.3 Contact Point Determination

The first point at which the indenter comes in contact with the surface, serves as the reference for calculating the penetration depth. Any error in the determination of this contact

point will result in considerable error in the hardness measured at small penetrations as the projected area of sharp indenters goes as the square of penetration. The contact point can be found in two different ways.

1. Detecting it experimentally with the accuracy limited by the resolution of the measurements involved.

2. Post experiment analysis of data by fitting a curve to the loading portion of P vs h curve and extrapolating to zero load.

The second method is numerical and depends on some model to set the type of curve to be fit. Experimentally, since the indentation process is displacement controlled, the contact point is determined by measuring the variation in the force sensor output. As the indenter is moved towards the surface, the force sensor output varies due to the noise with the mean remaining constant. However, once the indenter comes in contact, the mean changes. This change is detected using a statistical testing procedure.

The population sample is taken when the indenter has been moved within 2 microns of the sample holder reference point by the Z state and the thermal equilibrium has been reached. The translator is then given a small increment in displacement, typically 1nm. In selecting this increment value, a compromise is made between the accuracy and the time taken. A sample of the force sensor output is taken, typically 25 values and the mean is compared with the population mean using Student's "t" distribution at 99% confidence level. If this statistical test result says that both the mean are same, then the displacement is increased by another increment. The procedure is repeated till the contact is established. The contact is further confirmed beyond doubt by repeating the test with two more increments. The whole process is carried out automatically through the PC.

3.4 Performance

A 16 bit analog to digital converter gives a displacement resolution of 0.672 nm for the capacitance sensors when data is acquired through the IEEE488 interface card, while the 12 bit PC add-on converter with an acquisition rate of 500 Hz gives a resolution of 9.76 nm. The minimum step size through which the piezo translator can be driven is 0.916 nm at the maximum rate of 18 Hz when controlled through the IEEE488 interface. Figures 3.16 and 3.17 shows the variation of the displacement and the force sensor output with time when the

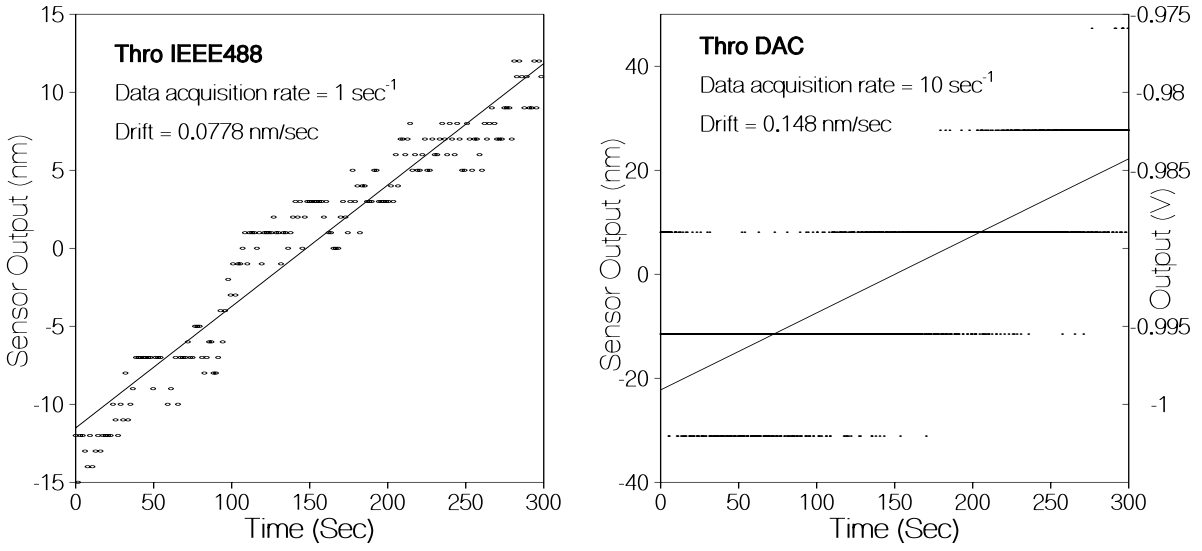

Figure 3.16: Displacement sensor output

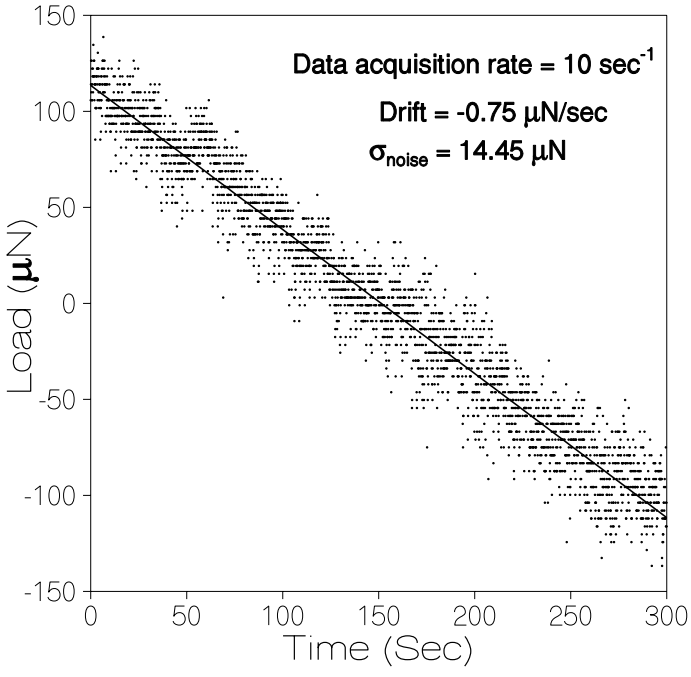

Figure 3.17: Force sensor output

instrument is in thermal equilibrium. It can be seen that the peak to peak noise is 4 nm for displacement sensor and 14 μN for the force sensor.

3.4.1 Stiffness of the Force Sensor

The effective stiffness of the force sensor is an important parameter that determines the accuracy of the force measured. The force is measured as the deflection of the spring system involving the four flexible hinges. Though the stiffness could be calculated theoretically through the FEM analysis, the actual stiffness would depend on the machining accuracy that determines the exact dimensions of the hinges and their relative positions. Hence, the actual stiffness of the force sensor is obtained by applying a known force at the indenter and measuring the output of the sensor C_1.

A permanent magnet is attached to the point I_1 and I_2 instead of the indenter and a coil of 180 turns of copper wire is placed in the specimen holder. Thus the force at indenter could be simulated by varying the current in the coil. If the magnetic moment is known exactly, the force can be obtained as a function of the current and the distance between the coil and magnet. The force is maximum when the tip of the magnet is just outside the coil.

Instead of depending on the theoretical expression for the force on magnet that involves other constants such as the geometry of coil, the magnetic moment of the magnet and the permitivity of the medium, the actual force vs current characteristics is measured in a precision opto-electronic balance. Figure 3.18 shows the schematic of the arrangement used. The magnet is attached to the weighing arm of the balance, while the coil is fixed such that the tip of the magnet is 10 μm from the edge of the coil as verified by a feeler gauge.

The compliance of the balance is very high, causing the distance between the coil and the magnet change a lot even for very small amount of the current, in the coil. Precision weights are placed on the pan and the current is adjusted such that the optical grating reading remains the same. This means that the gap between the coil and magnet remains constant. The force acting arm is equal to the total amount of precision weights and the force on the magnet. Thus by varying the weights on the pan, the current for different force on the magnet could be measured. The resulting force vs current graph is shown in figure 3.19. The slope (m_{if}) of the best fit line is 30.724 Amp/N.

To find the effective stiffness of the force sensor, the magnet is placed in the indenter's place (I_1 or I_2 in figure 3.11). The distance between the magnet and the coil is adjusted using Z axis stepper motor and a 10 μm feeler gauge. A known force now can be applied by passing a known current in the coil. Under this force the sensor deflects which is measured by

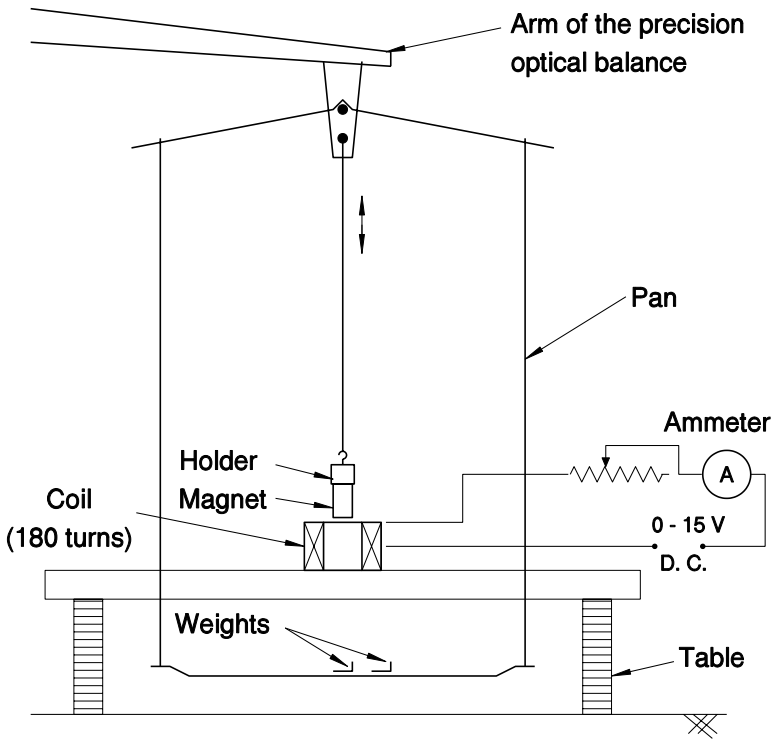

Figure 3.18: Arrangement for Calibrating the coil and the magnet

the capacitance sensor (C_1). A slight variation in the gap between the coil and the magnet could be adjusted with the help of the piezo-electric translator. However, it has been found that the variation in the force due to the slight change in the gap (of order of 10nm) is negligible. The current vs sensor deflection is plotted in figure 3.20. The slope (m_{di}) of the best fit line is -7273 nm/Amp. The sensitivity of the force sensor is thus

$$s_f \;=\; m_{di} \times m_{if} \;=\; 223.5\ nm/mN$$

Since the minimum displacement that can be measured using the capacitance sensor C_1 is 0.672 nm the smallest force that can be detected is 3 μN. The stiffness of the force sensor is

$$k_f \;=\; \frac{M_1}{s_f} \;\approx\; 62.64\ \mu N/nm$$

3.4.2 Indentations on Copper

Figure 3.21 shows a typical load vs displacement graph obtained by indenting work hardened copper specimen with a 120^o conical indenter. The SEM picture of the tip of the indenter is

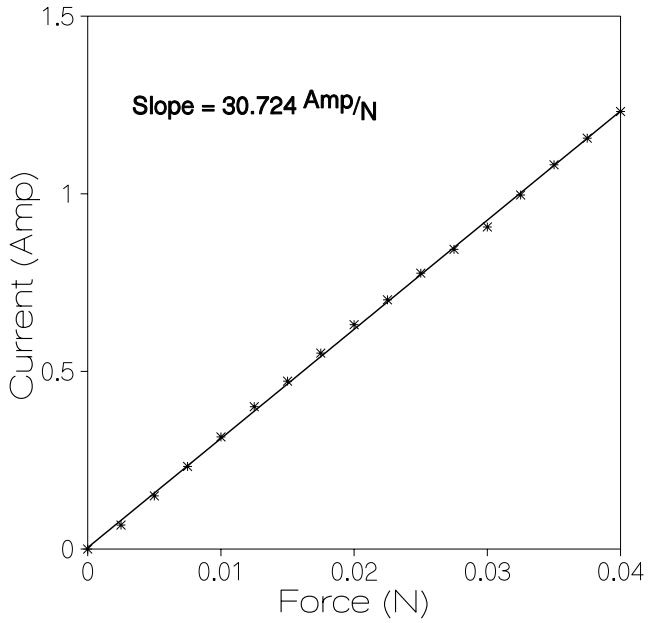

Figure 3.19: Calibration curve for the coil and the magnet

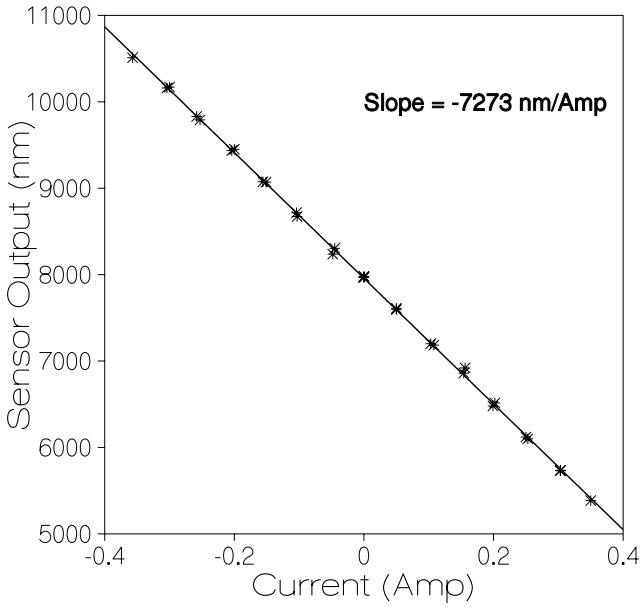

Figure 3.20: Calibration curve for force sensor

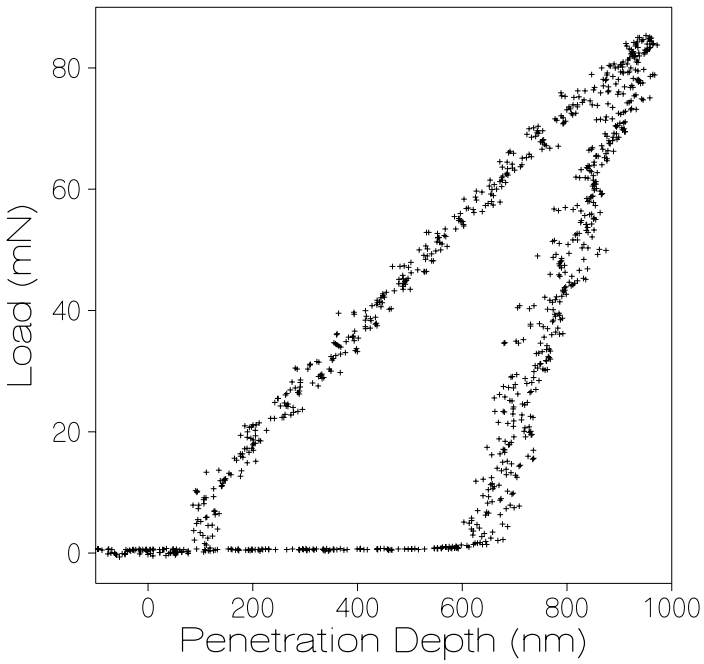

Figure 3.21: Typical Load–Displacement Curve

shown in figure 3.22. The area function of the indenter is obtained as

$$A = 79.23 \times 10^3 \times h + 46.82 \times h^2$$

where h is in nm and A is in nm^2, by measuring the area of the indents obtained for different penetration depths. Figure 3.23 shows two such indent for a penetration depth of 800 nm and 5000 nm.

Figure 3.24 shows the variation of hardness with penetration depth, for 5 different experiments. There is a definite increase in the measured hardness for penetration depths less than 1000 nm. The decrease in hardness for penetrations less than 200 nm is due to the fact that the indenter tip is blunt (figure 3.22) and the response is that of an elastic or elastic-plastic material. For example for a tip radius of 30 μm the first yield will occur at a load of 25 μN, assuming hertzian contact and bulk yield stress of 0.2 GPa. However for a surface hardness of 10 times the bulk the load will be 25 mN. The variation in hardness with penetration may also be due to a small error in determination of the area function or due to the effect of surface roughness. The surface of the specimen was mechanically polished with a diamond paste of average particle size of 2.5 μm. The R_z value was found to be 0.8 μm

Figure 3.22: SEM Image of the Indenter tip

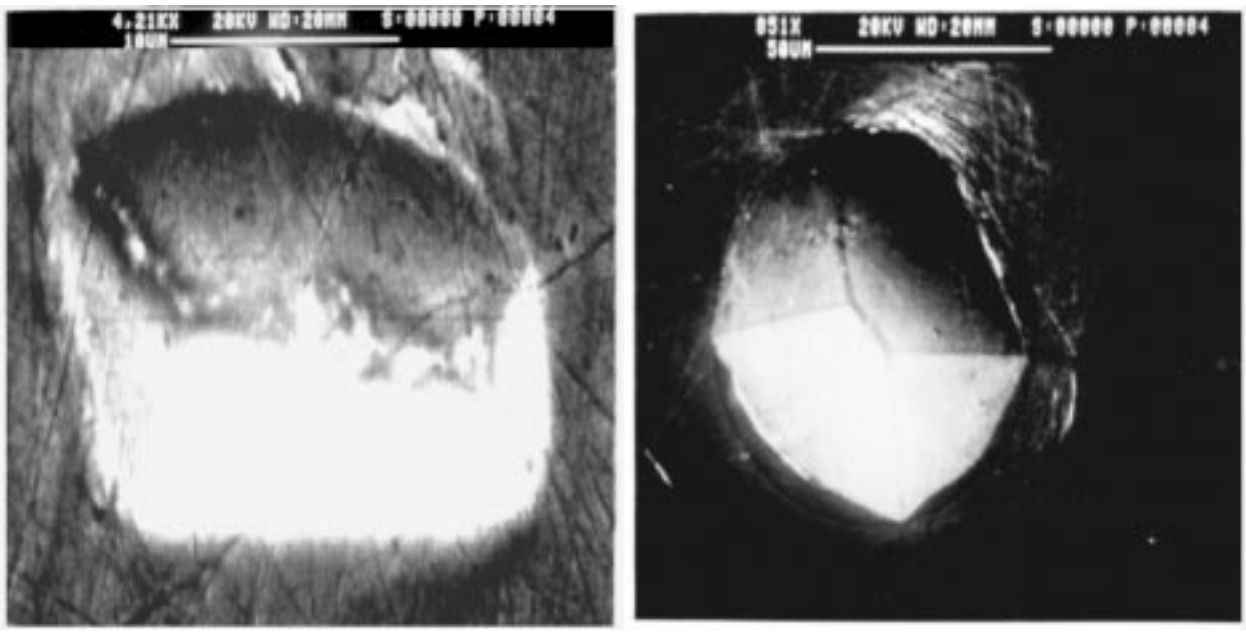

Figure 3.23: SEM Image of the Indents on Copper

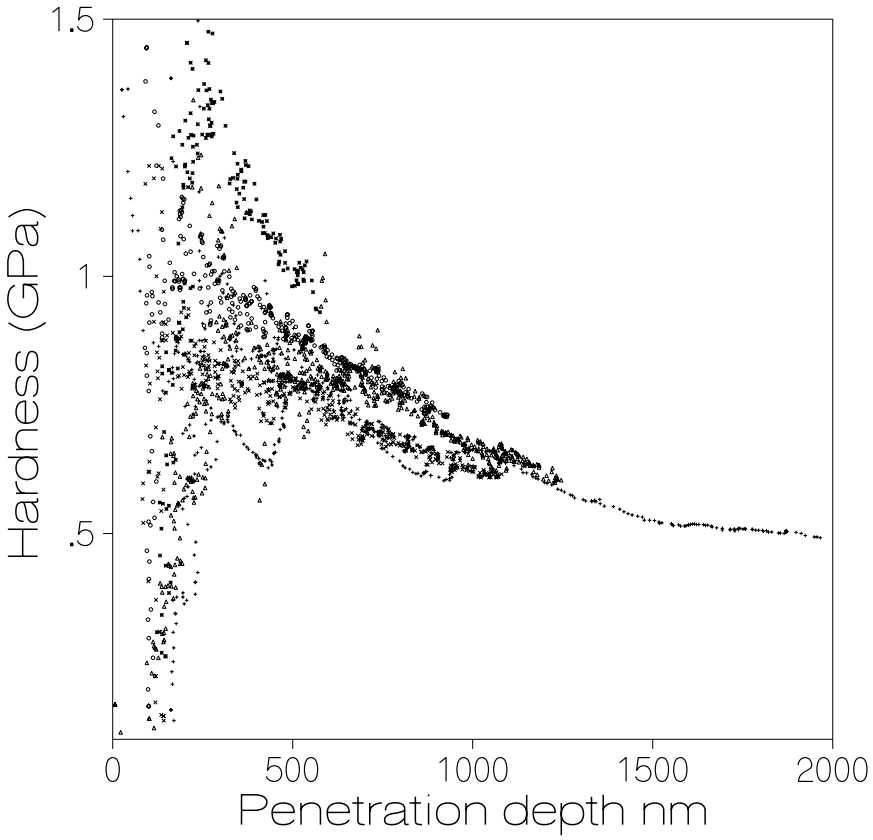

Figure 3.24: Variation of Hardness with penetration depth

from the conventional stylus profilometry.

Figure 6.4 (chapter 6) shows the same data corrected for the effect of surface roughness. It can be seen that the hardness varies as $1 + c_1/h$, as reported in literature [82]. The very high value ($\approx$ $10GPa$) of hardness at penetration depths of less than 100 nm could be attributed mainly to the presence of oxide layer in the copper surface.

Chapter 4

Single Asperity Contacts in Indentation

4.1 Introduction

Hardness estimated from nano-indentation tests has been found to depend on the size of the indent, the hardness increasing with decreasing penetration in the submicrometric regime [76] (figure 3.24). The reason for this could be that the strength of the material is high for small deformation volumes. Even though independent experimental evidence exists [1] to support this, the phenomenon is not well understood. There are a host of other factors like presence of oxide layers, measurement errors, etc., (section 1.3) that contribute to this behaviour [65]. It is also found that the scatter in the measured hardness value is high at lower penetration depths and is found to decrease with increasing penetration.

It has been recognised for sometime that roughness of the indented surface may contribute to the error in hardness measurement. Tabor [97] noted that the effect of roughness on hardness estimation is negligible if the indentation depths are much greater than the surface roughness, as is the case in conventional hardness measurements. However in the microhardness and nanohardness measurements, the surface roughness could significantly affect the estimations.

The easiest way to minimise the effect of roughness on indentation measurements is to polish the surface such that the maximum asperity heights are less than one order of the penetration depth. The diamond polishing or electro-chemical polishing used widely to prepare the surface for indentation, will generate a surface whose R_z value (the difference between the maximum and minimum value of the roughness profile) is about 50 nm. This would mean that the hardness estimated from a penetration depth of less than 500 nm is influenced by surface roughness. Keeping with the spirit of the design (chapter 3) to characterize the errors and to account for it later in data processing, the effect of surface roughness

is studied in detail. This chapter describes experimental study which simulate single asperity contact. Chapter 5 addresses the scatter resulting from indenting the rough surface through numerical simulation. Based on these studies, a model is proposed in chapter 6 to estimate the variation of the mean hardness of a rough surface with penetration depth.

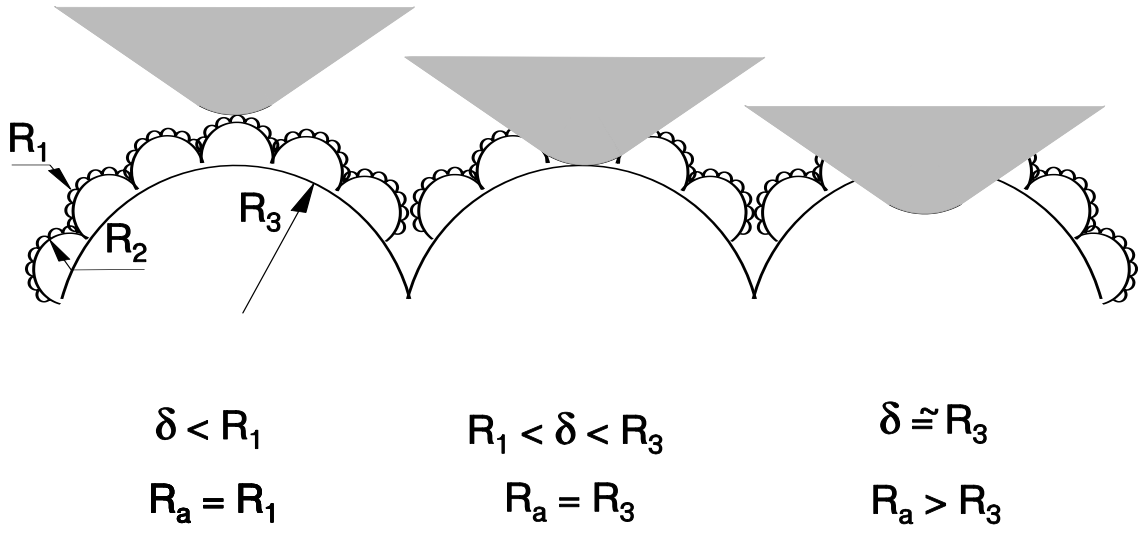

Figure 4.1: Schematic of Indentation on a rough surface

The roughness of the surfaces can be represented as a series of sinusoidals, with a broad spectrum of wavelengths [100]. Recent measurements with instruments that has very high lateral resolutions (such as Atomic Force Microscope, Scanning Tunnelling Microscope, etc.,) establish that the smallest wavelengths is of the order of atomic dimensions [11]. The simplest model of roughness [3] is that of a small hemispherical asperities riding on the back of larger asperities (figure 4.1). The radius of the asperities range from the atomic dimension to the maximum asperity size ($\approx R_z$). It is next to impossible to fabricate an indenter which is sharp down to atomic levels. Even if such an indenter is made, the tip will break at the first contact. A practical indenter is blunt with a tip radius of about 100 nm or more. The simplest geometry that can represent such an indenter is a hemispherical tip blending smoothly into the regular shape such as triangular pyramid etc.

When such an indenter is brought into contact with a rough surface, the first contact is established with the smallest asperity (figure 4.1). The radius of the asperity that affects the hardness measurement is of the order of the penetration depth. As the penetration depth is increased, the effect of smaller asperities (R_1 in figure 4.1) average out and the next larger

asperity (of radius R_2) starts influencing the indentation. At much higher penetration the asperity radius tends towards infinity and the response is that of an ideally flat surface.

The hardness measured at a particular penetration depth on a rough surface is thus approximately equal to the hardness obtained by indenting a hemispherical asperity with a spherical indenter. The radius of the asperity is determined by the nature of the rough surface and the penetration depth, while the radius of the spherical indenter is equal to tip radius of the actual indenter. Depth sensing experiments were carried out on a macroscopic hemispherical asperity with a spherical indenter. The scale has been magnified, to eliminate the influence of variation of the strength of the material with deformation volume or the penetration depth, observed at submicron depths. The study of a sphere indenting another sphere is also of relevance in powder compaction studies [54]

4.2 Analysis

Hardness (H) is taken to be equal to the mean pressure (p_m) experienced in indentation of a flat surface bounding a solid material.

$$H = p_m = \frac{P}{A(h)} \tag{4.1}$$

where P is the indentation load for a penetration h of the indenter and $A(h)$ is the area function of the indenter tip [76, 77] giving the projected area of the indent. If the surface is curved then the projected area will also depend on the radius of curvature of the indented surface and the location of an indent on the curved surface. In such a case the hardness obtained using equation 4.1 differs from the flat surface hardness. The difference should vary with the radius of curvature and the location of the indent on the curved surface. The dependence of the measured hardness on these parameters are explored here by indenting spherical bodies of different radii (R_a) and heights (h), at different location (θ) by an indenter of radius (R_i) (Figure 4.2).

The axis of the indenter (AB) is the axis along which the load is measured and passes through the indenter tip sphere. The specimen axis (OC) is parallel to the indenter axis but passes through the center of the specimen sphere. Let x be the distance between the axes of the indenter and the specimen (Figure 4.2). The initial contact is established at the point which lies on the line joining the centers of the curvature OA as shown in figure 4.2. If the indenter is now displaced by h along its axis, then the displacement along the line OA is

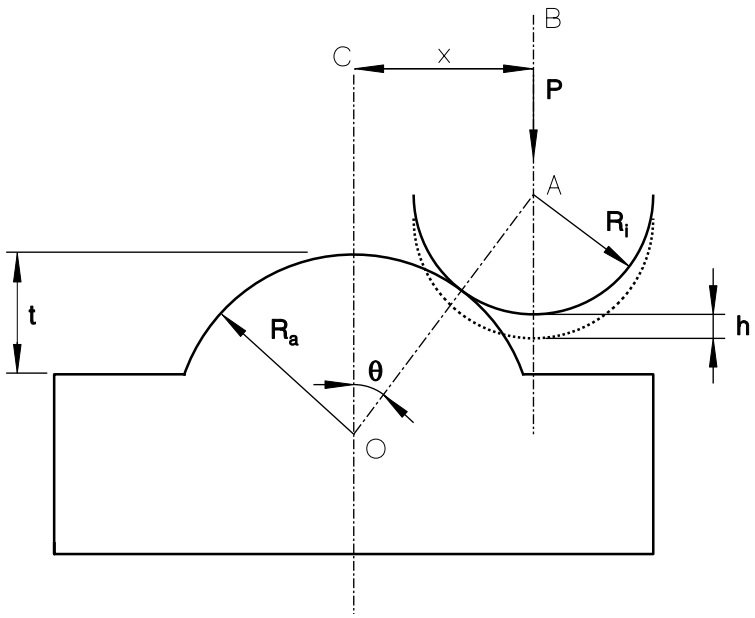

Figure 4.2: Schematic of asperity and indenter contact configuration

given by

$$h_n \approx h \cos\theta \tag{4.2}$$

for $h \ll R_a$ *or* R_i, with

$$\theta = \sin^{-1}\left(\frac{x}{R_a \ + \ R_i} \right)$$

The sum surface of the contact [35] will be a hemisphere (Figure 4.3) with reduced radius

$$R_e = \frac{R_a \ R_i}{R_a \ + \ R_i} \tag{4.3}$$

The contact area can then be approximated to $2\pi \ R_e \ h_n$. Thus the normal load P_n is

$$P_n = p_m \left(2\pi \ R_e \ h_n\right) \tag{4.4}$$

This can be resolved along the axis of the indenter as

$$P = P_n \ \cos\theta \tag{4.5}$$

and perpendicular to that axis as $P_s = P_n \sin\theta$.

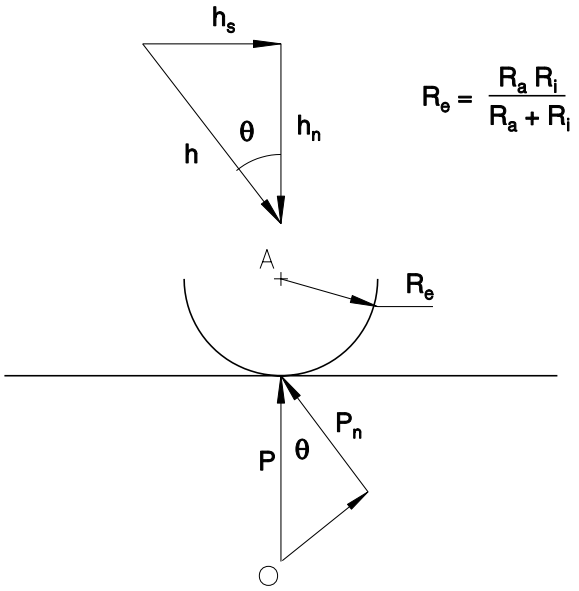

Figure 4.3: Sum surface of the contact

In an indentation experiment only the load (P) and the displacement (h) along the axis of the indenter are measured and the hardness is obtained from equation 4.1 using these parameters. For the spherical tipped indenter the area function is

$$A(h) = \pi \left(2\ R_i\ h\ -\ h^2 \right) \tag{4.6}$$

which can be approximated to

$$A(h) = 2\pi\ R_i\ h \qquad \text{for}\ \ h \ll R_i. \tag{4.7}$$

substituting for P and h from equations (4.5) and (4.2) in equation (4.1) and using (4.7),

$$H = \frac{P_n\ \cos^2\theta}{2\pi\ R_i\ h_n}$$

eliminating P_n using equation (4.4) and substituting for R_e from equation (4.3)

$$H = p_m \left(\frac{R_a\ \cos^2\theta}{R_i\ +\ R_a} \right) \tag{4.8}$$

Thus the hardness measured in a nano-indentation experiment can be expressed as a product of a geometry factor in parentheses (Equation 4.8) and the material property p_m. The mean pressure p_m is the flat surface hardness which is predictable known Youngs' modulus E, poissons ratio ν and yield strength Y [14, 37, 46, 111].

4.3 Experimental Details

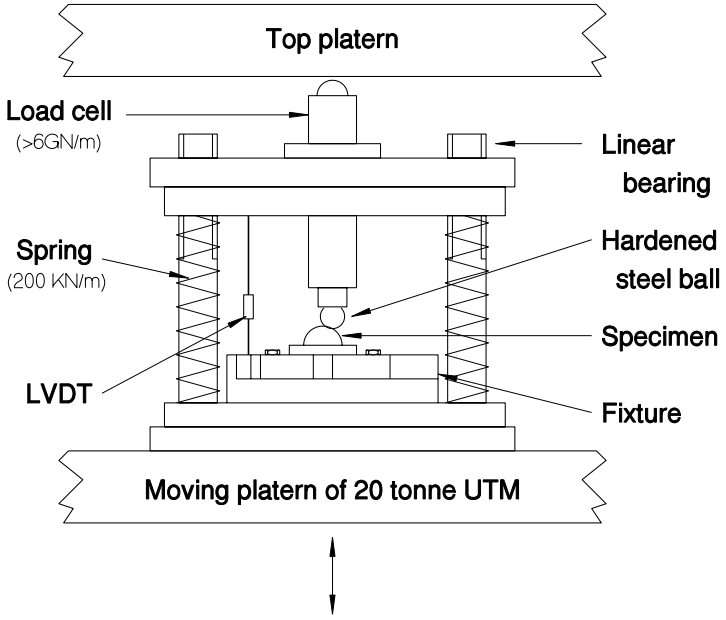

Figure 4.4: Schematic of the experimental setup

Indentation experiments were carried out in a set up as shown in figure 4.4, using a hardened steel ball of radius (R_i) 12.5 mm as the indenter. Specimens as shown in figure 4.2, and of three different radii (R_a), i.e 25 mm, 12.5 mm and 8 mm were machined out of copper rods in a copying lathe. A fixture was used to position the specimen such that the distance between the specimen and indenter axes (x) can be varied. Indentation was carried out in a 10 ton ($\approx 100KN$) universal testing machine. The load (P) is measured with a load cell of strain gauge type. The displacement (h) is measured with a Linear Variable Differential Transformer (LVDT). The data is acquired with the help of a personal computer.

The experimental material stiffness was found (= 0.05 GN/m) to be two orders less than the total machine stiffness of 6 GN/m.

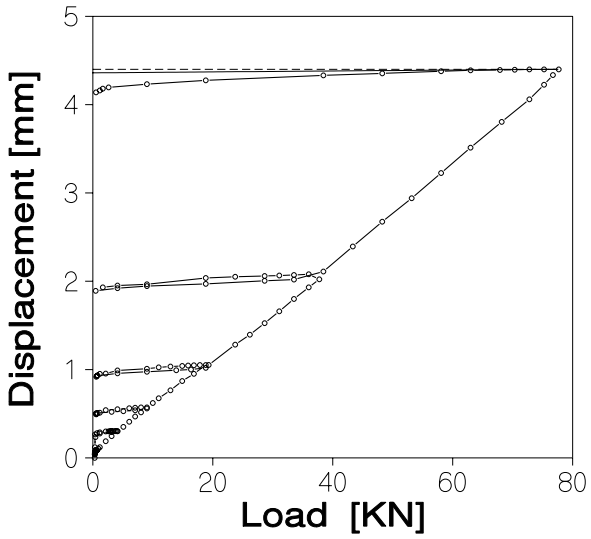

Figure 4.5: A typical Load - Displacement graph $R_a = 12.5mm, \theta = 0^o$, — tangent to the initial portion of the unloading curve, - - - displacement corresponding to maximum load

A typical load-displacement curve obtained from the experiment is shown in figure 4.5. The hardness is measured by drawing a tangent to the unloading portion of the curve and taking the x-intercept of this tangent for calculating the area of residual impression [30]. However, from figure 4.5 it can be seen that the initial portion of the unloading path is nearly normal to the penetration axis. Hence, the maximum penetration depth is used here to calculate the hardness. The difference between the maximum penetration (4.4 mm) at 80 KN load and the residual penetration at no load was found to be 0.04 mm. This was considered to be small and therefore neglected. The hardness is calculated as,

$$H = \frac{P}{A(h)} = \frac{P}{\pi\ (2R_i h - h^2)} \tag{4.9}$$

Indentation experiments were carried out on a flat specimen and the hardness estimated from these experiment is taken as p_m.

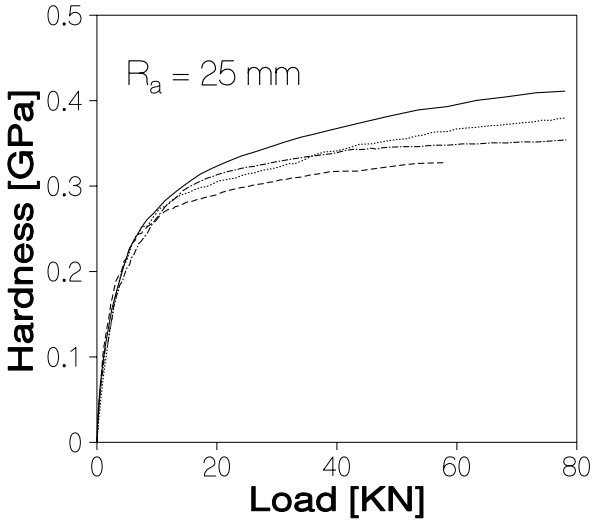

Figure 4.6: Variation of hardness with load on $R_a = 25mm$ for different angular locations (θ) of the indenter, — 0^o, $\cdots$ 4.5^o,– ·– 11.5^o, - - 28.7^o

It has been found that for a high value of θ, the indenter slides over the specimen. The maximum value of θ at which the experiments are carried out, is less than the value at which the sliding occurs for a given radii of the specimen (R_a). Further, to minimise the effect of friction, copious amount of lubricant SAE 20/30 was applied to the indenter as well as to the specimen.

4.4 Results and Discussion

Figures 4.6 and 4.7 show the variation of mean pressure (estimated using the recorded load P - displacement h graph) with load. The mean pressure decreases with increasing angle of contact (θ) and increases with increasing radius of the model asperity (R_a). When all the test data are summarised and plotted as a function of $R_a \cos^2\theta$ / $(R_i + R_a)$, then figure 4.8 shows the experimental results to fall roughly on a straight line. This validates equation 4.8 and indicates that it can be used to estimate flat surface hardness by deconvoluting the mean pressure measured at any locations of a spherical surface. Figure 4.8 further provides

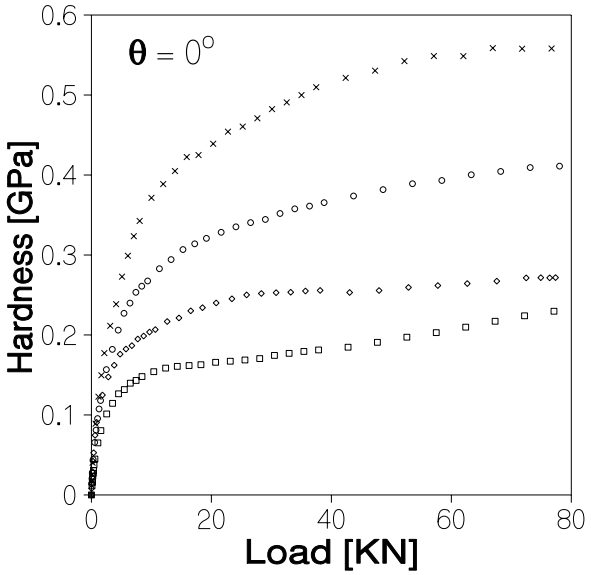

Figure 4.7: Variation of hardness with load at $\theta = 0^o$ for different asperity radii (R_a), □ 8mm, ◇ 12.5 mm, ○ 25 mm, × flat surface

a support for the approach used here to model the geometric effect of surface roughness on hardness measurement. Some of the implications of present findings especially for nano-indentation results are discussed below. It is assumed that the asperity profiles are spherical and the contact (of the indenter) is always with a single asperity.

For a rough surface the summit curvature of asperities has a Gaussian probability distribution [107]. An uniform probability distribution could be associated with θ. Given these distributions, it should be possible to use equation 4.8 to obtain the expected scatter in nano-indentation, due to geometric variations alone. It is likely that the curvature itself varies from tip to base of an asperity. Such variation will also affect the nature of the scatter. This is further explored in chapter 5

The distribution of radius of curvature however depends on the scale used to make the roughness measurement [88]. This notion leads to a surface architecture which is perhaps illustrated in its simplest form by Archard [3]. Archard's two dimensional architecture, validated atleast in principle by a later discovery of the fractal nature of rough surface [61], consists of uniform spherical asperities carrying asperities of smaller radius (Figure 4.1).

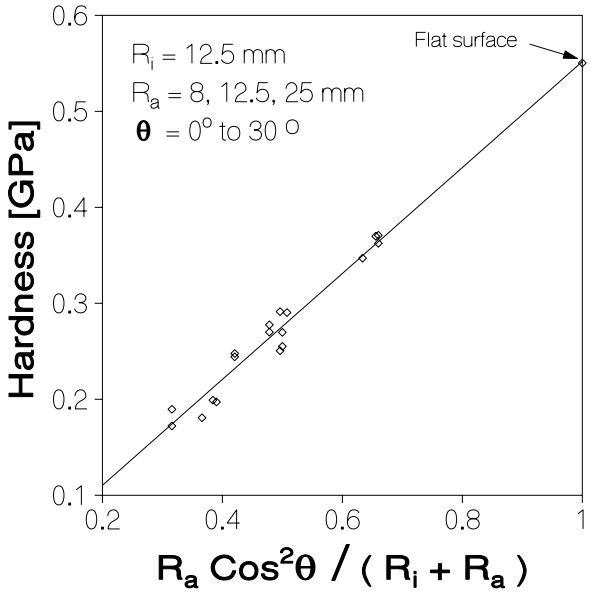

Figure 4.8: Plot of hardness versus $R_a \cos^2\theta$ / (R_i + R_a), ◇ experimental, — eqn(8)

This hierarchy progresses till the asperity radius becomes zero. Let a nano-indentation test be carried out on such a surface such that the total penetration never exceeds the height of the asperity with the largest radius. Contact is first established with the asperity of the smallest radius, which at this stage can be considered to be a semi-infinite half space, since the contact area is much smaller compared to the radius. As per the present findings the mean pressure recorded at this stage is the lowest. As the penetration proceeds well into the asperity the semi-infinite nature of the configuration breaks down and the mean pressure becomes increasingly influenced by the lower level of asperity in the hierarchy which has a larger radius. The mean pressure starts to increase accordingly.

Figure 4.9 shows that for a spherical section of 12.5 mm radius and 6 mm maximum height, the mean pressure does not change a great deal from that corresponding to the 12.5 mm maximum height section up to a penetration of 2 mm. The mean pressure increases beyond this penetration steadily, with increasing displacement.

This indicates that for the model of rough surface considered here, the semi-infinite nature of an indented asperity is lost when the penetration exceeds about one-third the

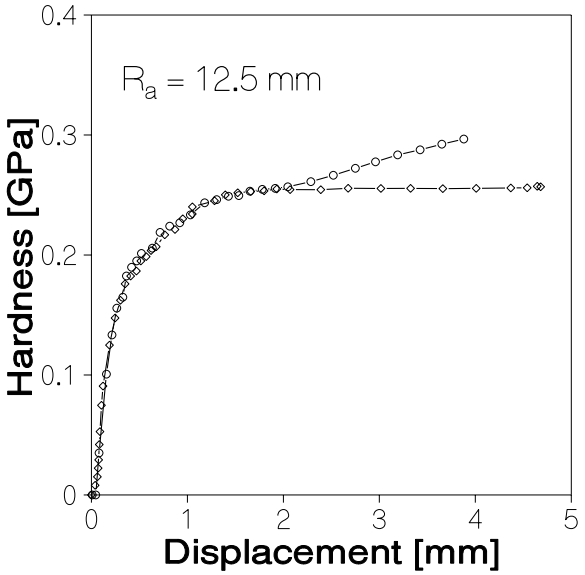

Figure 4.9: Effect of asperity height (h) on the hardness, $R_a = 12.5mm$ $\diamond$—$\diamond$ $h = R_a$, $\circ$—$\circ$ $h = R_a/2$

asperity height. Beyond this penetration, the mean pressure rises with penetration and is likely to become asymptotic to that corresponding to the next higher asperity radius when the penetration exceeds the top asperity height. For an ideal surface where the asperity radius may vary from zero to infinity in infinite number of steps one may therefore expect a mean pressure curve to ascent smoothly with load to become asymptotic to the flat surface hardness which of course corresponds to the mean pressure of an asperity of infinite radius. Therefore the nano-indentation of a rough surface should yield, a hardness *vs* load or penetration characteristic which has a positive slope, in the absence of

1. any systematic variation in mechanical property in the near surface region and

2. any error in displacement measurement.

For the slope to be negative the contact has to be conformal with a negative radius of curvature. As this is not possible, the negative slope generally [76] recorded in nano-indentation tests must be due to genuine variations of mechanical property and material structure in the near surface region.

Known the area function, the hardness *vs* load/penetration characteristic is derived from the recorded load-displacement data. The area function is generally a quadratic [76], [77] in penetration (h). Any error in the estimation of this function, introduces large error in the estimation of hardness [30].

To study this, a defect was introduced in the present spherical indenter by pressing it against a hard surface. This created a flat, situated at 0.18 mm from the tip along the the indenter axis. Indentation experiments were carried out as before but hardness was estimated using equation 4.9.

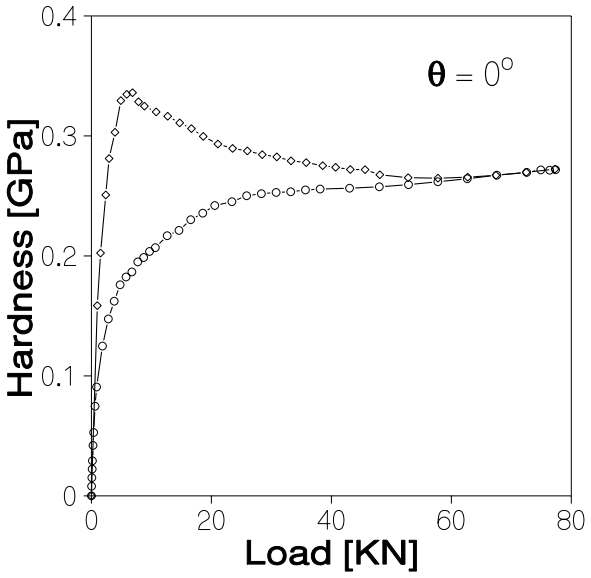

Figure 4.10: Hardness estimated using a defective indenter, $R_a = 12.5mm$, $R_i = 12.5mm$, ○—○ spherical indenter, ◇—◇ defective spherical indenter, having a flat face normal to the indentation axis at 0.18 mm from tip

Figure 4.10 shows the hardness values obtained using the defective indenter, along with hardness obtained using the spherical indenter. The slope of the hardness-penetration characteristics for a defective indenter is negative for loads greater than 5 KN. Such trends have been reported by Alonso *et. al.* [2].

The actual area function for the defective indenter is

$$A(h) = \pi \left\{ 2\, R_i(\ h\ +\ h_e\ ) - (\ h\ +\ h_e\ )^2 \right\} \tag{4.10}$$

Equation 4.6, which has been used to obtain hardness, can be obtained from this equation by replacing h by $(h - h_e)$. This means equation 4.6 corresponds to a situation where the penetration depth is underestimated by h_e. Thus any underestimation in depth measurement will result in increased hardness at lower loads.

In nano-indentation tests there is always a strong possibility for the penetration to be underestimated. This may be due to the blunting of the indenter tip or error committed in the establishment of point of contact. The contact point is detected [65] later than the actual contact due to a finite resolution of the measuring system and noise. This leads to the projected area being underestimated. For a measured displacement of h the load corresponding to a displacement underestimation of h_e is,

$$P = p_m\ k\ (\ h\ +\ h_e\ )^2$$

where k is a constant related to the indenter geometry. Noting that the estimated projected area of contact is $A(h) = kh^2$, the hardness is

$$\begin{aligned} H &= p_m \frac{k\ (h + h_e)^2}{k\ h^2} \\ &= p_m \left(1\ +\ (\frac{h_e}{h})^2\ +\ 2\ \frac{h_e}{h} \right) \\ &= C_1\ +\ \frac{C_2}{h}\ +\ \frac{C_3}{h^2} \end{aligned}$$

where C_1, C_2, C_3 are constants. What may be of some concern is that such trends brought about by inevitable artifacts may be very similar to the genuine trends in mechanical property with penetration [76]. There may thus be situations where it will be impossible to separate the artifacts from the genuine trends.This points to the inherent weakness of using hardness as a measure of mechanical response of surfaces and near surface zones of solids.

4.5 Conclusions

1. Hardness estimated from indentation of a spherical body by a spherical indenter increases with the radius of the body and varies with location of contact.

2. Known the contact location and radius of curvature it is possible to use a simple geometric model to deconvolute the flat surface hardness.

3. In nano-indentation where penetration depths are of the same order as the roughness dimensions, roughness in the absence of any error in displacement measurement and any variation in mechanical property with penetration, effects a scatter and may be responsible for a positive slope in the hardness-penetration characteristics.

4. In nano-indentation where an error in displacement measurement may be of the same order as the displacement itself any underestimation of penetration leads to a negative slope in the hardness-penetration characteristics.

Chapter 5

Multiple Asperity Contacts in Indentation

When the indenter tip radius is considerably large compared to the asperity radius, as when the penetration depth is much smaller than the surface roughness, then the contact can no longer be said to be that of a single asperity. This corresponds to $R_a \ll R_i$ in the analysis of chapter 4. Multiple asperity contacts are difficult to analyse analytically.

The problem of the contact of elastic bodies whose nominally flat surface has one dimensional wave of small amplitude has been solved by Westergaard [106] using complex variable method. Asymptotic solutions for contact of two-dimensional flat surfaces has been obtained by Johnson *et al.* [47]. The elastic contact of a sphere on a gaussian rough surface was first analysed by Greenwood and Tripp [39]. It was found that though the contact never takes place over a circular area, an effective contact radius can be defined, which at higher load approaches the Hertzian radius. These analyses gives the contact pressures and the area. The stress distribution in the half-space is important to understand the plastic deformation.

Mann and Farris [63] have numerically found the sub-surface stress distribution for the contact of a rigid cylindrical indenter on an elastic half-space of regular cylindrical asperities, neglecting the interaction of asperities. Rajendra Kumar and Biswas [50] have used complex variable method to formulate the same problem with the asperity-asperity interaction. They found that depending upon the geometry of the asperities, the first yield can either occur at asperity level or in bulk. For a given asperity radius, the maximum shear stress will occur in sub-surface rather than in asperities when the asperity pitch is higher. Since in nano-indentation, the aim is to get the deformation properties of the sub-surface rather than the properties of the asperities, the surface has to be polished such that asperities have higher radius of curvature and are spaced far apart.

It is not always possible to polish the surface to the required smoothness. As noted in

chapter 4, it is difficult to reduce the roughness of wavelengths less than 1 μm. Due to the presence of atomic scale roughness, the assumption that the asperities can be considered as smooth spheres/cylinders is questionable.

A numerical method of analysing the elastic-plastic contact of a rigid indenter with a rough surface is developed in this chapter. The rough surface is simulated using a fractal function to characterise the roughness wavelengths that affect the nano-indentation. The scatter arising due to surface roughness is studied through numerical simulation.

5.1 Simulation

5.1.1 Rough Surface

Conventionally, the undulations of a surface about its mean plan is assumed to be a random process and the surface is characterised by statistical parameters such as variances of height, slope and the curvature [100]. The various rough surface contact analyses whether it is elastic [40] or plastic [72, 85] or elasto-plastic [35] use these parameters for modelling the rough surface.

It has been found that the variances of the slopes and curvature of the rough surface depend strongly on the distance between the points at which the surface is sampled [99], i.e the horizontal resolution of the profilometer. Sayles and Thomas [88] have established that the surface topography is a non-stationary random process for which the variance of the heights is related to the length of the sample and that the power spectrum follow a power law for several decades of the wavelength of the roughness. Thus the statistical parameters used in modelling depends on the scan length and the horizontal resolution.

The fractal simulation [62] of the rough surface overcomes this problem by using a scale-invariant parameter – fractal dimension(D). The measures (M) such as length, area or volume of an object is obtained as a sum of respective small units (ϵ, ϵ^2, ϵ^3), in Euclidean geometry as

$$M = \sum \epsilon^D$$

where D is an integer. Generalising this concept, the fractal geometry is obtained in which D can take non-integer values and is defined as Hausdorff dimension or the fractal dimension. For a curve the value of D would be between 1 and 2. The fractal dimension gives the information about how much the area filling the curve is or the amount of cringiness in the curve.

5.1.1.1 Weierstrass-Mandelbrot Function

The Weierstrass-Mandelbrot function [8] is given by

$$Z(x) \;=\; \sum_{n=-\infty}^{\infty} \frac{(1 \;-\; \exp(i\gamma^n x))\;\exp(i\phi_n)}{\gamma^{(2-D)n}} \;\;;\quad (1 \;<\; D \;<2,\; \gamma \;>1,\; \phi_n \;=\; arbitrary\, phase)$$

with D as the fractal dimension, and ϕ can be chosen to make $Z(x)$ either deterministic or stochastic. For a deterministic function ϕ can be chosen as $\phi = \mu n$. This function is continuous, non-differentiable and obeys the self-affine scaling law,

$$Z(\gamma x) \;=\; exp(-i\mu)\;\gamma^{2-D}\;Z(x)$$

With $\mu \;=\; 0$ the real part of this function can be used to represent the height variation Z(x) of an isotropic and homogeneous rough surface in any arbitrary direction, along a straight line as [62],

$$Z(x) \;=\; G^{(D-1)} \sum_{n=n_l}^{\infty} \frac{\cos(2\pi\gamma^n x)}{\gamma^{(2-D)n}};\quad 1 < D < 2;\quad \gamma > 1; \tag{5.1}$$

In this G is a scaling contact, D is the fractal dimension of the profile and $\gamma = 1/\lambda$ is the frequency mode corresponding to the reciprocal of the wavelength (λ) of the roughness and n_l is the lower cut off frequency of the profile which depends on the length of the sample (L) through the relation $n_l \;=\; 1/L$, γ is chosen to be 1.5 for phase randomization and high spectral density.

This function has a power spectrum which can be approximated by a continuous spectrum [8] given by

$$P(\omega) \;=\; \frac{G^{2(D-1)}}{2\,\ln\gamma}\frac{1}{\omega^{(5-2D)}} \tag{5.2}$$

Thus the slope of the power spectrum in log-log plot gives the fractal dimension D. The constant G is a characteristic length scale of a surface which is invariant with respect to the roughness frequency and determines the position of the spectrum along the power axis. This constant is related to the parameter topothesy introduced by Sayles and Thomas [88].

The equation 5.1 can be used to simulate the roughness profile along a line. The values of G and D to be used in the simulation can be obtained from the power spectrum of a measured profile. Figure 5.1 shows the simulated profile and the actual profile measured on a polished metal surface using an atomic force microscope.

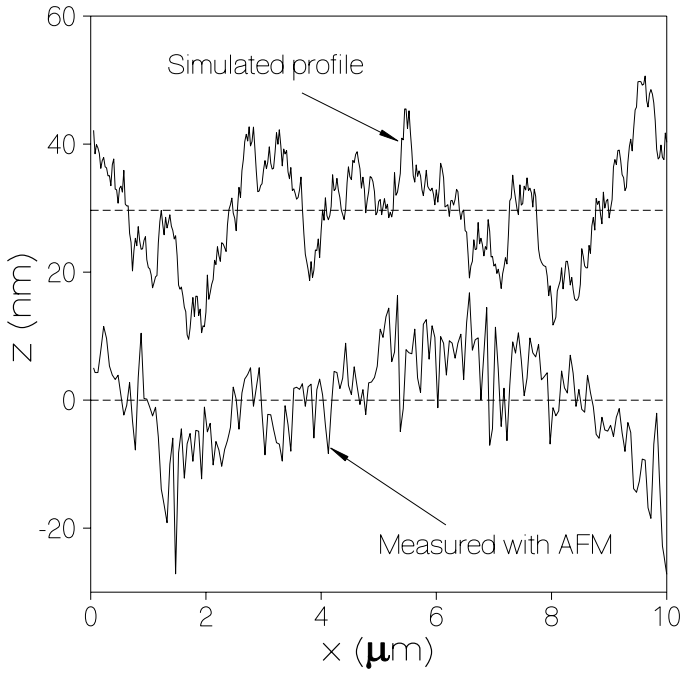

Figure 5.1: Roughness profile of a polished surface compared with the simulated profile

5.1.1.2 Surface Simulation

The spectra of the profiles measured along a line, do not contain complete information about the surface, as the stylus of the profilometer rides over the shoulders of the asperities and rarely goes over the summit or into the deepest valley. For isotropic surfaces, Nayak [72], has established the relation between the spectrum of a surface and its profile along an arbitrary direction. For the profile with a spectrum given by equation 5.2, surface spectrum [62] is

$$P^s(\omega) = \frac{(5-2D)\,(7-2D)}{\pi}\frac{G^{2\,(D-1)}}{2\,\ln\gamma}\int_0^{2\pi}\frac{\left\{\cos^{(5-2D)}\theta - \cos^{(7-2D)}\theta\right\}d\theta}{\omega^{(6-2D)}}$$

The equation of the surface with this spectrum is

$$Z(x,y) \;=\; F(D)\,G^{(D-1)}\sum_{n=n_l}^{\infty}\frac{\cos(2\pi\gamma^n\{x+g(y)\})\cos(2\pi\gamma^n\{y+g(x)\})}{\gamma^{(2-D)n}};\;\; 1<D<2;\;\; \gamma>1; \tag{5.3}$$

with

$$F(D) \;=\; \left(\frac{2}{\pi}(\ln\gamma)\;(5-2D)\,(7-2D)\int_0^{2\pi}\left\{\cos^{(5-2D)}\theta - \cos^{(7-2D)}\theta\right\}d\theta\right)^{0.5}$$

and

$$g(a) = \frac{1}{2 \times 2^{0.5}} \frac{\gamma^{(2-D)(n_l-1)}}{\{\gamma^{(4-2D)} - 1\}^{0.5}} \sum_{n=n_l}^{\infty} \frac{\cos(2\pi\gamma^n a)}{\gamma^{(2-D)n}}$$

A value of 1.5 is chosen for D, giving the fractal dimension of the surface as

$$D_s = D + 1 = 2.5$$

which corresponds to a brownian surface [61]. The function $g(a)$ is introduced to randomise the phases such that for each value of y, the profile along x has different phases [62].

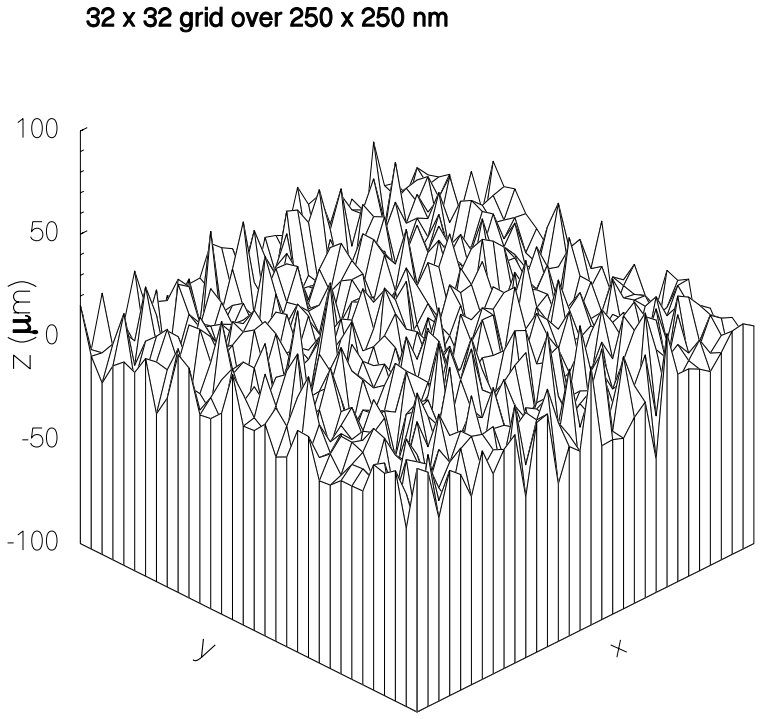

Figure 5.2: Simulated fractal surface

The summation to infinity is cut off at a higher index. The indices are chosen to be 34 & 52 respectively, such that the roughness is simulated in the same length scale as the physical phenomena - the indentation to be studied. The surface is simulated by evaluating the equation 5.3 over a grid of 128 x 128 uniformly spaced points. Figure 5.2 shows a part of the simulated surface.

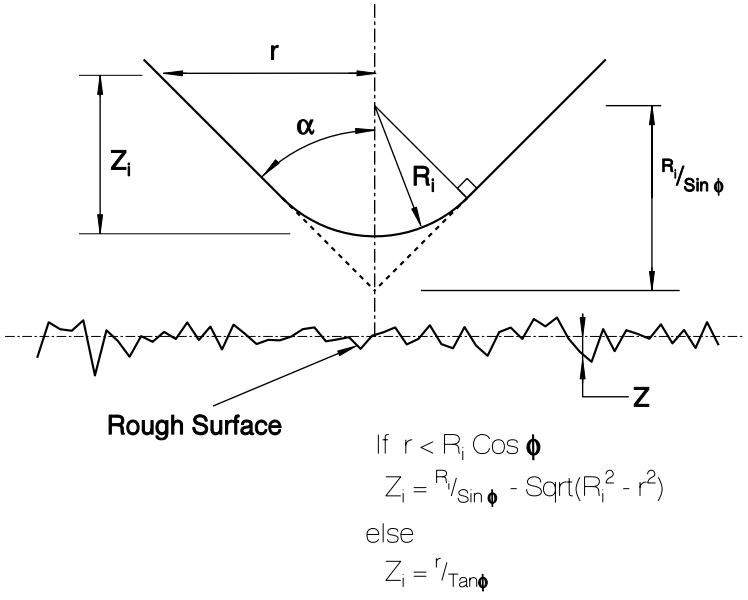

Figure 5.3: Schematic of the indenter configuration on a fractal surface

5.1.2 Indenter

The geometry of the indenter used is shown in figure 5.3. The half cone angle (α) and the tip radius of curvature (R_i) are varied to get the different area function. The surface of the indenter Z_i is generated over the same set of grid points as the simulated rough surface. The axis of the indenter is varied randomly over the x-y plane, within the $1\mu m \times 1\mu m$ simulated surface. 25 such random indentations are carried out for a given indenter parameters α and R_i.

5.1.3 Indentation

The smooth indenter is brought into contact with the simulated surface and the real contact area is obtained. For this, first the sum surface [35] is found using

$$Z_s = Z_i - Z$$

Z_s gives the difference in height between the indenter Z_i and the rough surface Z (Figure 5.3). The contact area for a particular penetration (h) of the indenter into the rough surface is

the contour of the sum surface for the value of Z_s equal to d. The contours were obtained using a standard algorithm that uses linear interpolation for the Z_s values in between the grid points.

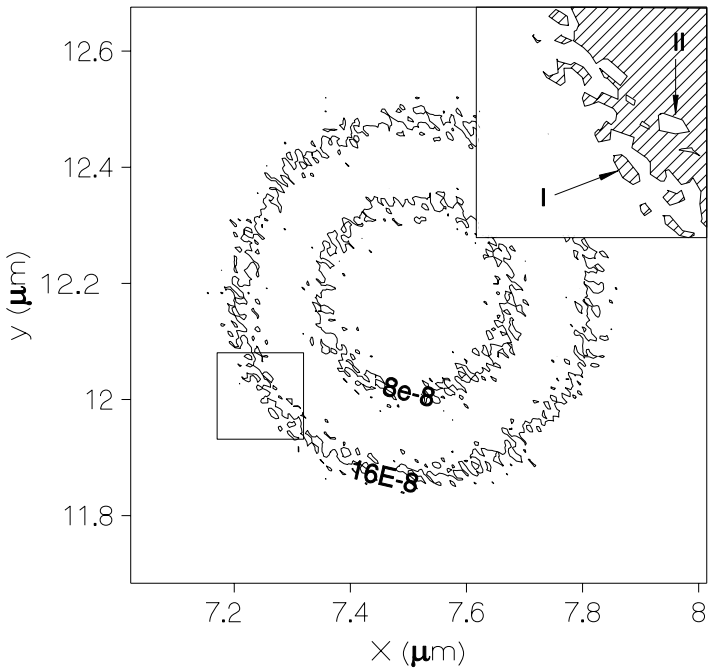

Figure 5.4: Actual contact area of a conical indenter on a fractal surface

A typical real contact area is shown for two penetrations as shown in figure 5.4. There are two types of islands that can be identified in this figure. One is the island of contact area surrounded by region that is not in contact and the other is the hollow island surrounded by contact region. These two types are differentiated by comparing the z-values of a point inside the contour, with that of a point outside the contour. The algorithm [94] for finding out whether a point is inside or outside a closed curve is based on the property that a line joining a point inside a closed curve with a point outside has to intersect the curve an odd number of times. The area A_i of these contact islands is found by numerical integration employing the trapezoidal rule.

5.2 Contact Model

The indentation of a soft rough surface by a smooth and hard indenter is equivalent to the penetration of a soft, smooth and flat surface by a set of hard asperities [97]. From the volume and the area of a contact island, the spherical cavity model [46] is used to estimate the mean pressure (p_i) acting over the contact island as,

$$p_i = \frac{2}{3} Y \left\{ 2 + \left[\ln \frac{\frac{E \tan\beta}{2Y} + 2(1-2\nu)}{3(1-\nu)} \right] \right\} \tag{5.4}$$

where E is the Young's modulus, Y is the yield strength and ν is the Poisson's ratio of the material being indented. $\tan\beta$ is obtained by equating the volume of the contact island to that of a cone of attack angle β, whose base area is equal to the contact area of the island. It is assumed that the indenter deformation is negligible. The upper limit to this mean pressure is set by the condition of fully plastic deformation. Thus the load supported by each island is computed as

$$P_i = \begin{cases} p_i \times A_i & if \;\; p_i < 3 \\ 3 \times Y \times A_i & if \; p_i \geq 3 \end{cases}$$

where A_i is the contact area of the individual islands. The total load is obtained by summing up the individual load supported by all the islands for a given penetration.

The hardness is then obtained by dividing this load with the apparent area function obtained from the area function of the indenter. The area function for a given indenter geometry is computed using the same routine but by letting the indentation be done on a plane surface. The reference from which the penetration depth is measured, to get the area, can be obtained in two different ways. One is to set zero to the initial contact point of the indenter with the rough surface. This stimulates a depth sensing indentation experiment with ideally infinite measurement resolution. The other is to set the zero to the mean plane of the rough surface. This stimulates the imaging type of nano-indentation experiments [11]. The area function for a given indenter geometry is computed using the same routine but by letting the indentation be done on a smooth flat surface.

The indentation was carried out at 25 random locations on the simulated surface and the load was found out for 11 different penetration depths at a given location. The rms roughness (h_r) of the indented surface is varied by varying the magnification constant G in equation 5.3 [61]. 6 different rough surfaces with h_r ranging from 0.62 nm to 2.16 nm were generated for the indentation. To introduce the effect of the varying material property with the deformation volume or the penetration depth, the yield strength Y used in the

equation 5.4 to calculate the mean pressure is allowed to vary as

$$Y \;=\; Y_0 \;(\; 1 \;+\; \frac{c_0}{V^n} \;) \tag{5.5}$$

With $n = 1/3$ this would give, for a conical indenter, a flat surface hardness variation of type,

$$H_s \;=\; H_0 \;(\; 1 \;+\; \frac{c_1}{h} \;) \tag{5.6}$$

where H_0 is the bulk hardness and c_1 is a material constant.

The simplifying assumptions involved in this model are:

1. There is no interaction between asperities, that is, the load on an asperity does not modify the geometry of other asperities.

2. The difference between the actual contact area of an asperity with the indenter and the geometrical intersecting area is neglected. That is the pile up and the elastic deformation of the asperity has been neglected. The error introduced because of this assumption is less than 20% [100].

The numerical values for the material properties used in this simulation are $E = 208$ GPa, $Y_0 = 1$ GPa and $\nu = 0.3$

5.3 Results and Discussion

The simulation was carried out for 5 different tip radii and 6 different cone angles. For each of these 11 indenter geometries, 25 indentations are carried out with the axis of the indenter positioned randomly over the simulated rough surface. For each indentation, the load was determined for 11 penetration depths of the indenter.

Figure 5.5 shows a typical hardness vs penetration graph for a tip radius of 0.1 micron and 60^o cone. It can be seen that the scatter in the hardness values increases at the lower penetration. Also the mean hardness is found to increase with decreasing penetration. This is because of the reason that the penetration depth is measured from the mean square plane fitted to the rough surface. It is interesting to observe that the mean hardness varies in a similar way as was experimentally found by Oliver *et al.* [76]. This variation of mean hardness for different condition is further detailed in chapter 6.

The magnitude of the scatter can be quantified by a non- dimensional parameter

$$S \;=\; \frac{\sigma}{M}$$

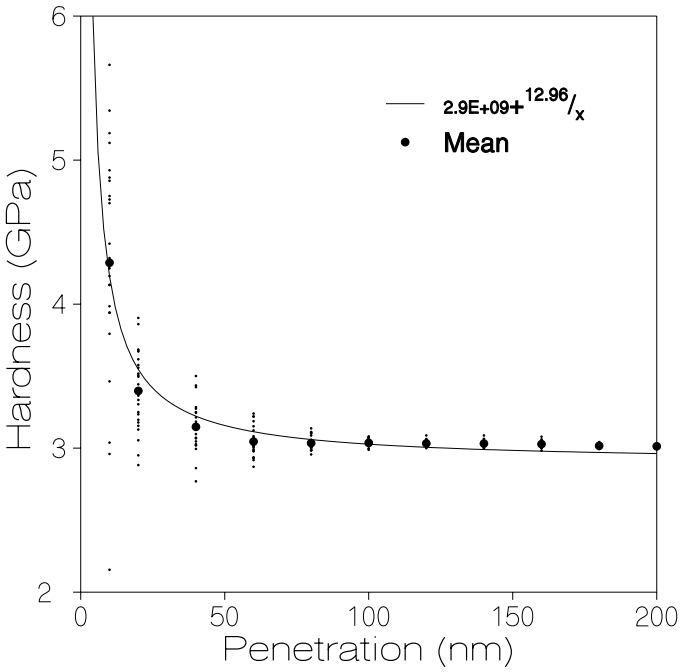

Figure 5.5: Variation of hardness with penetration

where σ is the standard deviation and M is the mean value of the hardness for a given penetration depth. For an ideally smooth surface this parameter will be identically zero. For the rough surfaces this increases at the lower penetration depths.

Figures 5.6 and 5.7 shows the variation of S with the tip radius (R_i) and the cone angle (α), for the case when the penetration is measured from the first contact and for the material whose deformation properties does not vary with depth/volume. The scatter decreases with the increasing tip radius and increasing cone angle. It can be seen that there is a minimum penetration depth beyond which the scatter due to surface roughness is negligible.

In figure 5.8, the scatter is plotted against the penetration (h) normalised with the rms roughness (h_r), for an indenter with the half angle (α) of 60^o. The rms roughness is obtained as

$$h_r = \sqrt{\frac{1}{n^2} \sum_{x,\ y}^{n} \left(Z(x,y) - \frac{\sum Z(x,y)}{n^2} \right)^2}$$

It can be seen from the figure that the scatter is more for the case when, hardness is obtained from the penetration depth measured from the first contact than when it is obtained from the depth measured from the mean reference plane. Also, the variation in the material property

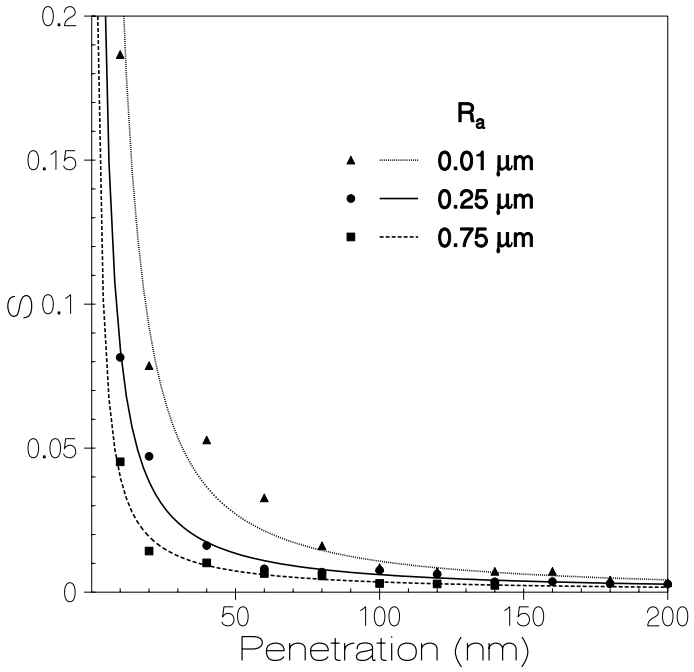

Figure 5.6: Variation of scatter with penetration for different tip radius

has very little influence in the scatter.

In Figure 5.9 the scatter obtained for all the indenter geometries is plotted against the apparent contact area measured on a plane passing through the first contact point and parallel to the mean plane of the rough surface. The scatter clearly follows a power law. This means that the nature of the scatter depends only on the surface geometry and not the indenter geometry.

The geometry of the rough surface is mainly determined by its power spectrum. Brown and Scholz [21] observed that the power spectra of a variety of machined surfaces coincide at high frequencies. Majumdar and Tien [62] found that the power spectra at higher frequencies follow the power law of

$$P(\omega) \propto 1/\omega^2$$

where P is the power of the spectral content with frequency ω. The surface processing techniques reduce the amplitude at lower frequencies, and the spectrum of the processed

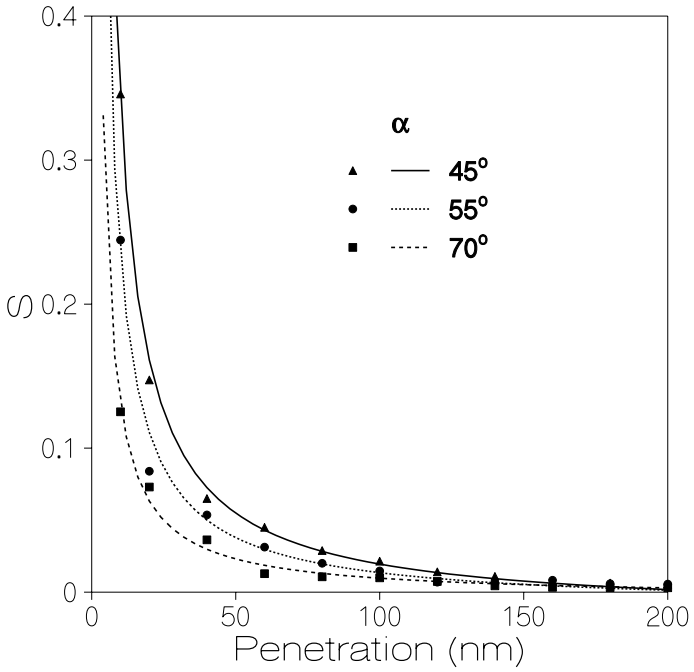

Figure 5.7: Variation of scatter with penetration for different cone angles

surface has two distinct regions

$$P(\omega) \propto \begin{cases} 1/\omega^k & \text{for } \omega < \omega_c \\ 1/\omega^2 & \text{for } \omega < \omega_c \end{cases} ; \; k < 2$$

ω_c is the corner frequency [62] and depends on the length scale such as the nose radius in turning and grain size of grinding wheel etc., involved in the processing method. The size of the indentation in nano-indentation is less than 1 micron and for most of the mechanical processing methods the length scale is more than few microns. Thus the corner frequency for most engineering surfaces will be greater than a micron. Hence, when the length scale that affect the physical process is less than a micron, as is in nano-indentation, these surfaces would follow the inverse square law for the spectral density. For a profile with a cut off length of 1 micron or less, the contribution from roughness wavelengths greater than 1 micron will not affect the profile but will simply change the mean value of the profile. This is the reason why the sample length for the simulated surface was chosen to be 1 micron. Since the geometric nature of the surface is not going to be affected, the nature of the scatter obtained in this study is applicable for all surfaces. For a given nominal contact area, the amount of

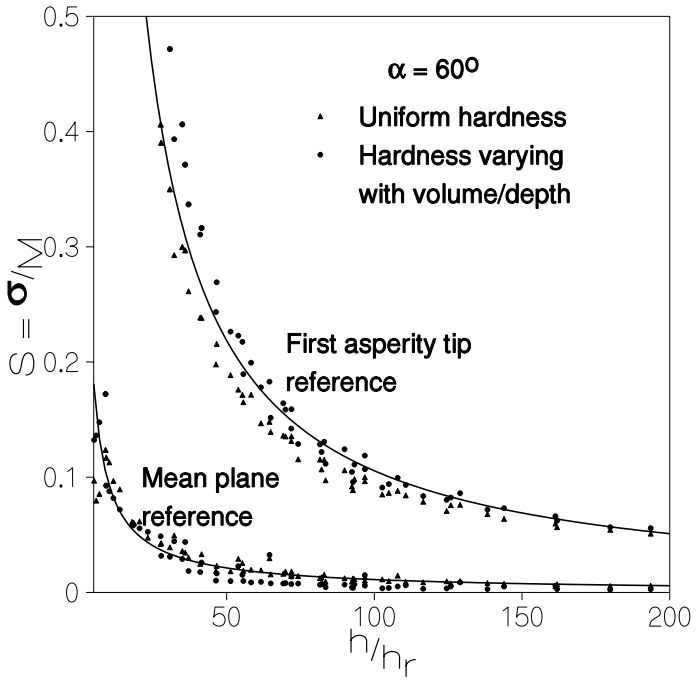

Figure 5.8: Variation of scatter with normalised penetration for conditions of indentation

the scatter in the hardness measurement due to surface roughness alone can be directly read from figure 5.9. The material constants used in this simulation are typical of the metals.

5.4 Conclusions

1. The scatter in hardness measurement decreases with increasing indenter angles and bluntness of the indenter. The scatter seems to depend on the nominal contact area, rather than the exact geometry of the indenter.

2. The variation in the deformation properties of the material with either the penetration depth or the deformation volume has very little effect on the scatter. The scatter due to surface roughness is independent of material properties for non-strain hardening material.

3. The scatter is affected by the way the area is measured to obtain the hardness. Image sensing method gives lesser scatter than the depth sensing method when there is no pile up.

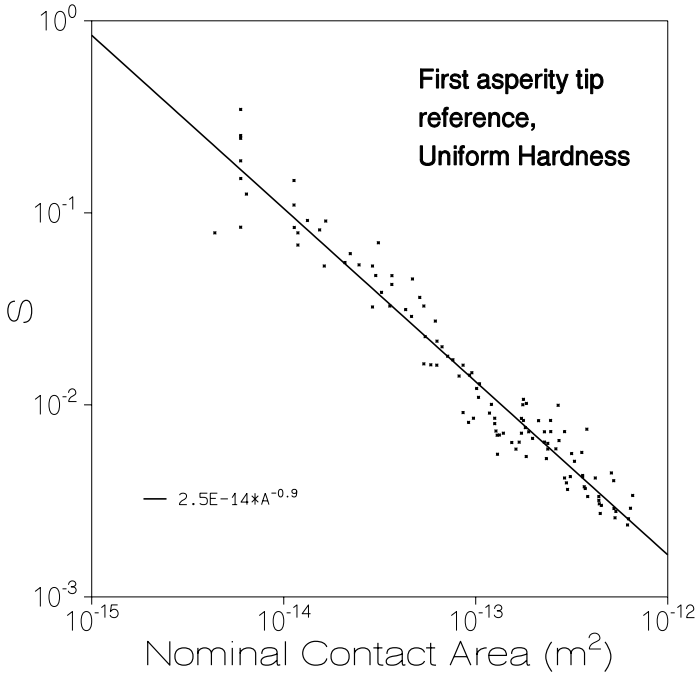

Figure 5.9: Variation of scatter with nominal contact area measured on the plane passing through the first contact point

4. If the indenter geometry and the surface roughness in the correct length scale is known, the scatter arising as a result of varying local geometry can be quantified.

Chapter 6

Effect of Surface Roughness on Indentation

6.1 Introduction

The depth sensing hardness measured on the rough surface will be less than the bulk value, when the penetration is less than the asperity height (chapter 4). This is due to the over-estimation of the projected area, as the area function assumes an ideally flat surface. The variables that contribute to this are,

1. the geometric nature of the rough surface,
2. the indenter geometry,
3. the position of the reference plane on which the residual impression is projected to get the hardness and
4. the actual variation in hardness with the penetration depth as in property gradient material or with deformation volume, due to reduced defect concentration.

The effect of the simplest geometry of the rough surface and the indenter was explored in chapter 4. However the actual geometry of the rough surface is much more complicated than the sphere. Numerical simulation method developed in chapter 5 provides a means of estimating the error due to a random non-stationary rough surface. The simulation can also take into consideration the other two variables (no.3 and 4) listed above. Given the nature of rough surface, indenter geometry and other variables, this simulation technique can determine the variation in the measured hardness with penetration depth due to surface roughness alone.

The actual variation that is obtained experimentally as in figure 3.24 is due to other factors (section 1.3) as well [65]. The numerical simulation cannot take into consideration all

these factors. If is difficult to see how these factors will interact with each other like presence of an hard oxide layer. The main draw back of the numerical simulations is that it fails to give the intuitive feel which is lost in the maze of the numbers. In this chapter a relation between the measured hardness and the penetration depth is arrived at by extrapolating the results obtained from the indentation of spheres (chapter 4). It is shown that this can be used to get more insight into the indentation by extending this relation to a case in which the material properties vary with the penetration depth/volume.

6.2 Theory

The hardness obtained from indenting a spherical surface with a spherical indenter can be written as equation 4.8 [19],

$$H = H_s \left(\frac{R_a \cos^2 \theta}{R_i + R_a} \right) \tag{6.1}$$

where H_s is the hardness of the smooth flat surface and R_i and R_a are the radii of the indenter and asperity respectively. The angle θ is small, because of the presence of neighbouring asperities. It further has very little effect on measured hardness. By expanding the term within the parenthesis and neglecting the higher order terms of $\frac{R_i}{R_a}$ (assuming $R_i \ll R_a$) the equation can be simplified to

$$\frac{H}{H_s} = 1 - \frac{R_i}{R_a}$$

R_a varies continuously for an actual rough surface from zero to infinity as the indenter penetrates into the surface. The exact relation between R_a and the penetration depth h depends on the nature of the rough surface. A general form of such a relation may be written as

$$R_a = K_1 \left(\frac{h}{h_r} \right)^m \tag{6.2}$$

where h_r is a roughness parameter such as root mean square roughness, with respect to which the penetration depth can be normalised. K_1 and m are the constants, dependent on the geometric nature of the rough surface.

Thus,

$$\frac{H}{H_s} = 1 - \frac{K_2}{\left(\frac{h}{h_r}\right)^m} \tag{6.3}$$

Weiss [105] pointed out that the effect of roughness can be accounted for, by adding

an error term h_e in displacement. This would give, [19]

$$\begin{aligned} \frac{H_r}{H_0} &= \frac{Af(h \pm h_e)}{Af(h)} \\ &= (1 \pm \frac{h_e}{h}) \quad for\ spherical \\ &= (1 \pm \frac{h_e}{h})^2 \quad for\ conical/pyramidal \end{aligned}$$

where H_0 is the bulk hardness and Af is the area function of the indenter. Comparing this with equation 6.3 it is clear that for the assumed dependency of effective radius on penetration (equation 6.2), h_e is related to some roughness parameter and the indenter geometry. Accordingly we may write

$$h_e = k\ h_r \tag{6.4}$$

and

$$\frac{H_r}{H_0} = (1 - \frac{k}{h/h_r})^n \tag{6.5}$$

where k and n are parameters dependent on indenter geometry. n for Weiss's analysis is 1 for a spherical indenter and 2 for a conical indenter.

6.3 Numerical Simulation

The indentation of a rough surface is simulated using the method outlined in chapter 5. Two different reference planes, on which the permanent indent is projected to get the area for finding out the hardness are used. One is the mean plane of the rough surface and the other is a plane parallel to it but passing through the first contact point. The first one simulates the hardness obtained by the imaging techniques [11]. The second one simulates a depth sensing indentation with ideal depth resolution. The reference plane in an actual depth sensing experiment will lie in between these two extreme cases and is determined by the error involved in determining the contact point. The rms roughness of the surface was varied by changing the scaling constant,G (equation 5.1, 5.3). Simulations were carried out for 5 different rms values ranging from 0.62 nm to 2.16 nm. These rms values were obtained from the profile of the simulated surface with a sampling length of 1 μm. The indenter geometry is varied from ideally sharp cone to sphere, by varying the tip radius, R_i (figure 5.3) from 0 to 1500 nm.

To take into consideration the genuine property variation, simulations are also carried for a material with the assumed strength variation of

$$Y = Y_0\ (\ 1\ +\ \frac{c_0}{V^m}\ ) \tag{6.6}$$

With $m = 1/3$ this would give, for a conical indenter, a flat surface hardness variation of type,

$$H_v = H_0 \left(1 + \frac{c_1}{h} \right) \tag{6.7}$$

where H_0 is the bulk hardness and c_1 is a material constant.

6.4 Results and Discussion

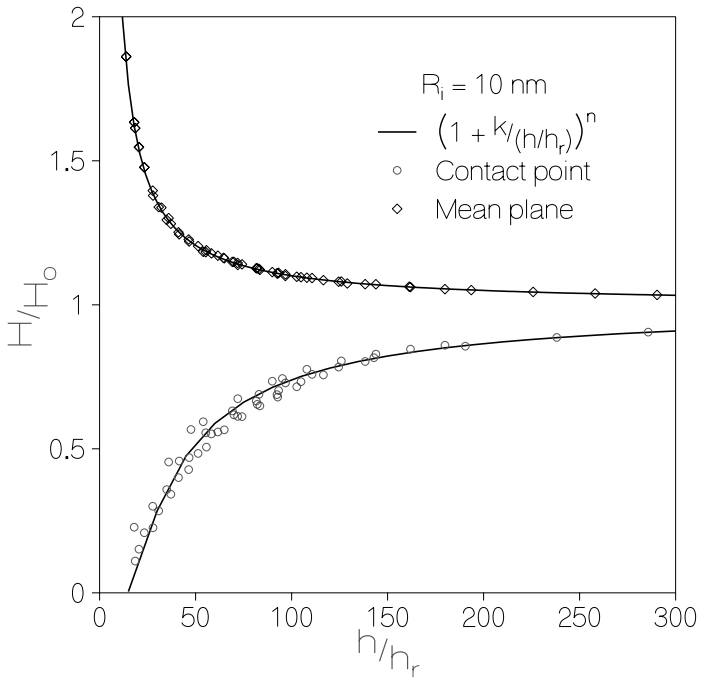

Figure 6.1: Mean hardness variation with normalised penetration

Figure 5.5 (chapter 5) shows the variation of hardness measured with the mean plane as reference, with penetration obtained from the numerical simulation for a conical indenter ($\phi = 60^o$) on a rough surface ($h_r = 1.446nm$). The solid line represents the variation in mean hardness. This mean hardness normalised with the bulk hardness (H_o) obtained for different values of the roughness is plotted in figure 6.1 against the penetration normalised with the rms value (h_r) of the simulated surface. The data is for a material with no property variation with depth/volume and for a indenter with the tip radius (R_i) of 10 nm. It can be seen that the hardness obtained from the mean plane is higher than that obtained from

the contact point. This figure further brings out clearly the fact that even for a material for which the bulk and the surface mechanical properties are the same, the hardness changes with penetration as long as the surface is rough. The data fits the equation 6.5 - plotted as the continuous lines, remarkably well.

Indenter tip radius R_i nm	$H_r/H_0 = (1 - \frac{k}{(h/h_r)})^n$ Ref: Contact point		Ref: Mean plane		Remarks
	k	n	k	n	
1500	25.15	1	-2.21	1	spherical
500	23.78	1	-2.28	1	almost spherical
10	14.07	2	-4.92	2	almost conical
0	13.29	2	-5.66	2	conical

Table 6.1: The indenter related parameters k and n obtained from numerical simulation

Table 6.1 gives the values of k and n obtained by fitting the equation 6.5 by least square method for different cases, on a material with no property variation. The regression coefficient is found to be better than 0.95. It is seen that n is an integer as predicted by Weiss [105] and the value of k is relatively insensitive to indenter radius, both the parameter being primarily dependent on the indenter shape. It may be noted here that k and n are not model (of the rough surface) specific and it is possible, given any measured real surface profile with proper resolution, to estimate the values of k and n by numerical simulation.

Thus the equation 6.5 can be used to determine the bulk hardness from the hardness measurements on the rough surface. This equation will be of great use in determining the hardness of thin films. The hardness of thin films can only be obtained, when the penetration depth is very small. When penetration is greater than one-tenth of the thickness of the film, the substrate starts influencing the measurement. The hardness measured gradually changes from the film value to the substrate value. The surface roughness of the film is approximately the same as the substrate, which is usually polished ($R_z \approx 0.1\ \mu m$). Thus in order to determine the hardness of the film whose thickness is 1 micron or less the penetration of the indenter will be of same order as roughness.

Equation 6.5 can be used only when the material property variation with depth/volume is negligible or non-existent. If the variation is considerable then as the strength of the asperities depends on their size and shape, there will be one further level of roughness dependence in the measured hardness. In figure 6.2, the normalised hardness for the materials, with and without strength variation, is plotted against penetration for a indenter tip radius (R_i) of

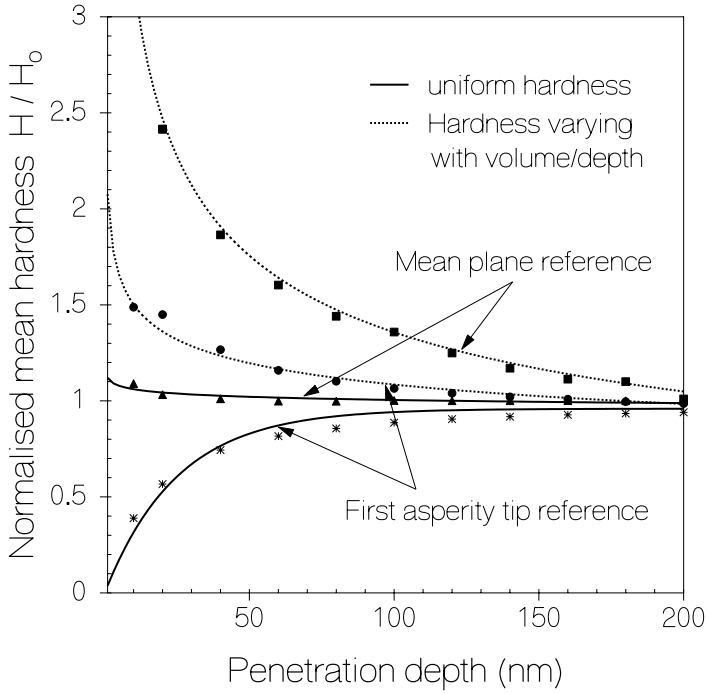

Figure 6.2: Mean hardness variation with penetration

10 nm on a rough surface of rms roughness of 1.45 nm. The figure delineates the influence of the method of measurement and the actual property gradient with depth on the measured hardness.

For a rough surface with a material property variation of type given by equation 6.6, the effect of roughness can be introduced, by adding an error term h_e in the depth used to calculate the volume. The equation 6.7 for a rough surface can be written as,

$$H_v = H_r \left(1 + \frac{c_1}{h - h_e} \right) \tag{6.8}$$

Substituting for h_e from equation 6.4, this can be written in a series form for $h > h_e$ as

$$H_v = H_r \left(1 + \frac{c_1}{h} + \frac{c_1\ k\ h_r}{h^2} + \frac{c_1\ (k\ h_r)^2}{h^3} + \ \ldots \right)$$

Neglecting higher order terms,

$$\frac{H_v}{H_r} = 1 + \frac{c_1}{h} + \frac{c_1\ k\ h_r}{h^2} \tag{6.9}$$

and by substituting for H_r from the equation 6.5,

$$H_v = \left(1 - \frac{k}{h/h_r}\right)^n \left(1 + \frac{c_1}{h} + \frac{c_1\, k\, h_r}{h^2}\right) H_0 \tag{6.10}$$

The first term in this equation gives the hardness variation due to roughness alone when there is no property variation with volume/depth. The second term expresses the effect of property gradient in its interaction with roughness on hardness. This term comes about because the deformation volume in an asperity, for a given penetration depth, changes with roughness. This results in a change in the aggregate strength of the asperity. The roughness thus alters the asperity-wise distribution of strength and geometric constraint. Hardness which is a product of strength and constraint summed over the whole contact domain, changes with roughness. When there is no property variation with volume, c_1 is zero and this expression reduces to equation 6.5. When the roughness on the other hand is zero ($h_r = 0$), then this expression (equation 6.10) reduces to the smooth surface material property profile (equation 6.7).

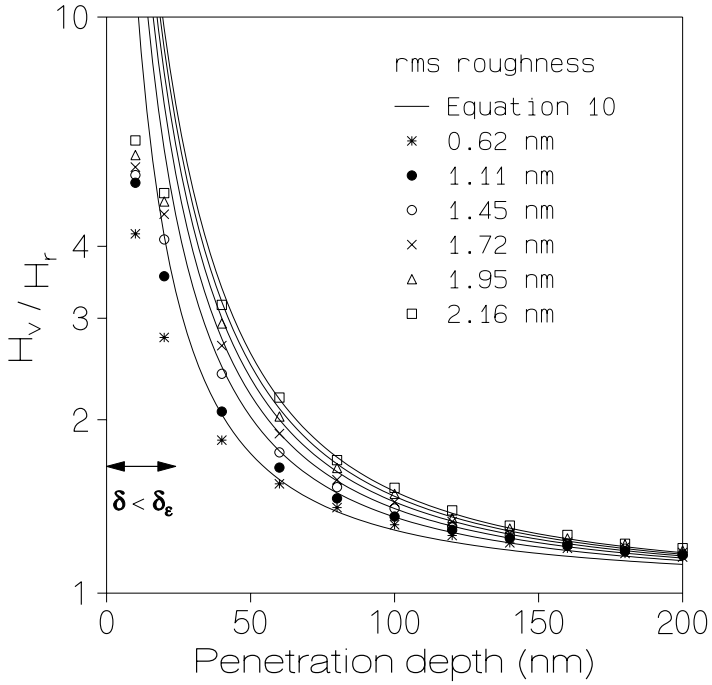

Figure 6.3: Mean hardness variation for different roughness

Figure 6.3 shows the variation of the mean hardness normalised with the rough surface

hardness (equation 6.5) as a function of the penetration depth and roughness, for a sharp conical indenter. The continuous lines in the figure are drawn as per the equation 6.9. It is seen that the variation of hardness due to the changing roughness and penetration depth is described well by this equation. Thus given the measured hardness, the indenter geometry related constants k_1 and n and the bulk hardness equation 6.10 can be used to determine the material constant c_1 which gives the gradient of property with depth.

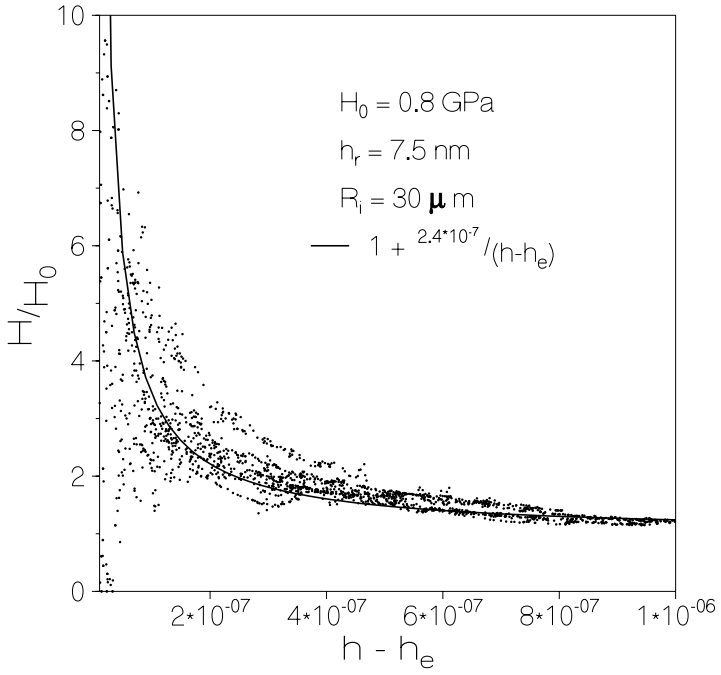

Figure 6.4: Experimental hardness variation corrected for surface roughness

This analysis can be used to obtain the genuine variation in hardness from the experimental data measured on the rough surface. The data in figure 3.24 has been corrected for the effect of surface roughness. The data was obtained by indenting work-hardened copper surface polished mechanically with a diamond paste of average diamond size of 2.5 μm. The rms value of such polished surface is 7.5 nm. This is obtained from a profile (figure 5.1) measured using an atomic force microscopy over a sampling length of 10 μm with a sampling interval of 25 nm. The conical diamond indenter has a tip radius R_i of about 30 μm (figure 3.22). The measured hardness H_m can be written for a general case as (from

equation 6.8)

$$H_m = H_r \, f(h - h_e) \tag{6.11}$$

where $f(h)$ is the unknown function giving the genuine variation of hardness with penetration. Since the tip radius of indenter (30 μm) is large compared to the maximum penetration ($\approx$ 2 μm), the flat surface hardness H_o can be obtained from spherical cavity model as (equation 5.4)

$$H_o = \begin{cases} \frac{2}{3} Y \left\{ 2 + \ln \left(\frac{\frac{E}{2\,Y} \frac{h}{2\,R_i} + 2\,(1-2\nu)}{3\,(1-\nu)} \right) \right\} & \text{if } H_0 < 3\,Y \\ 3\,Y & \text{otherwise} \end{cases}$$

Taking the values of k and n from table 6.1, H_r can be written for this indenter as (equation 6.5)

$$H_r = H_o \, (1 - \frac{25}{h/h_r})$$

Substituting the values of Youngs modulus ($E = 123\ GPa$) and poisson ratio ($v = 0.33$), the function $f(h)$ can be obtained.

In figure 6.4, the H_v/H_r is plotted against $h - h_e$ and gives the corrected hardness variation with penetration. The continuous line is the best fit of equation of type,

$$\frac{H}{H_o} = 1 + \frac{c_1}{h^m}$$

The index m is very close to 1, which gives the variation of type given by equation 6.7 assumed for the numerical simulation.

6.5 Conclusions

1. The roughness of a surface affects the hardness estimated by a nano-indentation, irrespective of whether the bulk and surface mechanical properties are the same.

2. The effective radius of the indented fractal surface increases in direct proportion to penetration and in inverse proportion to the rms roughness.

3. Known the indenter geometry and the surface roughness, a method has been developed to remove the effect of roughness on measured hardness using a simple algebraic equation. This will help to determine the genuine mechanical property profile of the surface region.

Chapter 7

Conclusions

The strength of the blister field that characterises the stresses in an elastic-plastic indentation is obtained *ab initio*, using energy conservation principles. It is found that this strength is proportional to $(load)^{1.5}$, and can be obtained as a function of the material properties and geometric configuration of the rigid indenter. The predicted strength values matches closely with the experimental values obtained from surface strain measurements. This method combined with surface strain measurement in nanoindentation is expected to help the understanding of the mesoscopic material behaviour.

A displacement controlled, depth sensing indenter capable of determining the mechanical properties of the materials by indenting them to the depths of few tens of nanometers has been designed, fabricated and tested. The main emphasis of the design is to account for the possible errors in the measurement by suitable post processing of data. The design uses flexure hinges to measure forces and to minimise the friction and hysterisis in mechanical movements.

The error and the scatter introduced in hardness measurements due to the roughness of the surface on which the indentation is carried out, is characterised. The standard deviation of the hardness measured on the rough surface, normalised with the mean hardness,

1. follows an inverse power law with the nominal contact area.
2. is independent of the material property gradient.
3. is more for depth sensing method of hardness determination than the imaging method.
4. can be quantified if the indenter geometry and the roughness at the length scales comparable to the penetration depths are known.

With decreasing penetration depths,the hardness measured on the rough surface of a material with no property gradient, decreases for the depth sensing indentations and increases for

imaging type of indentations. The error introduced in hardness measured on a rough surface, can be expressed in terms of indenter and surface geometries. The data obtained from depth sensing nanoindentations can be corrected for the effect of surface roughness.

References

[1] Agrait N. , Rodrigo J.G. , Rubio C. , Sirvent C. and Vieira S. , *Thin Solid Films*, **253**, 199, (1994).

[2] Alonso F. , Arizaga A. , Quainton S. , Ugarte J.J. , Vivente J.L. and J.I. , *Surf. Coat. Technol.*, **74**, (1995).

[3] Archard J.F. , *Proc. Roy. Soc. London A*, **243**, 190, (1957).

[4] Atkins A.G. and Tabor D. , *J. Mech. Phys. Solids*, **13**, 149, (1965).

[5] Bangert H. and Wangendristel A. , *J. Vac. Sci. Technol. A*, **4**(6), 2956, (1986).

[6] Baugert H. and Wagendristel , *Rev. Sci. Instrum.*, **56**, 1568, (1985).

[7] Bell T. , Bendel A. , Field J.S. , Swain M.V. and Thwaite E.G. , *Metrologia*, **28**, 463, (1991).

[8] Berry M.V. and Lewis Z.V. , *Proc. Roy. Soc. London A*, **370**, 459, (1980).

[9] Bhattacharya A.K. and Nix W.D. , *Int. J. Solids Structures*, **24**, 881, (1988).

[10] Bhattacharya A.K. and Nix W.D. , *Int. J. Solids Structures*, **24**, 1287, (1988).

[11] Bhusan B. , Koinkar V.N. and Ruan J.A. , *Proc. Inst. Mech. Engrs.*, **208**(1), 17, (1994).

[12] Billig V. , *Design*, **February**(4), 114, (1960).

[13] Binning G. , Quate C.F. and Gerber Ch. , *Phys. Rev. Lett.*, **56**, 930, (1986).

[14] Bobji M.S. and Biswas S.K. , *Phil. Mag. A*, **73**, 399, (1996).

[15] Bobji M.S. and Biswas S.K. , *Appl. Phys. Lett.*, **71**(8), 1059, (1997).

[16] Bobji M.S. and Biswas S.K. , Proc. of intl. conf. on recent advances in metallurgical processes, page 1224. New Age International Publishers, New Delhi, (1997).

[17] Bobji M.S. and Biswas S.K. , Surface modification technologies x, The Institute of Materials, London., (1997).

[18] Bobji M.S. and Biswas S.K. , *to appear in J. Mater. Res.*, (1998).

[19] Bobji M.S. , Fahim M. and Biswas S.K. , *Tribol. Lett.*, **2**, 381, (1996).

[20] Brinell J.A. , *zieme congress Internationale methodes dessai, Paris*, (1900).

[21] Brown S.R. and Scholz C.H. , *J. Geophysical Res. B*, **90**(7), 5531, (1985).

[22] Buckle H. , *Metall. Rev.*, **4**, 49, (1959).

[23] Burnham N.A. and Colton R.J. , *J. Vac. Sci. Technol. A*, **9**(4), 2548, (1991).

[24] Burnham N.A. , Colton R.J. and Pollock H.M. , *Nano Technology*, **4**, 1, (1993).

[25] Cebon D. and Ashby M.F. , *Measur. Sci. Technol.*, **5**, 296, (1994).

[26] Chakrabarthy J. , *Theory of Plasticity*, McGraw-Hill Book Co., Newyork., (1987).

[27] Chaudhri M.M. and Winter M. , *J. Phys. D: Appl. Phys*, **21**, 370, (1988).

[28] Chiang S.S. , Marshall D.B. and Evans A.G. , *J. Appl. Phys.*, **53**, 293, (1982).

[29] Cook R.F. and Pharr G.M. , *J. Am. Ceram. Soc.*, **73**, 787, (1990).

[30] Doerner M.F. and Nix W.D. , *J. Mater. Res.*, **1**(4), 601, (1986).

[31] Dumas G. and Baronet C.N. , *Int. J. Mech. Sci.*, **13**, 519, (1971).

[32] Feldman C. , Ordway F. and Bernstein J. , *J. Vac. Sci. Technol. A*, **8**(1), 117, (1990).

[33] Fleck N.A. , Muller G.M. , Ashby M.F. and Hutchinson J.W. , *Acta Metall*, **42**, 475, (1994).

[34] Follansbee P.S. and Sinclair G.B. , *Int. J. Solids Structures*, **20**, 81, (1984).

[35] Francis H.A. , *Wear*, **45**, 221, (1977).

[36] Gane N. , *Proc. Roy. Soc. London A*, **317**, 367, (1970).

[37] Ghosal A.K. and Biswas S.K. , *Phil. Mag. B*, **67**, 371, (1993).

[38] Giannakopoulous A.E. , Larsson Pl.L. and Vestergaard R. , *Int. J. Solids Structures*, **31**, 2679, (1994).

[39] Greenwood J.A. and Tripp J.H. , *Trans. ASME, J. Appl. Mech.*, **34**, 153, (1967).

[40] Greenwood J.A. and Williamson J.B.P. , *Proc. Roy. Soc. London A*, **295**, 300, (1966).

[41] Hardy C. , Baronet C.N. and Tordion G.V. , *Int. J. Numer. Meth. Engng.*, **3**, 451, (1971).

[42] Hill R. , *Mathematical Theory of Plasticity*, Oxford, Clarendon, (1950).

[43] Jarvis S. , *Atomic Force Microscopy and Tip-Surface Interactions*, PhD thesis, (1993).

[44] Jarvis S.P. , Weihs T.P. and Pethica J.B. , *Rev. Sci. Instrum.*, **64**(12), 3515, (1993).

[45] Johnson K.L , *J. Mech. Phys. Solids*, **18**, 115, (1970).

[46] Johnson K.L. , *Contact Mechanics*, Cambridge University Press, Cambridge., (1985).

[47] Johnson K.L. , Greenwood J.A. and Higginson J.G. , *Int. I. Mech. Sci*, **27**(6), 383, (1985).

[48] Knoop F. , Peters C.G. and Emerson W.B. , *Nat. Bureau of Standards*, **23**(1), 39, (1939).

[49] Kohlhoff S. , Gumbsch P. and Fischmeister H.F. , *Phil. Mag. A*, **64**, 851, (1991).

[50] Kumar P.K. Rajendra and Biswas S.K. , *Mechanics Research Communications*, **4**, (1996).

[51] Landman U. and Luedtke W.D. , *J. Vac. Sci. Technol. B*, **9**(2), 414, (1991).

[52] Lawn B.R. and Howes V.R. , *J. Mater. Sci.*, **16**, 2745, (1981).

[53] Lee C.H. , Masaki S. and Kobayashi S. , *Int. J. Mech. Sci.*, **14**, 417, (1972).

[54] Li Hui , Saigal S. and Wang P.T. , *Acta. Mater.*, **44**(7), 2591, (1996).

[55] Ling C.B. , *Trans. ASME, J. Appl. Mech.*, **74**, 141, (1952).

[56] Loubet J.L. , Georges J.M. and Meillie G. , Microindentation techniques in materials science and, In Blau P.J. and Lawn B.R. , editors, *ASTM STP 889*, page 72. ASTM, Philadelphia, (1986).

[57] Love A.E.H. , *The Mathematical Theory of Elasticity*, Cambridge University Press, (1920).

[58] Lu C.J. , Bogy D. and Kaneko R. , *Trans. ASME, J. Tribol.*, **116**, 175, (1994).

[59] Ludwik P. , *Die kgelprobe*, J. Springer, Berlin., (1908).

[60] Lyman T. , *Materials Hand Book*, ASM, Metals Park, Ohio, (1960).

[61] Majumdar A. and Bhushan B. , *Trans. ASME, J. Tribol.*, **112**, 205, (1990).

[62] Majumdar A. and Tien C.L. , *Wear*, **136**, 313, (1990).

[63] Mann J.B. and Farris T.N. , *Trans. ASME, J. Tribol.*, **116**, 430, (1994).

[64] Marsh D.M. , *Proc. Roy. Soc. London A*, **279**, 420, (1964).

[65] Mencik J. and Swain M.V. , *J. Mater. Res.*, **10**, 1491, (1995).

[66] Meyer E. , *Zeits. d. vereines Deutsh Ingenicure*, **52**, 645, (1908).

[67] Mindlin R.D. , *Physics*, **7**, 85, (1936).

[68] Miyahara K. , Matsuoka S. , Nagashima N. and Masuda H. , *J. Test. Eval.*, **22**(2), 121, (1994).

[69] Mott B.W. , *Microindentation Hardness Testing*, Butterworth, London., (1957).

[70] Mukhopadhyaya A. and Biswas S.K. , *Phil. Mag. Lett.*, **4**, 77, (1991).

[71] Murakami Y. , Tanaka K. , Itokazu M. and Shimamoto A. , *Phil. Mag. A*, **69**, 1131, (1994).

[72] Nayak P.R. , *Wear*, **26**, 165, (1973).

[73] Newey D. , Wilkins M.A. and Pollock H.M. , *J. Phys. E: Sci. Instrum.*, **15**, 119, (1982).

[74] Nishibori M. and Kinosita K. , *Thin Solid films*, **48**, 325, (1978).

[75] Nishimura K. , *Rec. Sci. Instrum.*, **62**(8), 2004, (1991).

[76] Oliver W.C. , Hutchings R. and Pethica J.B. , Microindentation techniques in materials science and, In Blau P.J. and Lawn B.R. , editors, *ASTM STP 889*, page 90. ASTM, Philadelphia, (1986).

[77] Oliver W.C. and Pharr G.M. , *J. Mater. Res.*, **7**, 1564, (1992).

[78] O'Neill H. , *Hardness Measurements of Metals and Alloys*, Chapman and Hall, London, (1967).

[79] Page T.F. and Hainsworth S.V. , *Surf. Coat. Technol.*, **61**, 201, (1993).

[80] Paros J.M. and Weisbord L. , *Machine Design*, **November**(25), 151, (1965).

[81] Pethica J.B. , Ion implantation into metals, page 147. Pergamon, (1982).

[82] Pethica J.B. , Hutchings R. and Oliver W.C. , *Phil. Mag. A*, **48**, 593, (1983).

[83] Pethica J.B. and Sutton A.P. , *J. Vac. Sci. Technol. A*, **6**(4), 2490, (1988).

[84] Pollock H.M. , Maugis D. and Barguins M. , Microindentation techniques in materials science and, In Blau P.J. and Lawn B.R. , editors, *ASTM STP 889*, page 47. ASTM, Philadelphia, (1986).

[85] Pullen J. and Williamson J.B.P. , *Proc. Roy. Soc. London A*, **327**, 159, (1972).

[86] Rangan C.S. , Sharma G.R. and Mani V.S.V. , *Instrumentation - Devices and Systems*, Tata McGraw Hill Publishing Co. Ltd., New Delhi, (1983).

[87] Sargent P.M. , Microindentation techniques in materials science and, In Blau P.J. and Lawn B.R. , editors, *ASTM STP 889*, page 160. ASTM, Philadelphia, (1986).

[88] Sayles R.S. and Thomas T.R. , *Nature*, **271**, 431, (1978).

[89] Scholl D. , Everson M.P. and Jaklevic R.C. , *Rev. Sci. Instrum.*, **65**(7), 2255, (1994).

[90] Sebastian K.S. , *Indentation Hardness of Polymers*, PhD thesis, (1994).

[91] Smith R. and Sandland G. , *Proc. Inst. Mech. Engrs.*, **1**, 623, (1922).

[92] Smith S.T. , Chetwynd D.G. and Bowen D.K. , *J. Phys. E: Sci. Instrum.*, **20**, 977, (1987).

[93] Sneddon I.N. , *Int. J. Engng. Sci.*, **3**, 47, (1965).

[94] Spoelder H.J.W. and Ullings F.H. , Graphics gems, page 121. Academic Press Inc., Boston, (1990).

[95] Stillwell N.A. and Tabor D. , *Proc. Phys. Soc.*, **78**, 169, (1961).

[96] Stone D. , Lafontaine W.R. , Alexopoulos P. , Wu T.W. and Li. C-Y , *J. Mater. Res*, **3**(1), 141, (1988).

[97] Tabor D. , *The Hardness of Metals*, Clarendon Press, Oxford, (1951).

[98] Tabor D. , Microindentation techniques in materials science and, In Blau P.J. and Lawn B.R. , editors, *ASTM STP 889*, page 129. ASTM, Philadelphia, (1986).

[99] Thomas T.R. , *Wear*, **79**, 73, (1982).

[100] Thomas T.R. , *Rough Surfaces*, Longman, London, (1982).

[101] Tsukamoto Y. , Yamaguchi H. and Yanagisawa M. , *Thin Solid Films*, **154**, 171, (1987).

[102] Ullner Ch. , *Phys. Status Solidi A*, **129**, 167, (1992).

[103] Wahlberg A. , *J. Iron Steel Inst.*, **59**, 243, (1901).

[104] Weiss H.J. , *Phys. Status Solidi A*, **99**, 491, (1987).

[105] Weiss H.J. , *Phys. Status Solidi A*, **129**, 167, (1992).

[106] Westergaard H.M. , *Trans. ASME, J. Appl. Mech.*, **6**, 49, (1939).

[107] whitehouse D.J. and Archard J.F. , *Proc. Roy. Soc. Lond. A*, **316**, 97, (1976).

[108] Wierenga P.E. and Franken A.J.J. , *J. Appl. Phys.*, **55**(12), 4244, (1984).

[109] Williams V.S. , Landesman A.L. , Shack R.V. , Vukobratovich D. and Bhushan B. , *Applied Optics*, **27**(3), 541, (1988).

[110] Woigard J. and Dargenton J.C. , *Measur. Sci. Technol.*, **6**, 16, (1995).

[111] Yoffe E.H. , *Phil. Mag. A*, **46**, 617, (1982).

[112] Yokouchi Y. , Chou T.W. and Greenfield I.G. , *Metall. Trans. A*, **14**, 2415, (1983).

[113] Yokouchi Y. , Chou T.W. and Greenfield I.G. , *J. Mater. Sci*, **22**, 3087, (1987).

[114] Yost F.G. , *Metall. Trans.*, **14**, 947, (1983).

[115] Zeng K. and Rowcliff D. , *Phil. Mag. A*, **74**, 1107, (1996).